

## ABSTRACT

Title of dissertation: A STATISTICAL CHARACTERIZATION OF THE  
ATMOSPHERES OF SUB-SATURN PLANET  
CANDIDATES IN THE *KEPLER* ARCHIVE

Holly Ann Sheets, Doctor of Philosophy, 2016

Dissertation directed by: Professor L. Drake Deming  
Department of Astronomy

Exoplanet atmospheric characterization is still in its early stages. Large surveys like the *Kepler* Mission provide thousands of planet candidates, but follow-up observations to characterize the individual candidates are often difficult to obtain. In this thesis, I develop a method to detect small atmospheric signals in *Kepler*'s planet candidate light curves by averaging light curves for multiple candidates with similar orbital and physical characteristics. I also consider two applications of this method: at secondary eclipse, to determine the average albedo of groups of planet candidates, and near transit, to determine whether on average the planets have cloud-free, low-mean-molecular-weight atmospheres, or cloudy/hazy/high-mean-molecular-weight atmospheres. This approach allows the measurement of properties that are unmeasurable for candidates individually, because of their low signal-to-noise, and it prevents biasing of the results by false positives (candidates that are not actually planets) and outliers by not depending on only a few measurable candidates.

I first develop the method and apply it to the secondary eclipses of 32 close-in *Kepler* planet candidates between 1 and 6  $R_{\oplus}$  with short cadence data available, in

order to determine their average albedo. I then adapt the method to the long cadence data, accounting for the effects of the longer integration time. The increase in the number of candidates available in long cadence allows for finer radius groupings of 1 to 2  $R_{\oplus}$ , 2 to 4  $R_{\oplus}$ , and 4 to 6  $R_{\oplus}$ . The short cadence average includes 6,238 individual eclipses, while the long cadence averages contain 80,492 eclipses from 56 candidates in the 1 to 2  $R_{\oplus}$  bin, 22,677 eclipses from 38 candidates in the 2 to 4  $R_{\oplus}$  bin, and 4,572 eclipses from 16 candidates in the 4 to 6  $R_{\oplus}$  bin. In both studies, I find that these planet candidates are generally dark, though there are bright outliers like Kepler-10b, and I discuss the implications of these results for understanding the atmospheres of these planets. Finally, I apply the method to *Kepler* planet candidates in short cadence near transit, looking for a brief brightening due to light that is refracted through the atmospheres of the planets and directed toward the observer just before and just after transit. Refracted light is strongest in planetary atmospheres that are cloud-free and have a low mean molecular weight. Preliminary results suggest this strong refraction effect is not present in the selected group of 10 candidates with radii between 0.8 and 3  $R_{\oplus}$ , but I begin to develop a more detailed model and sketch out future plans to improve the model and to continue testing for the presence of refracted light with greater sensitivity.

A STATISTICAL CHARACTERIZATION OF THE  
ATMOSPHERES OF SUB-SATURN PLANET CANDIDATES  
IN THE *KEPLER* ARCHIVE

by

Holly Ann Sheets

Dissertation submitted to the Faculty of the Graduate School of the  
University of Maryland, College Park in partial fulfillment  
of the requirements for the degree of  
Doctor of Philosophy  
2016

Advisory Committee:

Professor L. Drake Deming, Chair/Advisor

Professor Suvi Gezari

Professor Douglas P. Hamilton

Dr. Shawn Domagal-Goldman

Professor Rachel Pinker, Graduate Dean's Representative

© Copyright by  
Holly Ann Sheets  
2016

## Preface

I am grateful for support in this work from NASA’s Virtual Planetary Laboratory (Victoria Meadows of the University of Washington, P. I.) and from NASA’s Astrophysics Data Analysis Program (ADAP) under grant NNX15AE53G, entitled “A Statistical Characterization of the Atmospheres of Kepler’s Small Planets” (L. Drake Deming of the University of Maryland, P.I.).

This thesis contains work published in the *Astrophysical Journal* as well as work currently in preparation for submission to the same journal. Chapter 2 was published under the title “Statistical Eclipses of Close-in Kepler Sub-Saturns” (Sheets & Deming, 2014). Chapter 3 will soon be submitted. Results from Chapter 2 were presented at the Kepler Science Conference II in November 2013, the 223rd Meeting of the American Astronomical Society in January 2014, and the 46th Annual Meeting of the Division for Planetary Sciences in November 2014. Preliminary results from Chapter 3 were presented at the 225th Meeting of the American Astronomical Society in January 2015. Results from Chapter 3 were presented at the Statistics and Exoplanets Focus Meeting at the XXIX General Assembly of the International Astronomical Union in August 2015, the 47th Annual Meeting of the Division for Planetary Sciences in November 2015, and the 227th Meeting of the American Astronomical Society in January 2016.

This thesis includes data collected by the Kepler mission. Funding for the Kepler mission is provided by the NASA Science Mission directorate. All of the data from Kepler presented in this thesis were obtained from the Mikulski Archive

for Space Telescopes (MAST). STScI is operated by the Association of Universities for Research in Astronomy, Inc., under NASA contract NAS5-26555. Support for MAST for non-HST data is provided by the NASA Office of Space Science via grant NNX13AC07G and by other grants and contracts. This research has made use of the NASA Exoplanet Archive, which is operated by the California Institute of Technology, under contract with the National Aeronautics and Space Administration under the Exoplanet Exploration Program.

## Acknowledgments

Thank you to the students, faculty, and staff in the Department of Astronomy whom I have gotten to know during my journey here and who have made that journey easier.

Thanks especially to my advisor, Professor Drake Deming, for his guidance, encouragement, and patience when the words wouldn't write themselves. Thanks also to Professor Stuart Vogel, for his efforts as department chair to promote diversity and inclusion in the department, and for all that he has done on behalf of the graduate students in the department. Thanks to my committee members for their time and valuable input on my work. Thanks to Professor Doug Hamilton for being a sounding board when I needed it.

Thanks to Professor Derek Richardson, Dr. Melissa Hayes-Gehrke, Alice Olmstead, and the rest of the A120/121 overhaul team for including me in the process. I've learned so much about teaching and education research from this experience, which will hopefully come in handy in the near future. Thanks also to Observatory Director Elizabeth Warner for indulging my love of looking through telescopes.

Thanks to my family and friends for their support throughout the years.

Lastly, thanks to my dog, Mira, who is my greatest friend and confidant.

# Table of Contents

List of Tables	vii
List of Figures	viii
List of Abbreviations	x
1 Introduction	1
1.1 Outline of Thesis	22
2 Statistical Eclipses of Short Cadence Close-in <i>Kepler</i> Sub-Saturns	24
2.1 Introduction	24
2.2 <i>Kepler</i> Observations	26
2.3 Averaging Candidate Light Curves	30
2.4 Reflected and Thermal Light Modeling	32
2.5 Results and Discussion	33
2.5.1 Close-in Candidates	33
2.5.2 Control Group	37
2.5.3 Individual Candidates	48
2.5.4 Advantages and Limitations of the Technique	54
2.6 Implications for Atmospheres and Surfaces of Sub-Saturns	57
2.6.1 Presence of Atmospheres in My Sample	57
2.6.2 Expected Albedos	59
2.7 Chapter 2 Summary	61
3 Statistical Eclipses of Long Cadence Close-in <i>Kepler</i> Sub-Saturns	63
3.1 Introduction	63
3.2 <i>Kepler</i> Data and Candidate Selection	64
3.3 Averaging the Long Cadence Data	72
3.3.1 Scaling and Stacking the Individual Eclipses	72
3.3.2 Notes on Individual Candidates	78
3.3.2.1 KOI 1662.01	78
3.3.2.2 KOIs 2396.01 and 2882.02	80
3.3.2.3 KOI 2795.01	80

3.3.2.4	KOI 4294.01	81
3.3.2.5	KOI 4351.01	83
3.3.2.6	KOI 4924.01	84
3.4	Modeling Reflected Light and Thermal Emission	84
3.5	False Positive and Other Detrimental Scenarios	85
3.5.1	Dilution by Unknown Objects in Aperture	85
3.5.2	Eccentric Eclipsing Binaries	87
3.5.3	Half-Period Eclipsing Binaries	88
3.5.4	Eccentric Planets	88
3.6	Results and Discussion	91
3.6.1	Super-Earths	91
3.6.1.1	Excluding Kepler-10b	91
3.6.1.2	Including Kepler-10b	92
3.6.2	Mini-Neptunes	95
3.6.3	Super-Neptunes	95
3.6.4	Comparison to Short Cadence	100
3.6.5	Comparison to Demory (2014)	109
3.6.6	Biases in the Albedo Due to Averaging	110
3.6.7	Implications of the Low Albedos	111
3.7	Chapter 3 Summary	113
4	Refraction and Future Work	115
4.1	Background	115
4.2	Averaging the Data	121
4.3	Modeling Refraction	125
4.4	Future Work	129
5	Summary of the Thesis	133
	Bibliography	137

## List of Tables

1	List of Abbreviations . . . . .	x
1.1	Radii of General Planet Groups and Solar System Planets . . . . .	8
1.2	Individual Detections of Secondary Eclipses in <i>Kepler</i> Data . . . . .	20
2.1	Candidate Parameters . . . . .	28
2.2	Eclipse depths and albedos . . . . .	37
2.3	Control Group Candidate Parameters . . . . .	40
2.3	Control Group Candidate Parameters . . . . .	41
2.3	Control Group Candidate Parameters . . . . .	42
2.3	Control Group Candidate Parameters . . . . .	43
2.3	Control Group Candidate Parameters . . . . .	44
2.3	Control Group Candidate Parameters . . . . .	45
2.3	Control Group Candidate Parameters . . . . .	46
2.3	Control Group Candidate Parameters . . . . .	47
2.3	Control Group Candidate Parameters . . . . .	49
2.4	Kepler-10b Studies . . . . .	52
3.1	Candidate Parameters . . . . .	67
3.1	Candidate Parameters . . . . .	68
3.2	Candidate Parameters . . . . .	69
3.2	Candidate Parameters . . . . .	70
3.3	Albedo Results . . . . .	114

## List of Figures

1.1	Information from a transit light curve . . . . .	3
1.2	Anatomy of a transit curve . . . . .	6
1.3	KOI 13.01 light curve . . . . .	7
1.4	Thermal Phase Curve of HD 189733b . . . . .	13
1.5	Radius vs. Mass . . . . .	15
1.6	Kepler-10b light curve . . . . .	19
2.1	Rescaling Phase for Stacking . . . . .	30
2.2	Average Light Curve, Excluding Kepler-10b . . . . .	34
2.3	Average Light Curve for Control Group . . . . .	38
2.4	Average Light Curve for Kepler-10b . . . . .	50
2.5	Average Light Curve for KOI 102.01 . . . . .	51
2.6	Average Light Curve for KOI 116.03 . . . . .	53
2.7	Calculated Equilibrium Temperatures Versus Radius . . . . .	58
3.1	Host Star Spectral Types . . . . .	71
3.2	Noise Test Histogram 1 . . . . .	74
3.3	Noise Test Histogram 2 . . . . .	75
3.4	Projection Test Failure . . . . .	76
3.5	KOI 1662.01 Light Curve . . . . .	79
3.6	KOI 2795.01 Weak Light Curve . . . . .	81
3.7	KOI 2795.01 Strong Light Curve . . . . .	82
3.8	KOI 4351.01 Light Curve . . . . .	83
3.9	Eccentric Planets Test . . . . .	90
3.10	Super-Earths: 55 candidates . . . . .	93
3.11	Super-Earths: Shortened Group . . . . .	94
3.12	Super-Earths: 55 Candidates and Kepler-10b . . . . .	96
3.13	Super-Earths: Shortened Group and Kepler-10b . . . . .	97
3.14	Mini-Neptunes: 38 Candidates . . . . .	98
3.15	Mini-Neptunes: Shortened Group . . . . .	99
3.16	Super-Neptunes: 16 Candidates . . . . .	101
3.17	Super-Neptunes: Shortened Group . . . . .	102

3.18	Sub-Saturns: 109 Candidates	103
3.19	Sub-Saturns: Shortened Group	104
3.20	Sub-Saturns: 109 Candidates and Kepler-10b	105
3.21	Sub-Saturns: Shortened Group and Kepler-10b	106
3.22	Albedo Vs. Radius	108
4.1	Sidis and Sari Refraction Light Curve	117
4.2	Spatially Resolved Refraction Model	120
4.3	Transforming Candidates for Stacking	123
4.4	Light Curve Near Transit for 300K to 400K Small Planets	124
4.5	Figure Adapted from Baum & Code (1953)	127
4.6	Ray-Tracing in 1D Model	128
4.7	Light Curve from 1D Model for Venus	130

Table 1. List of Abbreviations

Constants and Variables	
$A_B$	Bond Albedo
$A_g$	Geometric Albedo
AU	Astronomical Unit ( $1.496 \times 10^8$ km)
$\mu$	Mean Molecular Weight
$R_{\oplus}$	Earth's radius (6371 km)
$R_p$	Planet radius
$R_*$	Stellar Radius
$R_{\odot}$	Solar Radius (695,500 km)
Abbreviations	
KOI	Kepler Object of Interest
MCMC	Markov Chain Monte Carlo
PDC	Presearch Data Conditioning
ppb	parts per billion
ppm	parts per million

## Chapter 1: Introduction

The exoplanetary science community seeks to understand how common habitable, Earth-like planets around Sun-like stars are, as well as the physical properties of those planets. The first confirmed planets discovered outside our solar system were far from habitable. These planets were only a few times the mass of the Earth, but they were detected as their orbits perturbed the precise timing of the radio pulses from their host star, a neutron star ([Wolszczan & Frail, 1992](#); [Wolszczan, 1994](#)). Shortly thereafter, the first exoplanet around a Sun-like star, 51 Pegasi, was found using the radial velocity method ([Mayor & Queloz, 1995](#)). The radial velocity method looks for the “wobble” of the star as the star and planet orbit their common center of mass. This wobble produces a periodic Doppler shift in the spectral lines of the star. The exoplanet, named 51 Peg b, is a gas giant, at least as massive as Jupiter, but orbits its star in only 4.23 days. Jupiter, in contrast, takes nearly 12 years to orbit the Sun. The radial velocity method works best for massive, close-in planets; These create the largest Doppler shifts, with amplitudes on the order of 100 m/s and periods on the order of days ([Lovis & Fischer, 2010](#)). Earth, on the other hand, produces a shift with an amplitude of only 10 cm/s over a period of a year. The radial velocity method was used to detect 159 exoplanets in its first 10

years<sup>1</sup>, but using it as a discovery method was slow going. The high-precision spectra required for the radial velocity measurements means that many targets cannot be monitored at once, and not all of the targets will even have detectable planets.

Radial velocity measurements cannot constrain the orientation of the orbit to our line of sight (i.e. the inclination), and so they can only place a lower limit on the mass of the exoplanet. If an exoplanet transits its host star, passing between the star and our line of sight, not only is the inclination then determined, but the radius of the planet can also be determined (cf. Fig. 1.1). The first exoplanet transit (Charbonneau et al., 2000) was measured as a follow-up on a planet initially discovered by the radial velocity method around the star HD 209458. This detection demonstrated that photometric techniques and technologies were sufficiently developed to make searching for exoplanets via transit viable, as well as enabling the first bulk density measurement of an exoplanet.

The *Kepler* mission was designed to use the transit method to determine the fraction of stars in the solar neighborhood that harbor habitable exoplanets (Borucki et al., 2009), often called  $\eta_{\oplus}$  when considering only Sun-like stars. *Kepler* used precision photometry to look for the transit signal, by staring for 4 years at a single field located just above the Galactic plane. It provided near-continuous coverage at a 30-minute cadence for about 150,000 target stars, as well as for a subset of 512 targets at a 60-second cadence. After only four months of observations, the mission found 1235 planet candidates (Borucki et al., 2011). The primary mission

---

<sup>1</sup>From the confirmed planet table at the NASA Exoplanet Archive at [http://exoplanetarchive.ipac.caltech.edu/docs/counts\\_detail.html](http://exoplanetarchive.ipac.caltech.edu/docs/counts_detail.html)

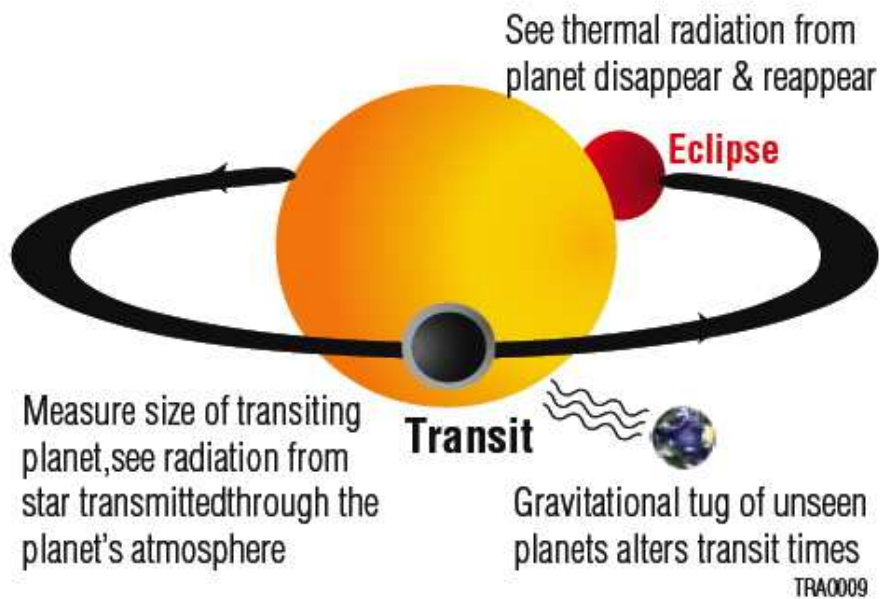


Figure 1.1 This figure, adapted from the EPOXI mission concept study report, shows several pieces of information that can be derived from a transiting planet. As the planet transits its star, the opaque part of the planet blocks out light from the star completely. Light also passes through the atmosphere of the planet, and so the planet looks larger at wavelengths where strong absorption features occur in its atmosphere, and smaller where the light freely passes deeper into the atmosphere. As the planet passes behind the star during secondary eclipse, reflected light and thermal emission from the planet is blocked. Lastly, delays in the timing of subsequent transits can be used to determine the mass of the planet and other, potentially unseen, planets in the system. These delays are caused by gravitational interactions between the planets in the system.

ended after hardware failures made it impossible to continue pointing at the chosen field. Analysis of the 4 years of data has yielded a total of 4696 planet candidates, of which 2329 have been confirmed (Coughlin et al., 2016). The *Kepler* candidate catalog lists any object with transits consistent with a planetary interpretation as “planet candidates”, and it lists any object that fails one or more consistency checks for the planetary interpretation as a “false positive” (Borucki et al., 2011). Planet candidates are changed to “confirmed” planets via one of two paths. The first path is measurements of the planet mass by radial velocity or transit timing variations (cf. Fig. 1.1). The second path is by intensive review of the *Kepler* data to rule out non-planetary interpretations. If the planetary interpretation is at least 100 times more likely than non-planetary interpretations, the planet candidate graduates to “confirmed” or “validated” status.

Transit observations provide several key pieces of information about an exoplanet and its orbit, provided the host star’s parameters are well-known. Most directly, the time between transits gives the period of the orbit. Combining the orbital period with the mass of the star determines the semi-major axis of the planet’s orbit. The relative drop in light during transit compared to the total light from the system outside of transit is simply the ratio of the areas of the planet and the star:  $(R_p/R_*)^2$ , where  $R_p$  is the planet radius and  $R_*$  is the stellar radius. This relative drop is known as the transit depth, which is labeled as  $d$  in Fig. 1.2. If the photometry is sufficiently precise and well-sampled in time, the planet radius and the stellar radius can be measured directly from the shape of the transit light curve (e.g. Brown et al., 2001), but the *Kepler* mission largely relies on host star

parameters derived from other means.

With the planet radius known from the transit, exoplanets are commonly broken down into five broad groups: Earth-size ( $< 1.25 R_{\oplus}$ ), super-Earth-size (1.25-2  $R_{\oplus}$ ), Neptune-size (2-6  $R_{\oplus}$ ), Jupiter-size (6-15  $R_{\oplus}$ ), and larger than Jupiter (15-25  $R_{\oplus}$ ) (Borucki et al., 2011). For the purposes of this work, super-Earths include planets down to 1  $R_{\oplus}$ , and Neptune-size planets are broken down further into mini-Neptunes (2-4  $R_{\oplus}$ ) and super-Neptunes (4-6  $R_{\oplus}$ ). Table 1.1 summarizes the groups and also includes the eight planets in our solar system for reference.

A byproduct of the precision photometry obtained by *Kepler* in a few cases is the measurement of the secondary eclipse of the planet. The secondary eclipse occurs when the planet passes behind its star, at which time reflected light and thermal emission from the planet are blocked. For planets in circular orbits, this occurs at phase 0.5. The phase of an observation is calculated by taking the time elapsed since some reference time, dividing by the period of the orbit, and subtracting the integer number of cycles that have passed. This results in phase values from 0 to 1. The *Kepler* telescope has a broad bandpass in the optical, from 420 to 900 nm<sup>2</sup>, and so secondary eclipses in *Kepler* light curves are mostly due to reflected stellar light. An example of a *Kepler* light curve showing a transit and a secondary eclipse is shown in Fig. 1.3, for Kepler Object of Interest (KOI) 13.01, which has a radius of 1.61 times the radius of Jupiter. Since the signal is primarily reflected stellar light, it can be several orders of magnitude fainter than the transit signal. The drop in light during eclipse relative to the total light of the system just outside of eclipse

---

<sup>2</sup><http://keplerscience.arc.nasa.gov/the-kepler-space-telescope.html>

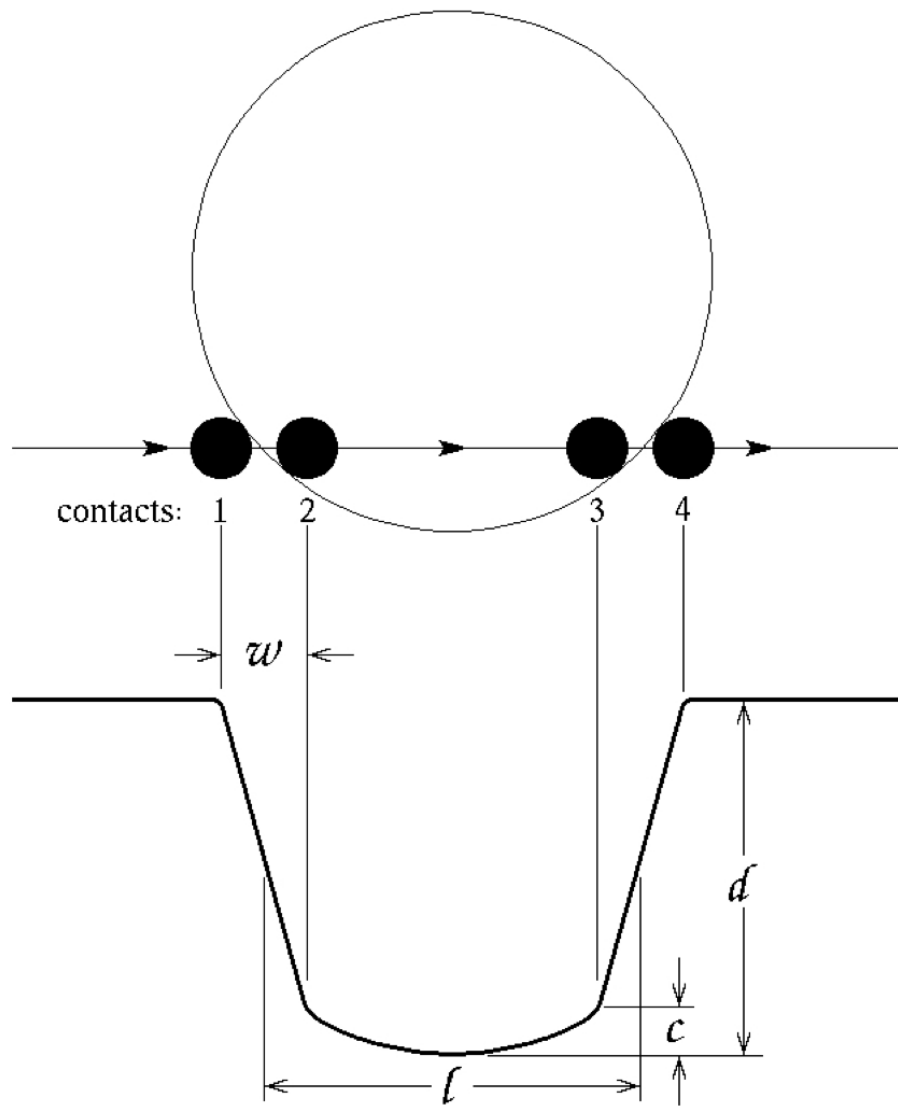


Figure 1.2 Adapted from [Brown et al. \(2001\)](#). Anatomy of a transit curve. The planet moves in its orbit from left to right across the face of the star. At first contact, the edge of the planet appears to first touch the limb of the star. Second contact is when the whole planet first covers the star. Third contact is the last moment when the entire planet covers the star, and fourth, or last, is the final moment at which the edge of the planet appears to touch the limb of the star. Ingress is defined as the period between first and second contact ( $w$ ), while egress is the period between third and fourth contact. The curvature due to stellar limb darkening is labeled  $c$ , while the depth of the eclipse is labeled  $d$ . The duration of the transit is labeled  $l$ .

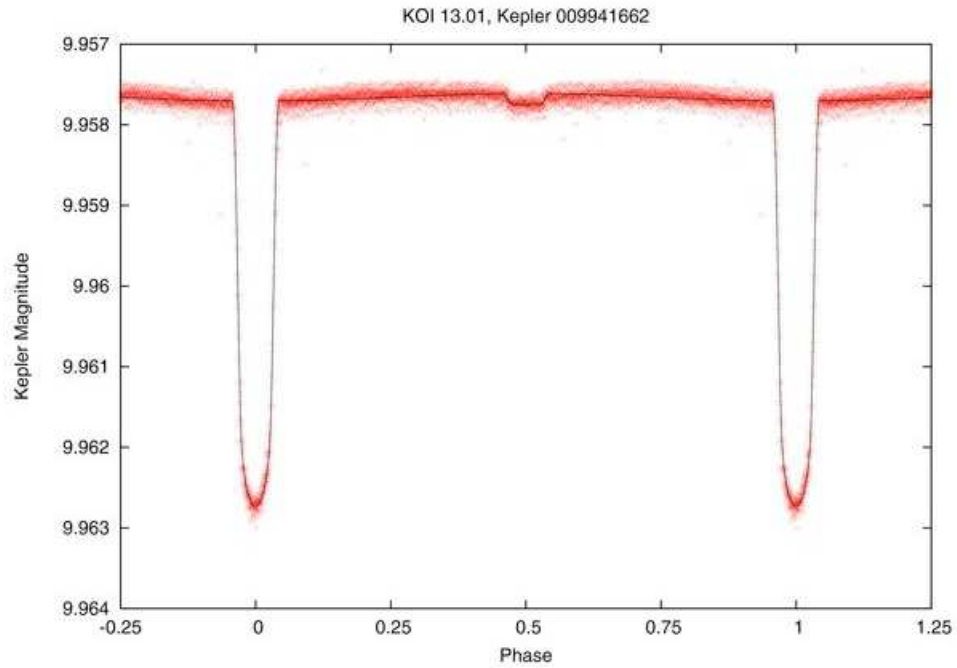


Figure 1.3 Adapted from [Coughlin & López-Morales \(2012\)](#). This figure shows the *Kepler* light curve for KOI 13.01, a hot Jupiter. Note the transit at phase 0, repeated at phase 1, and the secondary eclipse at phase 0.5. The red points are data while the black curve is a fit to the data. Also note the curvature in the transit due to stellar limb darkening, which is not present in the secondary eclipse.

Table 1.1. Radii of General Planet Groups and Solar System Planets

Planet/Group	Radius <sup>a</sup> ( $R_{\oplus}$ )
Mercury	0.383
Mars	0.532
Venus	0.949
Earth	1.000
Earth-size	< 1.25
super-Earth-size <sup>b</sup>	1.25-2
mini-Neptune	2-4
Neptune	3.88
Neptune-size	2-6
Uranus	4.01
super-Neptune	4-6
Jupiter-size	6-15
Saturn	9.45
Jupiter	11.21
Larger than Jupiter	15-25

<sup>a</sup>Radius bins for exoplanets from [Borucki et al. \(2011\)](#), except mini-Neptunes and super-Neptunes. Radii for Solar System planets from NASA's Planetary Fact Sheet - Ratio to Earth Values at [http://nssdc.gsfc.nasa.gov/planetary/factsheet/planet\\_table\\_ratio.html](http://nssdc.gsfc.nasa.gov/planetary/factsheet/planet_table_ratio.html), curated by Dr. David R. Williams.

<sup>b</sup>In this work, super-Earths include down to 1  $R_{\oplus}$ .

(i.e. the eclipse depth) is given by:

$$\frac{F_p}{F_*} = A_g \left( \frac{R_p}{a} \right)^2 \quad (1.1)$$

where  $F_p$  is the flux of reflected light from the planet,  $F_*$  is the flux from the star,  $A_g$  is the geometric albedo,  $R_p$  is the planet radius, and  $a$  is the orbital distance of the planet. Maximum values of  $(R_p/a)^2$  for the shortest-period (and therefore smallest semi-major axis) *Kepler* sub-Saturn planet candidates are less than 100 parts per million (ppm). For Earth, with a radius of 6371 km and a semi-major axis of  $1.496 \times 10^8$  km,  $(R_p/a)^2 = 0.0018$  ppm = 1.8 parts per billion (ppb). The geometric albedo, typically ranging from 0 to near 1, is the ratio of the light reflected by a body directly back toward the light source to the light reflected by a Lambertian surface (a disk that is a diffuse, perfect reflector). The highest measured geometric albedo in the solar system is Enceladus at 1.38 (Verbiscer et al., 2007), and values this high are typical of cold, young surfaces found among the geologically active icy satellites of giant planets in the solar system. Earth’s geometric albedo is 0.367 (Traub & Oppenheimer, 2010), so a distant observer would see secondary eclipses of Earth that were only 66 ppb. The gas giants in our solar system have geometric albedos of  $\sim 0.5$ , with Neptune slightly lower at 0.4 (Traub & Oppenheimer, 2010). Early modeling of giant planets outside the solar system suggested that hot giant planets would be dark, while cooler planets, below 400 K, would have clouds of water or other condensates that would make them bright (Marley et al., 1999). The first observational constraints on the geometric albedos of extrasolar giant planets came from work on  $\tau$  Boötis. Collier Cameron et al. (1999) found, using a method

other than secondary eclipses, a tentative reflected light signal of 190 ppm from the hot Jupiter around  $\tau$  Boo, but [Charbonneau et al. \(1999\)](#), using the same method, set an upper limit on the signal of 50 ppm, resulting in a geometric albedo less than 0.3. Transit depths, in contrast, are typically on the order of 100 ppm or greater. Earth seen from outside our solar system would have a transit depth of 84 ppm. *Kepler* was designed to look for transits, and so secondary eclipses are measurable only around the brightest stars in the sample, for which the photometric noise is smallest.

The hottest exoplanets may have a thermal contribution to the secondary eclipse depth, due to re-radiation of absorbed light from the host star. The Spitzer Space Telescope, an infrared mission, has detected thermal emission at secondary eclipse for many exoplanets (e.g. [Charbonneau et al., 2005, 2008](#); [Christiansen et al., 2010](#); [Deming et al., 2005, 2007](#); [Fressin et al., 2010](#); [Grillmair et al., 2007](#); [Machalek et al., 2008](#); [Todorov et al., 2010](#)). The planet-to-star contrast in the infrared is more favorable than in the optical bandpass of *Kepler* because of the emission from the planet. Thermal emission has even been detected by Spitzer from super-Earths, such as 55 Cancri e ([Demory et al., 2012](#)). The thermal contribution is given by the ratio of the area of the planet to the area of the star times the ratio of the integral of the blackbody flux from the planet to that of the stellar flux, modified by the response function of the detector. The blackbody flux for the planet is calculated assuming the equilibrium temperature for the planet, given by:

$$T_p = T_* \left( \frac{R_*}{a} \right)^{1/2} [f(1 - A_B)]^{1/4} \quad (1.2)$$

where  $T_p$  is the planet’s temperature,  $T_*$  is the star’s effective temperature,  $a$  is the planet’s orbital distance,  $R_*$  is the stellar radius, and  $A_B$  is the Bond albedo. The redistribution factor  $f$  typically varies between a value of 1/4 for complete redistribution of heat around the planet to 2/3 for instantaneous re-radiation of heat (see, e.g. [Esteves et al., 2013](#); [Hansen, 2008](#); [López-Morales & Seager, 2007](#); [Rowe et al., 2006](#)). The Bond albedo is the total light reflected by a body divided by the total light incident on the body, integrated over all wavelengths (as in, e.g. [Sudarsky et al., 2000](#)). For a Lambertian surface, the Bond albedo is related to the geometric albedo by  $A_B = (3/2)A_g$  (as in, e.g. [Esteves et al., 2013](#); [López-Morales & Seager, 2007](#); [Rowe et al., 2006](#)).

In addition to secondary eclipses, reflected light and thermal emission can create a subtle variation in the light curve over the course of the planet’s orbit, called a phase curve. The phase variation arises due to the changing fraction of the dayside of the planet visible to the observer as the planet orbits its host star. [Knutson et al. \(2007\)](#) studied the thermal emission phase curve of HD 189733b with Spitzer at  $8\mu\text{m}$ , shown in Figure 1.4. The authors find that the dayside of the tidally-locked planet is brighter than the nightside, and the peak brightness occurs just before secondary eclipse, suggesting a hot spot that has shifted slightly east of the substellar point. [Zellem et al. \(2014\)](#) studied HD 209458b with Spitzer at  $4.5\mu\text{m}$ , finding a similar eastward shift of the hot spot, which is predicted by circulation models due to superrotational winds at the equator. The phase curve for super-Earth 55 Cancri e has also been measured, and it suggests that the planet either has an optically thick atmosphere with heat redistribution across only the dayside, or a molten surface

capable of redistributing heat in a similar fashion (Demory et al., 2016).

In the seven years since its launch, the *Kepler* mission has delivered on its original mission. Early estimates of  $\eta_{\oplus}$  based on the 2011 February release of data suggested that 1-3% of Sun-like stars hosted planets that were similar in radius and insolation to Earth (Catanzarite & Shao, 2011). By 2013, estimates based on added data suggested 15% of cool stars, less than 4000 K, hosted Earth-sized planets in the habitable zone (Dressing & Charbonneau, 2013), and 11% (Petigura et al., 2013) of Sun-like stars hosted Earth-like planets. Questions of completeness of the candidate catalog posed a challenge to calculating these estimates. A more recent analysis by Burke et al. (2015) includes the Q1-Q16 catalog from Mullally et al. (2015) and a completeness study of the pipeline by Christiansen et al. (2015), and finds a lower limit for  $\eta_{\oplus}$  of 10% for Sun-like stars. Individual planets of interest include Kepler-62e, Kepler-62f, Kepler-438b, Kepler-442b, and Kepler-452b. Kepler-62e and Kepler-62f are two of five planets detected in their system (Borucki et al., 2013). They are  $1.61 R_{\oplus}$  and  $1.41 R_{\oplus}$ , respectively, and orbit in the habitable zone of their K dwarf host. The most Earth-like planets found to date are Kepler-438b and Kepler-442b (Torres et al., 2015). Kepler-438b has a radius of just  $1.12^{+0.16}_{-0.17} R_{\oplus}$  and receives 140% of the effective insolation of the Earth, though the host star is less massive than the Sun. Meanwhile, Kepler-442b is larger at  $1.34^{+0.11}_{-0.18} R_{\oplus}$  but receives only 66% of the effective insolation of the Earth. Kepler-442b also orbits a host star that is less massive than the Sun. Kepler-452b, on the other hand, orbits a G2 star like the Sun with a period of  $384.843^{+0.007}_{-0.012}$  days, but its radius is  $1.63^{+0.23}_{-0.20} R_{\oplus}$  (Jenkins et al., 2015).

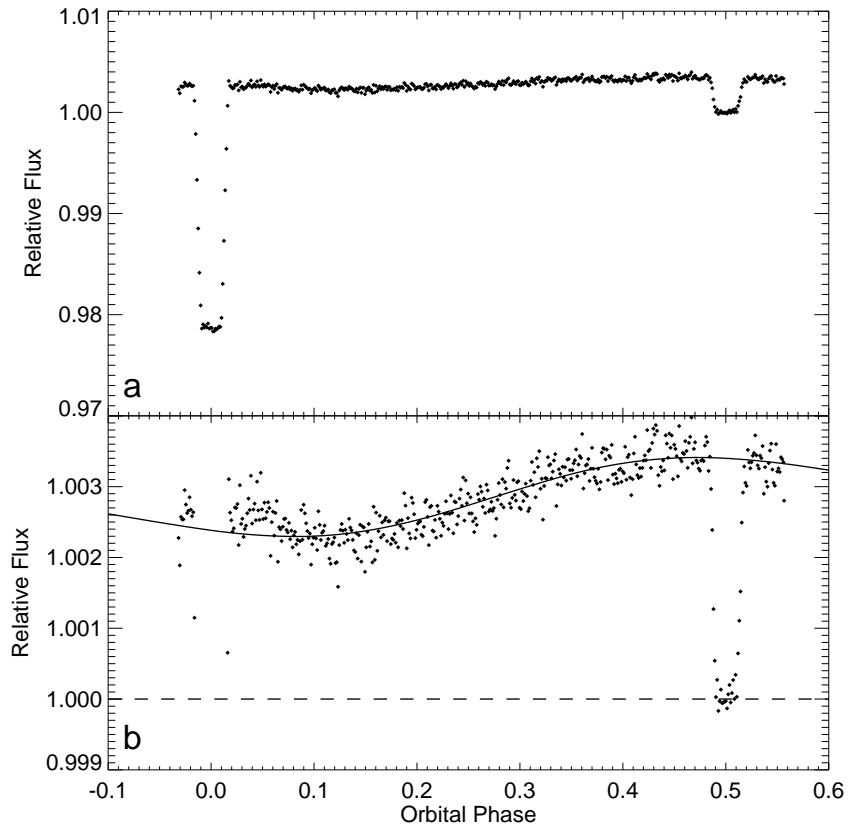


Figure 1.4 Adapted from [Knutson et al. \(2007\)](#). The top panel shows the phase curve for HD 189733b, from just before transit to just after secondary eclipse, measured at  $8 \mu\text{m}$  with Spitzer. The bottom panel zooms in to better show the subtle variation between the nightside (at transit) and the dayside (at secondary eclipse). Overplotted is the model fit, including the slight shift of the peak brightness to just before secondary eclipse.

The *Kepler* mission produced several surprises, one of which being that the most common type of planet in our neighborhood has no analog in our solar system. Of the 4,000 candidates discovered by the mission since launch, 2290 are less than  $2 R_{\oplus}$  in radius, and 1580 are between 2 and  $6 R_{\oplus}$  in radius<sup>3</sup>. The transition from terrestrial planets with outgassed, secondary atmospheres to mini-Neptune ice giants with accreted, H<sub>2</sub>-rich, primordial atmospheres occurs somewhere in the range of 1.5 to  $1.7 R_{\oplus}$  (e.g. Lopez & Fortney, 2014; Rogers, 2015), but it is likely not a sharp transition. Understanding the divide between the Earth-like, rocky planets and the Neptune-like, gas giant planets offers clues to the formation processes that created these worlds and has important implications for the definition of habitable planets and  $\eta_{\oplus}$ . To that end, we need to understand the atmospheres of these planets. Mass measurements for the small fraction of targets bright enough for radial velocity follow-up, combined with the measured radii, do not provide enough information to definitively constrain the interior models of these worlds. Figure 1.5 shows the radius versus the mass of subsample of *Kepler* candidates with mass measurements, as well as some other sub-Neptune-sized planets with radius and mass measurements. Also plotted on the figure are the mass-radius relations for various compositions. Planets larger than about  $3 R_{\oplus}$  are clearly low density, like the gas giants in our solar system. Below that, uncertainties in the measurements mean that any composition is possible.

In principle, the atmospheres of these planets can be probed with transmis-

---

<sup>3</sup>Counts taken from the Exoplanet Archive at

[http://exoplanetarchive.ipac.caltech.edu/docs/counts\\_detail.html](http://exoplanetarchive.ipac.caltech.edu/docs/counts_detail.html)

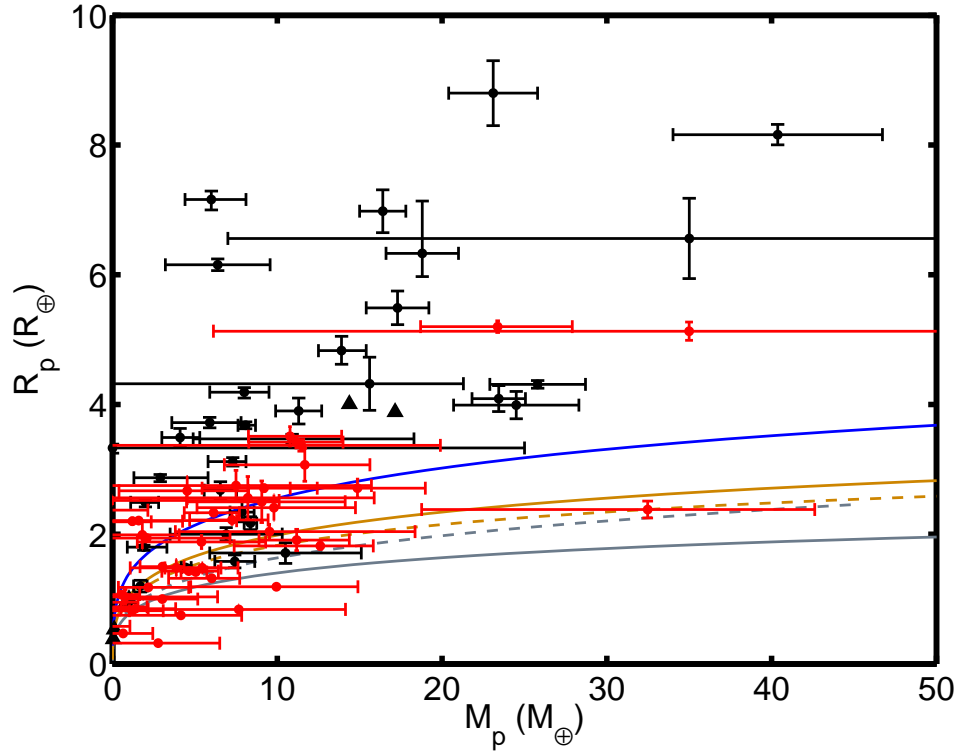


Figure 1.5 Adapted from [Rogers \(2015\)](#). This figure plots the mass and radius of planets for which both measurements exist. Planets from the *Kepler* mission are plotted in red. Solid lines indicate the mass-radius relation for planets of the following compositions: pure water (blue), pure  $\text{MgSiO}_3$  silicate (brown), and pure iron (grey). Dashed lines indicate the relation for an Earth-like composition (brown) and for rocky planets that have undergone collisional stripping ([Marcus et al., 2010](#)) (grey). Solar system planets are indicated with black triangles, and confirmed sub-Neptune transiting planets that are not from *Kepler* are indicated with black points.

sion spectroscopy. As the planet transits its star, stellar light passes through the atmosphere of the planet, imprinting any spectral features from the atmosphere, as shown in Fig. 1.1. This imprint results in a greater loss of flux at wavelengths where absorption features are strong, which manifests as a larger measured radius of the planet at those wavelengths. In practice, this is a difficult measurement to make, and, like radial velocity studies, it requires bright host stars. Further complicating the measurement is a degeneracy between scale height of the atmosphere and layers of clouds or haze. The best-studied mini-Neptune thus far is GJ 1214b. Only with 60 orbits of Hubble was its transmission spectrum measured well enough to determine that, indeed, a high-altitude cloud or haze layer was preventing light from reaching the lower layers of the atmosphere where the absorption features would be present (Kreidberg et al., 2014). A study of 10 hot Jupiters by Sing et al. (2016) shows a range of cloudiness in their atmospheres, with some being clear and others increasingly cloudy.

*Kepler* is a photometric mission, and most host stars in its data set are too faint for follow-up transmission spectroscopy measurements. The single, broadband light curves, however, still contain information about the atmospheres of *Kepler's* planet candidates which can be used to determine the average cloudiness and scale heights. The albedo and thermal emission information supplied by secondary eclipse measurements and phase curves provides constraints on the types of hazes or clouds that may be present, and perhaps even surface compositions in the case of the smallest planets. A sample of measured secondary eclipses in the *Kepler* data is given in Table 1.2. Phase curves and secondary eclipses are easiest to measure for

large, close-in objects, so most of these individual secondary eclipse detections are hot Jupiters. Many of these hot Jupiters are dark, as expected from theory, likely due to absorption by alkali metals (Sudarsky et al., 2000). Kipping & Spiegel (2011) used the amplitude of the phase curve in *Kepler* data for TrES-2b to determine that the geometric albedo, if only due to reflected light, is  $0.0253 \pm 0.0072$ . The authors conclude that the true geometric albedo must be even lower, less than 1%, since there is a significant thermal component. Other low-albedo hot Jupiters from the mission include Kepler-423b ( $A_g = 0.055 \pm 0.028$ , Gandolfi et al. (2015)), Kepler-12b ( $A_g = 0.14 \pm 0.04$ , Fortney et al. (2011)), and HAT-P-7b ( $A_g \lesssim 0.03$ , Morris et al. (2013)), and others listed in Table 1.2. Some hot Jupiters have been found to be bright, however, even at the same equilibrium temperatures as the dark planets. Examples include Kepler-7b ( $A_g = 0.32 \pm 0.03$ , Demory et al. (2011)), Kepler-13Ab ( $A_g = 0.33^{+0.04}_{-0.06}$ , Shporer et al. (2014)), and others listed in Table 1.2. Further examples of detected secondary eclipses of hot Jupiters in *Kepler* data can be found in Angerhausen et al. (2015) and Coughlin & López-Morales (2012). The study by Esteves et al. (2015) also reports a shift in the peak brightness of the phase curves for six hot Jupiters in their sample, noting that the hottest two planets, Kepler-76b and HAT-P-7b, have the brightness shifted toward the evening-side of the planet, while the cooler four (Kepler-7b, Kepler-8b, Kepler-12b, and Kepler-41b) have the shift toward the morning-side of the planet. If this correlation between the direction of the shift and the temperature of the planet holds, it indicates that the hottest two planets are likely clear atmospheres dominated by thermal emission from a substellar hot spot shifted slightly east, while the cooler planets are dominated by

reflected light from clouds that are present in the cooler western hemisphere.

The secondary eclipses of smaller planets are more difficult to detect with *Kepler*. Kepler-10b is one of only a few super-Earths in the *Kepler* data set that orbits a star bright enough that the secondary eclipse stands out above the noise (Demory, 2014; Sanchis-Ojeda et al., 2013, 2014). It is a  $1.4 R_{\oplus}$  planet in very close orbit around its host star (Batalha et al., 2011). It is expected to be too hot to have more than a tenuous atmosphere, and it may even have a molten surface. Its light curve is shown in Fig. 1.6. Kepler-10b is also an interesting exception in that the secondary eclipse depth is quite strong, suggesting a high geometric albedo of 0.4 to 0.6 (e.g. Batalha et al., 2011; Demory, 2014; Fogtman-Schulz et al., 2014; Hu et al., 2015; Rouan et al., 2011; Sanchis-Ojeda et al., 2014; Sheets & Deming, 2014), which is much higher than the albedos predicted and measured for larger planets at similar equilibrium temperatures (e.g. Coughlin & López-Morales, 2012; Esteves et al., 2013; Sudarsky et al., 2000). The remaining super-Earths with measured secondary eclipses in *Kepler* data are Kepler-78b (Sanchis-Ojeda et al., 2013), Kepler-93b (Demory, 2014), and KOI 1169.01 (Demory, 2014). They are detectable only because they are bright planets, with  $A_g$  greater than 0.25, orbiting bright stars.

Light from the host star can also refract through the atmosphere of the planet just before and just after transit. Depending on the viewing geometry, this light may be bent toward an observer, resulting in a slight increase in flux, above the level of the host star plus the night side of the planet, just outside of transit. This effect has been observed, as well as resolved spatially, during transits of Venus

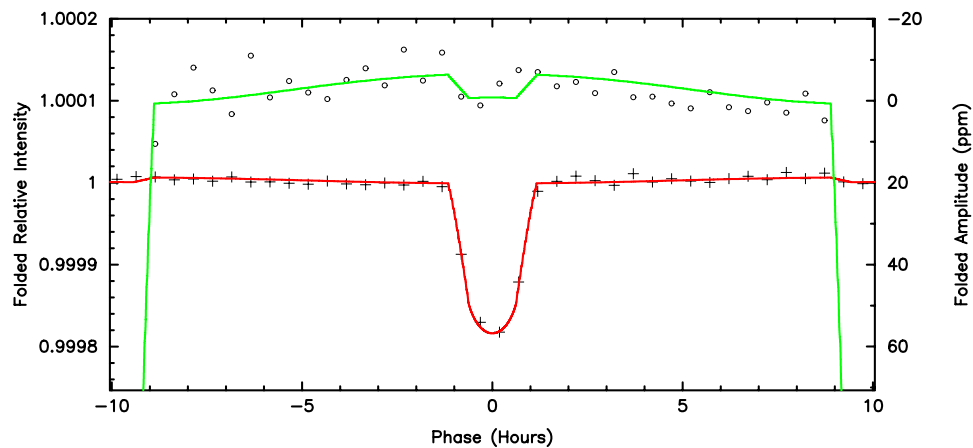


Figure 1.6 Adapted from [Batalha et al. \(2011\)](#). This figure shows the light curve for Kepler-10b, a hot Super-Earth. Crosses represent the data phase-folded on the center of the transit, while circles show the same data phase-folded on the center of the secondary eclipse. Note that the phase scale here is given in hours before or after the reference time, rather than on the dimensionless scale from 0 to 1. The red line is the model fit for the crosses, and the vertical scale is read from the left side. The green line is the model fit for the circles, and the vertical scale is read from the right side. The scale for the green model and the circles are greatly magnified to show the secondary eclipse, which is very shallow compared to the transit.

Table 1.2. Individual Detections of Secondary Eclipses in *Kepler* Data

KOI	Confirmed Name	$R_p^a$ ( $R_\oplus$ )	$(R_p/a)^{2a}$ (ppm)	Depth <sup>a</sup> (ppm)	$A_g$	Source
1.01	TrES-2b	13.68	251.73	$7.7 \pm 2.6$	$0.031 \pm 0.010$	<a href="#">Esteves et al. (2015)</a>
2.01	HAT-P-7b	$15.57^b$	349.5	$69.1 \pm 3.8$	$\lesssim 0.03$	<a href="#">Morris et al. (2013)</a>
10.01	Kepler-8b	15.31	191.3	$26.2 \pm 5.6$	$0.137 \pm 0.029$	<a href="#">Esteves et al. (2013)</a>
13.01	Kepler-13Ab	15.43	362.20	$90.81 \pm 0.27$	$0.33 \pm 0.06$	<a href="#">Shporer et al. (2014)</a>
17.01	Kepler-6b	14.83	194.38	$22 \pm 7$	$0.11 \pm 0.04$	<a href="#">Désert et al. (2011)</a>
18.01	Kepler-5b	16.04	182.87	$21 \pm 6$	$0.12 \pm 0.04$	<a href="#">Désert et al. (2011)</a>
20.01	Kepler-12b	18.60	202.96	$31 \pm 8$	$0.14 \pm 0.04$	<a href="#">Fortney et al. (2011)</a>
72.01	Kepler-10b	1.42	12.86	$5.8 \pm 2.5$	$0.61 \pm 0.17$	<a href="#">Batalha et al. (2011)</a>
69.01	Kepler-93b	1.51	2.45	$2.2 \pm 0.8$	0.87-0.88	<a href="#">Demory (2014)</a>
97.01	Kepler-7b	17.71	145.83	$44 \pm 5$	$0.32 \pm 0.03$	<a href="#">Demory et al. (2011)</a>
135.01	Kepler-43b	13.17	$153.01^c$	$17.0 \pm 5.3$	$0.06 \pm 0.02$	<a href="#">Angerhausen et al. (2015)</a>
183.01	Kepler-423b	13.08	241.58	$14.2 \pm 6.6$	$0.055 \pm 0.028$	<a href="#">Gandolfi et al. (2015)</a>
196.01	Kepler-41b	9.77	193.74	$64 \pm 12$	$0.30 \pm 0.07$	<a href="#">Santerne et al. (2011)</a>
202.01	Kepler-412b	14.54	457.39	$47.4 \pm 7.4$	0.013-0.094	<a href="#">Deleuil et al. (2014)</a>
1169.01	...	1.26	19.2	$13.5 \pm 3.1$	0.48-0.67	<a href="#">Demory (2014)</a>
1658.01	Kepler-76b	13.72	$535.49^c$	$75.6 \pm 5.6$	$0.22 \pm 0.02$	<a href="#">Angerhausen et al. (2015)</a>
2133.01	Kepler-91b	15.00	76.35	$35 \pm 18$	$0.46 \pm 0.30$	<a href="#">Esteves et al. (2015)</a>
... <sup>d</sup>	Kepler-78b	1.16	22.4	$10.5 \pm 1.2$	$0.27-0.4^e$	<a href="#">Sanchis-Ojeda et al. (2013)</a>

<sup>a</sup>Values from the source paper unless otherwise noted. Asymmetric error bars are given as symmetric with the larger of the two uncertainties.

<sup>b</sup>Radius value from [Esteves et al. \(2015\)](#).

<sup>c</sup> $(R_p/a)^2$  calculated from [Esteves et al. \(2015\)](#).

<sup>d</sup>Kepler-78b does not have a KOI number, because it was not initially detected by the *Kepler* mission pipeline. It was discovered by an independent search of the data reported in [Sanchis-Ojeda et al. \(2013\)](#).

<sup>e</sup> $A_g$  estimated using  $A_g = (2/3)A_B$  from  $A_B$  given by the source paper.

(Pasachoff et al., 2011; Tanga et al., 2012), but it has not yet been detected in exoplanets. Sidis & Sari (2010) developed a simple model for refraction in the clear atmospheres of giant planets to predict the scale of the effect, and Misra & Meadows (2014) extended the model to smaller planets and incorporated potential clouds. Much like in transmission spectroscopy, a large scale height (corresponding to a low mean-molecular-weight atmosphere) leads to a larger signal, because there is a greater volume of atmosphere to interact with the light. A weak refraction signal would suggest either that high-altitude clouds or hazes are preventing light from passing through the atmosphere, or that an atmosphere with a small scale height (i.e. high mean molecular weight) is present, meaning that there is a smaller volume of atmosphere present to interact with.

Though the signal for secondary eclipses and refraction is too small compared to the noise for most systems with small planets in the *Kepler* data set when considered individually, planets with similar characteristics can be grouped and averaged, increasing the signal to noise ratio. This group average provides a hint as to whether the cloud or haze on GJ 1214b is typical of the planet class, as well as the smaller super-Earths and larger Neptune-like planets. A group average can also tell us whether Kepler-10b, with its oddly strong secondary eclipse, is typical of the hot, rocky super-Earths or truly an outlier. The *Kepler* planet candidates have a 10 per cent false positive rate (Fressin et al., 2013), where a false positive is typically some type of eclipsing binary star that mimics the light curve of a transiting planet. Treating the planet candidates in aggregate rather than individually also guards against putting too much weight on an individual system that may turn out to be

a false positive. [Lopez & Fortney \(2014\)](#) indicates that radius is a good indicator of bulk composition for exoplanets, and so planets of similar radius should be reasonably similar to each other. In this thesis, I use the availability of many candidates of similar radii, stacking their light curves to reduce the noise and to tease out a group-averaged secondary eclipse. This provides constraints on the average albedo of the group members, which then constrains models of any clouds or hazes that may be present. I also use this stacking technique to look for an average refraction signal, to tell whether the planet class is likely to be amenable to transmission spectroscopy.

## 1.1 Outline of Thesis

Chapter 1 provides background and motivation for this thesis. In Chapter 2<sup>4</sup>, I discuss the planet candidate selection, the treatment of the light curve data to prepare for averaging, and the results for the average secondary eclipse for a group of sub-Saturn (1 to 6  $R_{\oplus}$ ) candidates with light curves sampled at 1 min cadence (i.e. short cadence). I also discuss the modeling of the reflected light and thermal emission, which is used to determine the average albedo for the group. In Chapter 3, I discuss the modifications required to work with the 30 min cadence (i.e. long cadence) data, which contains many more candidates but degrades the shape of the secondary eclipse. More available candidates means that the radius groups are more narrowly defined, with groups of 1 to 2  $R_{\oplus}$  (super-Earths), 2 to 4  $R_{\oplus}$  (mini-Neptune

---

<sup>4</sup>Chapter included as published in the *Astrophysical Journal* with minor edits for consistency with other chapters.

and Neptune-like), and 4 to 6  $R_{\oplus}$  (Neptune-like and super-Neptune). I present the results of the average secondary eclipse for the three groups and the modeling to determine their average albedos. In Chapter 4, I discuss early work I have done investigating and predicting the strength of the refraction effect on the light curves of exoplanets using a simple model based on [Sidis & Sari \(2010\)](#). I also discuss the similarities and differences in preparing the data for averaging around transit, rather than around secondary eclipse. Furthermore, I discuss the work I will do in the future, using more sophisticated models to predict the strength of the refraction effect to compare to the results observed with the *Kepler* data set and other future missions. In Chapter 5<sup>5</sup>, I summarize the thesis.

---

<sup>5</sup>A portion of this chapter is taken from the published version of Chapter 2 in the *Astrophysical Journal* with minor edits for consistency.

## Chapter 2: Statistical Eclipses of Short Cadence Close-in *Kepler* Sub-Saturns

### 2.1 Introduction

Secondary eclipses have been detected in *Kepler* data for hot Jupiters (e.g. [Coughlin & López-Morales, 2012](#); [Esteves et al., 2013](#)), showing that these bodies have very low albedos, as predicted by atmospheric models ([Sudarsky et al., 2000](#)). For super-Earth-sized planets, eclipses were first detected with *Kepler* in the two extremely hot, close-in planets Kepler-10b ([Batalha et al., 2011](#)) and Kepler-78b ([Sanchis-Ojeda et al., 2013](#)). Unlike the hot Jupiters, these two planets show relatively high geometric albedos, between 0.3 and 0.6. These planets are unlikely to harbor substantial atmospheres at such extreme temperatures ( $> 1500$  K) and are possibly a new class of “lava ocean” planets ([Léger et al., 2011](#); [Rouan et al., 2011](#)). The *Kepler* data set contains many super-Earths and sub-Saturn-sized candidates at slightly less extreme temperatures. At slightly lower temperatures and greater distances from the host star, the eclipse signals from these candidates are much weaker. [Demory \(2014\)](#) constrains the geometric albedos for 27 super-Earth candidates in the *Kepler* catalog and finds that the albedos for these candidates

are statistically larger than those of hot Jupiters (0.16 to 0.30 versus 0.06 to 0.11), with a subset of unusually bright candidates like Kepler-10b, with albedos greater than 0.4. Only a few of the candidates Demory (2014) analyzed show significant eclipses, while the remainder of the sample had upper limits set for their albedos. The hierarchical Bayesian analysis of Demory (2014) also illustrates the potential for extracting information on the atmospheres of *Kepler's* planets using statistical techniques.

In this chapter, I introduce a statistical method wherein I average the photometric data from different planetary candidates, after linearly scaling their orbital phases so that their eclipses have the same temporal cadence. This method has two advantages. My grand average eclipse has a much higher signal-to-noise than even the stacked eclipses of individual planets, and I avoid the selection bias that could result from focusing on the most easily measured individual planets. I focus on objects of less than 6 Earth radii. I choose this cutoff in radius to study the smallest planets while still providing a large sample size.

This chapter is organized as follows. Section 2.2 describes how I select Kepler data for candidate planets, and how I process those data to obtain high fidelity for my grand average eclipses. Section 2.3 describes how I transform the individual eclipses so that they reinforce in the grand average, and Section 2.4 calculates models of reflected light and thermal emission for comparison to my results. Section 2.5 gives my results for my candidate list of sub-Saturn sized planets (2.5.1), for a control group (2.5.2), and it briefly discusses notable individual planets (2.5.3), and acknowledges the limitation of my technique (2.5.4). Section 2.6 discusses the

implications of my results for atmospheres and surfaces of sub-Saturn sized planets, and Section 2.7 summarizes my conclusions for this chapter.

## 2.2 *Kepler* Observations

I choose two groups of candidates with radii less than  $6 R_{\oplus}$  from the NASA Exoplanet Archive’s Kepler Objects of Interest table<sup>1</sup>, downloaded on December 17, 2013. I select the groups based on the expected depth of the candidate’s eclipse, if the eclipse was due solely to reflected light with a geometric albedo of 1. The depth of the eclipse is given by the albedo times  $(R_p/a)^2$ , where  $R_p$  is the radius of the planet and  $a$  is the orbital radius of the planet (cf. Section 2.4). The first group consists of 32 candidates with  $(R_p/a)^2 > 10$  ppm, which makes them more likely to be detectable even with low albedo. The objects in this group and their parameters are listed in Table 2.1. The second list of 376 candidates is the control list, with  $(R_p/a)^2 < 1$  ppm, which makes them undetectable. [Fressin et al. \(2013\)](#) determined that 90 percent of the planet candidates are likely real planets across all radii, with smaller planets having slightly better odds of being real. I use the short-cadence ( $\approx 60$  s exposure) PDC data from the Mikulski Archive for Space Telescopes (MAST<sup>2</sup>), for quarters 0 through 16. I initially normalize each light curve file for a given candidate by the mean flux outside of transit. I check if there are other candidates in addition to the candidate of interest in the system, and, if so, I mask out all the transits from those other candidates. I extract each individual eclipse from the

---

<sup>1</sup><http://exoplanetarchive.ipac.caltech.edu/>

<sup>2</sup><http://archive.stsci.edu/kepler/>

light curve file, and I include a span of time centered on the eclipse and covering six eclipse durations. For each extracted eclipse, I refine the normalization by fitting a line across the out-of-eclipse section to determine the baseline and dividing by the fit. I assume the orbits are circular, and therefore the eclipses are centered at phase 0.5. I expect these planets to have circularized, based on the finding of [Kane et al. \(2012\)](#) that smaller *Kepler* candidates have a low mean eccentricity. I use a  $3\sigma$  clip to exclude unusually high or low points. I include only eclipses with at least 20 points out of eclipse on each side of the eclipse, as well as 40 points within eclipse. I apply this cut to ensure that I am adding eclipses with a well-determined out-of-eclipse baseline level and with information during eclipse.

The *Kepler* light curves occasionally contain discontinuities and ramps in flux due to systematic effects from the spacecraft and sudden changes in pixel sensitivity ([Christiansen et al., 2013](#)). I use the quickMAP PDC light curves ([Smith et al., 2012](#); [Stumpe et al., 2012](#); [Thompson et al., 2013](#)), which have largely been corrected for these effects. The PDC pipeline does not always catch every anomaly, however, so I must screen the data before use. I check each individual, normalized eclipse by applying three tests, which I refer to as the projection test, the slope test, and the red noise test.

In the projection test, I fit a line to the points before ingress, and then calculate the projection of that line for the points after egress. I take the mean of the actual data points after egress and a mean of the projected points from the linear fit. If the means differ by more than 0.001, the eclipse is dropped. I determined this value by trial and error, to balance the necessity of eliminating poorly fit eclipses, while

Table 2.1. Candidate Parameters

KOI	# eclipses	$R_p^a$ ( $R_\oplus$ )	$(R_p/a)^{2a}$ (ppm)	$a/R_*^a$	Max $T_{eq}^b$ (K)	Min $T_{eq}^c$ (K)	$T_{eff}$ (K)
Kepler-10b							
K00072.01	898	1.37	11.78	3.7	2659.0	1170.1	5627
$(R_p/a)^2 > 10$ ppm							
K00005.01	233	5.66	17.27	8.8	1786.8	786.3	5861
K00007.01	249	3.72	12.96	7.5	1939.0	853.3	5858
K00046.01	79	4.33	15.39	9.1	1721.9	757.8	5764
K00102.01 <sup>d</sup>	556	3.69	29.36	5.8	2194.0	965.5	5838
K00104.01	309	3.36	17.71	9.7	1391.4	612.3	4786
K00141.01	256	5.43	39.06	8.5	1678.4	738.6	5425
K00191.03	547	1.24	12.39	3.7	2688.0	1182.9	5696
K00240.01	18	4.20	11.39	11.2	1679.8	739.2	6215
K00299.01	473	1.98	10.52	5.0	2229.4	981.1	5538
K00356.01	11	5.73	75.96	3.8	2498.2	1099.4	5364
K00433.01	55	4.60	18.14	11.9	1377.1	606.0	5262
K00505.03	31	3.35	11.54	4.9	2073.8	912.6	5058
K00676.02	290	2.56	13.21	11.3	1171.8	515.6	4367
K00697.01	123	4.24	17.63	5.4	2238.8	985.2	5779
K00739.01	121	1.48	11.00	7.6	1361.6	599.2	4153
K00755.01	13	2.80	10.97	7.7	1933.1	850.7	5953
K00800.01	21	3.20	12.21	8.4	1920.9	845.3	6157
K00936.02	71	1.47	17.42	6.5	1358.3	597.7	3834
K01128.01	37	1.41	9.99	4.7	2295.2	1010.0	5480
K01169.01 <sup>e</sup>	41	1.49	15.73	3.4	2805.1	1234.4	5719
K01239.01	53	1.39	12.13	4.3	2548.2	1121.3	5849
K01300.01	336	1.34	22.62	4.1	2041.3	898.3	4602
K01367.01	236	1.41	25.04	3.7	2384.1	1049.1	5070
K01428.01	253	1.46	13.38	5.3	1899.9	836.1	4858
K01442.01	690	1.23	12.20	3.2	2749.2	1209.8	5476
K01510.01	40	1.47	15.31	5.3	1924.2	846.8	4885
K01784.01	13	5.20	15.09	13.8	1424.9	627.1	5853
K01805.01	51	5.60	11.61	10.1	1622.5	714.0	5708
K01835.02	51	2.92	14.20	3.9	2325.2	1023.2	5110
K02678.01	8	4.30	15.85	6.2	1945.5	856.1	5371
K02700.01	75	1.12	8.89	6.0	1635.9	719.9	4433

<sup>a</sup> $R_p$ ,  $a$ , and  $R_*$  are taken from the Exoplanet Archive candidate table, and  $(R_p/a)^2$  and  $a/R_*$  are calculated from them.

<sup>b</sup>Assumes  $f = 2/3$  (instant re-radiation) and  $A_B = 0.0$ .

<sup>c</sup>Assumes  $f = 1/4$  (complete redistribution) and  $A_B = 0.9$  (i.e.  $A_g = 0.6$ ).

<sup>d</sup>Coughlin & López-Morales (2012) find an eclipse depth of  $13.6_{-9.86}^{+8.83}$  ppm, consistent with the depth of  $7.43_{-2.30}^{+2.32}$  found in this work.

<sup>e</sup>Demory (2014) finds an eclipse depth of  $13.5_{-3.1}^{+3.0}$  ppm, using long cadence data. With the more limited amount of short cadence data, I find a depth of  $20.31_{-14.35}^{+14.31}$  ppm, consistent with the higher-precision measurement.

maintaining a significant sample size. I repeat the test, fitting a line to the points after egress and projecting that fit to the points before ingress. The eclipse is dropped if it fails either part of this test; it need not fail both parts. This test eliminates eclipses in which there is an offset in the out of eclipse baseline due to instrumental effects. It also helps to eliminate eclipses in cases where the approximation of a linear baseline across the eclipse was not adequate for the normalization.

In the slope test, I compare the slopes of the two lines fitted during the projection test. I expect the slopes to be zero, since I have already normalized with a straight line. If both slopes are consistent with zero within the  $3\sigma$  uncertainties on the fits, the eclipse is kept. Since the noise in any single eclipse is quite large, this test is not sensitive enough to accidentally eliminate eclipses due to phase variations.

I implement the red noise test by calculating the standard deviation of the light curve section under consideration when it is binned by 3, 5, 7, 9, 11, 13, and 15 points. Random noise, like photon-counting, should follow a  $\log(\sigma) \propto -0.5 \cdot \log(N)$  relation. For each individual eclipse, I fit a line to  $\log(\sigma)$  versus  $\log(N)$ . I expect the distribution of the slope of this fit to be a Gaussian distribution around  $-0.5$ , if the noise in the eclipses is random noise. I compile the distribution of fitted slopes for all eclipses in the group being averaged that pass the projection test. I then fit a Gaussian distribution to the histogram of slopes and estimate the cutoff value at which the distribution appears to deviate from the Gaussian fit. I then eliminate any individual eclipse with a slope greater than the cutoff. For my group of close-in candidates, this cutoff slope value is  $-0.30$ , while for the control group, it is  $-0.35$ . I eliminated KOI 3.01 (a.k.a Kepler-3b, HAT-P-11b) and KOI 2276.01 from the

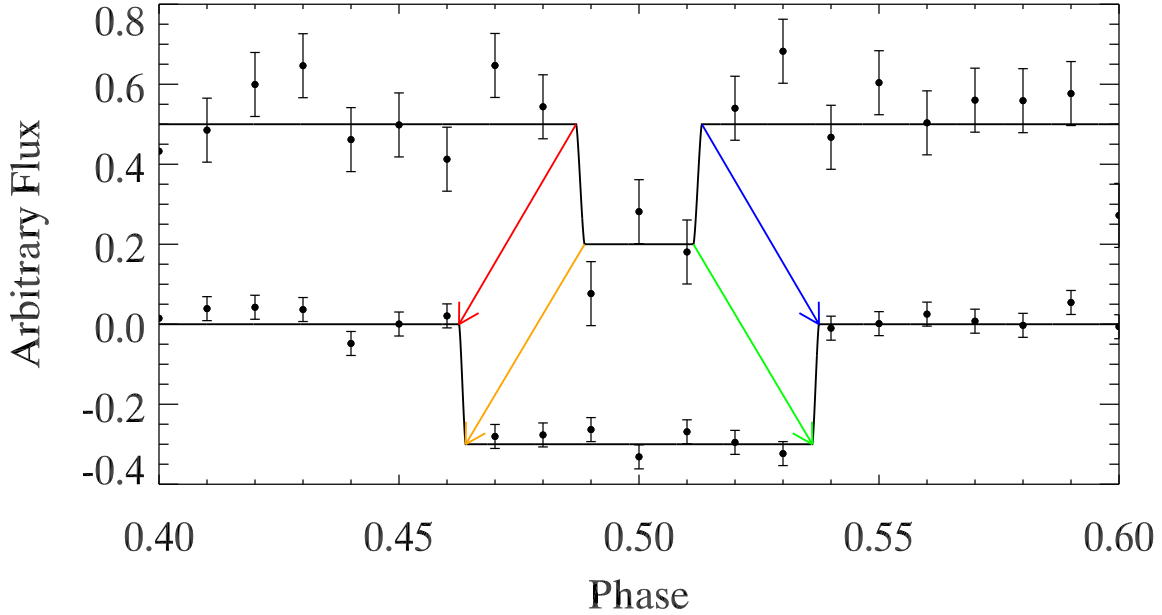


Figure 2.1 A visualization of the rescaling of the phase to the reference object, using simulated data. The top light curve is a single eclipse from one candidate, which is rescaled to the phase of the reference object and added into the group average, shown in the bottom light curve. The phase of the single eclipse is broken into segments: 0.25 to 1st contact, 1st contact to 2nd contact (ingress), 2nd contact to 3rd contact (full eclipse), 3rd contact to last contact (egress), and last contact to 0.75.

close-in group entirely because these two candidates have a very high rate of failure for the red noise test. For KOI 3.01, 177 of 207 eclipses (85.5 %) fail this test, while for KOI 2276.01, 234 of 319 eclipses (73.4 %) fail.

### 2.3 Averaging Candidate Light Curves

To constructively add the eclipses of multiple objects, I adopt the candidate from the group being averaged with the largest duration eclipse in phase to serve as a reference object. Then I transform the phase of all other objects in the group by

scaling sections of the light curve phase for each candidate to the reference object. Figure 2.1 shows how I break up the light curve into segments for scaling. Fixed points for the transforms are phase equal to 0.25, 0.5, and 0.75, i.e. a phase of exactly 0.25, 0.5, or 0.75 is transformed to be the same in the original coordinate and the transformed coordinate. The other reference points are 1st, 2nd, 3rd, and 4th contacts. I choose these points so that ingress, egress, and full eclipse will add constructively in the transformed phase. I also impose the cutoffs at 0.25 and 0.75 in phase because, for a simple circular orbit with reflected light, these points are where the inflection point for the phase curve of the planet would be located. I transform the phase using the following equations:

$$\psi = \psi_{1st} + (\phi - \phi_{1st}) * \frac{\psi_{1st} - 0.25}{\phi_{1st} - 0.25}, \quad (0.25 < \phi < \phi_{1st}) \quad (2.1)$$

$$\psi = \psi_{2nd} + (\phi - \phi_{2nd}) * \frac{\psi_{2nd} - \psi_{1st}}{\phi_{2nd} - \phi_{1st}}, \quad (\phi_{1st} < \phi < \phi_{2nd}) \quad (2.2)$$

$$\psi = 0.5 + (\phi - 0.5) * \frac{0.5 - \psi_{2nd}}{0.5 - \phi_{2nd}}, \quad (\phi_{2nd} < \phi < 0.5) \quad (2.3)$$

$$\psi = 0.5 + (\phi - 0.5) * \frac{\psi_{3rd} - 0.5}{\phi_{3rd} - 0.5}, \quad (0.5 < \phi < \phi_{3rd}) \quad (2.4)$$

$$\psi = \psi_{3rd} + (\phi - \phi_{3rd}) * \frac{\psi_{4th} - \psi_{3rd}}{\phi_{4th} - \phi_{3rd}}, \quad (\phi_{3rd} < \phi < \phi_{4th}) \quad (2.5)$$

$$\psi = \psi_{4th} + (\phi - \phi_{4th}) * \frac{0.75 - \psi_{4th}}{0.75 - \phi_{4th}}, \quad (\phi_{4th} < \phi < 0.75) \quad (2.6)$$

where  $\psi$  is the transformed phase,  $\phi$  is the native phase for the object,  $\psi_{1st}$ ,  $\psi_{2nd}$ ,  $\psi_{3rd}$ , and  $\psi_{4th}$  are the contact points in phase for the reference object, and  $\phi_{1st}$ ,  $\phi_{2nd}$ ,  $\phi_{3rd}$ , and  $\phi_{4th}$  are the contact points in the native phase of the object. The contact points, assuming circular orbits, are calculated using Equations 14 and 15 from

Winn (2010):

$$T_{tot} = \frac{P}{\pi} \sin^{-1} \left[ \frac{R_* \sqrt{(1+k)^2 - b^2}}{a \sin i} \right] \quad (2.7)$$

$$T_{full} = \frac{P}{\pi} \sin^{-1} \left[ \frac{R_* \sqrt{(1-k)^2 - b^2}}{a \sin i} \right] \quad (2.8)$$

where  $T_{tot}$  is the time between first and last contact,  $T_{full}$  is the time between second and third contact,  $b$  is the impact parameter,  $P$  is the period of the planet,  $i$  is the inclination of the planet's orbit,  $a$  is the orbital distance of the planet,  $R_*$  is the radius of the star, and  $k = R_p/R_*$  with  $R_p$  being the radius of the planet. I use  $b$ ,  $P$ ,  $a$ ,  $R_*$ , and  $R_p$  from the Exoplanet Archive candidate table and calculate  $i$  and  $R_p/R_*$  from those values. I then bin the normalized flux data using this scaled phase coordinate and average the points in each bin, weighted by their photometric errors. The bin size is chosen such that there are 11 bins within full eclipse. Ingress and egress are each given their own bin, as well, which results in a different bin size for these two bins.

## 2.4 Reflected and Thermal Light Modeling

I calculate the reflected light contribution using Equation 1.1, and I add to this the thermal emission component.

To calculate the thermal emission from the planet, I first estimate the effective temperature of the planet, using Equation 1.2, as in, [Esteves et al. \(e.g. 2013\)](#); [López-Morales & Seager \(e.g. 2007\)](#); [Rowe et al. \(e.g. 2006\)](#). I then adopt a black-body spectrum for that effective temperature, integrating over the wavelength range

of *Kepler*, accounting for its transmission function<sup>3</sup>. I adopt  $A_B = (3/2)A_g$  for a Lambert sphere, as in [Esteves et al. \(2013\)](#) and [López-Morales & Seager \(2007\)](#), and I do this calculation for the cases of  $f = 1/4$  and  $f = 2/3$ , with  $A_g = 0.0, 0.1, 0.3,$  and  $0.6$ . I then normalize by the stellar flux and multiply by  $(R_p/R_*)^2$ . I calculate the stellar flux for the close-in group by integrating over an ATLAS<sup>4</sup> model atmosphere ([Kurucz, 1979](#)) for the stellar effective temperature of each candidate’s host, modified by the instrument’s transmission function. For the control group, I integrate over a blackbody spectrum with the stellar effective temperature, rather than a model atmosphere. I use the planetary and stellar parameters from the NASA Exoplanet Archive candidate table, which includes the revised effective stellar temperatures from [Pinsonneault et al. \(2012\)](#) and [Buchhave et al. \(2012\)](#). Some of the KOIs in the candidate table also have updated effective temperatures based on the methods of [Valenti & Piskunov \(1996\)](#).

## 2.5 Results and Discussion

### 2.5.1 Close-in Candidates

Figure [2.2](#) shows the result for the list of 31 close-in candidates, with parameters in [Table 2.1](#), with  $(R_p/a)^2 > 10$  ppm, containing 5340 individual eclipses and excluding Kepler-10b. The bin size is approximately 0.0078 in phase, except for the two bins that contain ingress and egress. Ingress and egress are binned separately,

---

<sup>3</sup>[http://keplergo.arc.nasa.gov/kepler\\_response\\_hires1.txt](http://keplergo.arc.nasa.gov/kepler_response_hires1.txt)

<sup>4</sup><http://kurucz.harvard.edu/>

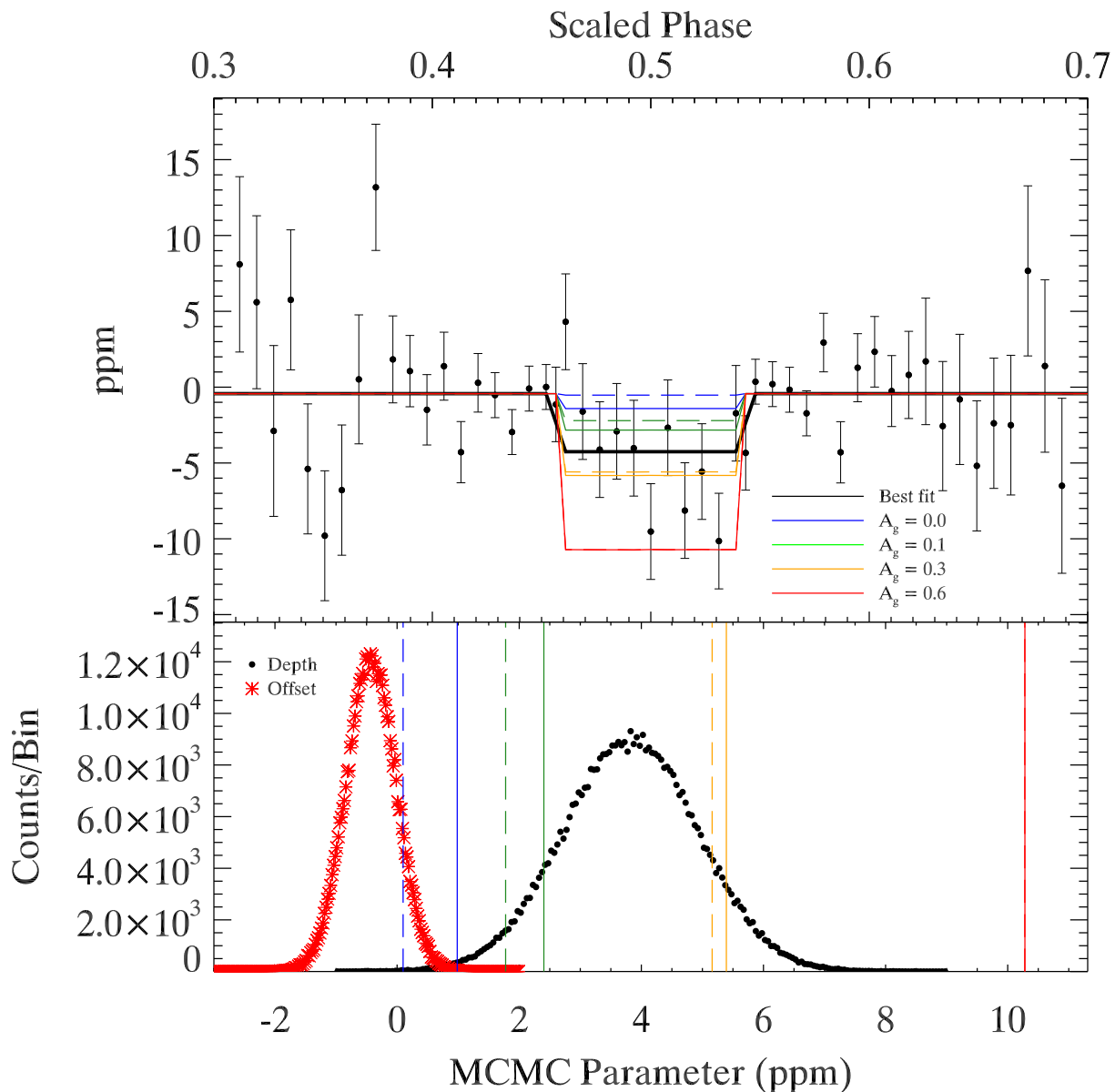


Figure 2.2 Upper panel: The light curve, centered on secondary eclipse, for the group of objects less than  $6 R_{\oplus}$  with  $(R_p/a)^2 > 10$  ppm, excluding Kepler-10b. The binned data are shown as points. The error bars are the propagated photometric errors. The best fit curve is the solid black line. Overplotted are the reflected light plus thermal emission models for  $A_g = (2/3) * A_B = 0.0$  (blue), 0.1 (green), 0.3 (orange), and 0.6 (red), with the re-radiation factor  $f = 1/4$  (dashed) and  $2/3$  (solid). Lower panel: The distributions for the two parameters of the MCMC run, with the depths from the reflected light plus thermal emission from the upper panel plotted as vertical lines. The two fitted parameters are eclipse depth ( $3.83^{+1.10}_{-1.11}$  ppm) and continuum offset from zero ( $-0.43 \pm 0.41$ ).

resulting in smaller bin sizes for these two points. To determine the probability distribution of eclipse depths, I implement in IDL a simple Markov Chain Monte Carlo (MCMC) procedure with 500,000 steps, fitting the equation  $F_b + \delta x$ , where  $F_b$  allows for an offset from zero for the continuum of the light curve,  $x$  is the model eclipse curve from [Mandel & Agol \(2002\)](#), rescaled so that the continuum is zero and the full eclipse is -1, and  $\delta$  is the scale of the eclipse curve. I use the Bayesian information criterion (BIC, [Liddle, 2007](#)) to establish that the data in this case do not support the addition of a sinusoidal phase curve parameter. The eclipse depth is then the median value of  $\delta$ . Also included in [Figure 2.2](#) is the expected depth of the eclipse calculated from the reflected light plus thermal emission for a range of albedos, adopting  $A_g = (2/3)A_{Bond}$ . Error bars on the eclipse depth are set by the central 68.27% of values from the MCMC chain. The lower panel of [Figure 2.2](#) shows the distributions for the two parameters in the MCMC chain, with the vertical lines indicating the same calculated reflected plus thermal emission values from the upper panel. I find an average eclipse depth of  $3.83_{-1.11}^{+1.10}$  ppm. The weighted average of  $(R_p/a)^2$  for this group is 17.13 ppm, so if the eclipse is due entirely to reflected light, the average geometric albedo is  $0.22 \pm 0.06$ . I have excluded Kepler-10b from this group, since it has an eclipse detectable when considered alone ([Batalha et al., 2011](#); [Demory, 2014](#); [Fogtman-Schulz et al., 2014](#); [Rouan et al., 2011](#)), and the host star is quite bright, at a magnitude in the *Kepler* bandpass of 9.12, allowing it to dominate the weighted average. Note that Kepler-78b does not have short cadence data, so it is not included either. Including Kepler-10b in the average results in a larger eclipse depth of  $5.08_{-0.72}^{+0.71}$  ppm, consistent with a higher albedo of  $0.37 \pm 0.05$

if due solely to reflected light. Since Kepler-10b is highly reflective, and the host star Kepler-10 is so bright, its inclusion greatly influences the average.

Allowing for thermal emission from the planets in the *Kepler* bandpass does not change the average geometric albedo appreciably. Including thermal emission requires adjusting the geometric albedo downward slightly. I calculated the expected eclipse depth given my average geometric albedo, including thermal emission, which was slightly deeper than the average eclipse depth from the data. I only need to adjust the geometric albedo downward by 0.001-0.002 (2-3%) to match the average eclipse depth from the data in the case of full redistribution of heat, while I need to adjust it downward by 0.026 to 0.027 (7%) to match in the case of instantaneous re-radiation. These values are less than the uncertainty in the average geometric albedo that I derived from reflected light only.

My average geometric albedo depends on accurate planet radii. It is known that cooler stars ( $\lesssim 4500$  K) in the original *Kepler* Input Catalog (KIC) have more poorly-determined parameters (Brown et al., 2011), and uncertain stellar radii translate to uncertain planet radii. To check how this affects my average, I determined the average geometric albedo for the close-in objects, excluding Kepler-10b, around stars that are  $\geq 5000$  K, and also for those around stars that are  $\geq 4500$  K. For the 5000 K group, I find an average eclipse depth of  $4.25^{+1.16}_{-1.15}$  ppm, corresponding to a geometric albedo of  $0.25 \pm 0.07$ . For the 4500 K group, I find an average eclipse depth of  $3.74 \pm 1.11$  ppm, corresponding to a geometric albedo of  $0.22 \pm 0.06$ . Table 2.2 summarizes the results for these sub-groupings as well as other sub-groupings which follow. These are consistent with the result above for the

Table 2.2. Eclipse depths and albedos

Group	Avg Eclipse Depth (ppm)	Avg $A_g$
Close-in, $(R_p/a)^2 > 10$ ppm		
without Kepler-10b	$3.83^{+1.10}_{-1.11}$	$0.22 \pm 0.06$
with Kepler-10b	$5.08^{+0.71}_{-0.72}$	$0.37 \pm 0.05$
$T_{eff} > 5000$ K	$4.25^{+1.16}_{-1.15}$	$0.25 \pm 0.07$
$T_{eff} > 4500$ K	$3.74 \pm 1.11$	$0.22 \pm 0.06$
$R_p < 2R_{\oplus}$ <sup>a</sup>	$2.14 \pm 1.96$	$0.17 \pm 0.16$
$2R_{\oplus} < R_p < 6R_{\oplus}$	$4.68 \pm 1.22$	$0.23 \pm 0.06$
Control, $(R_p/a)^2 < 1$ ppm		
376 candidates	$0.36 \pm 0.37$	$0.75 \pm 0.77$
31 candidates	$0.75^{+0.51}_{-0.50}$	$1.24^{+0.85}_{-0.83}$
Individual Candidates		
Kepler-10b	$7.08 \pm 1.06$	$0.60 \pm 0.09$
KOI 102.01	$7.43^{+2.32}_{-2.30}$	$0.25 \pm 0.08$
KOI 116.03	$8.04^{+3.71}_{-3.67}$	... <sup>b</sup>

<sup>a</sup>Excludes Kepler-10b.

<sup>b</sup>The calculated geometric albedo is unphysical.

full group, excluding Kepler-10b, so I conclude that the presence of planets orbiting cooler stars in my sample does not present an ambiguity when interpreting my results.

## 2.5.2 Control Group

Figure 2.3 shows the averaged light curve, containing 9249 individual eclipses, for the control group of objects with  $(R_p/a)^2 < 1$  ppm. The bin size is approximately 0.004 in phase. Using the same two-parameter equation as the close-in group for the MCMC run, I find an average eclipse depth of  $0.36 \pm 0.37$  ppm, which is consistent with no detection, as expected. This result cannot constrain the average geometric albedo for this group, which has a weighted average of  $(R_p/a)^2 = 0.48$  ppm. The

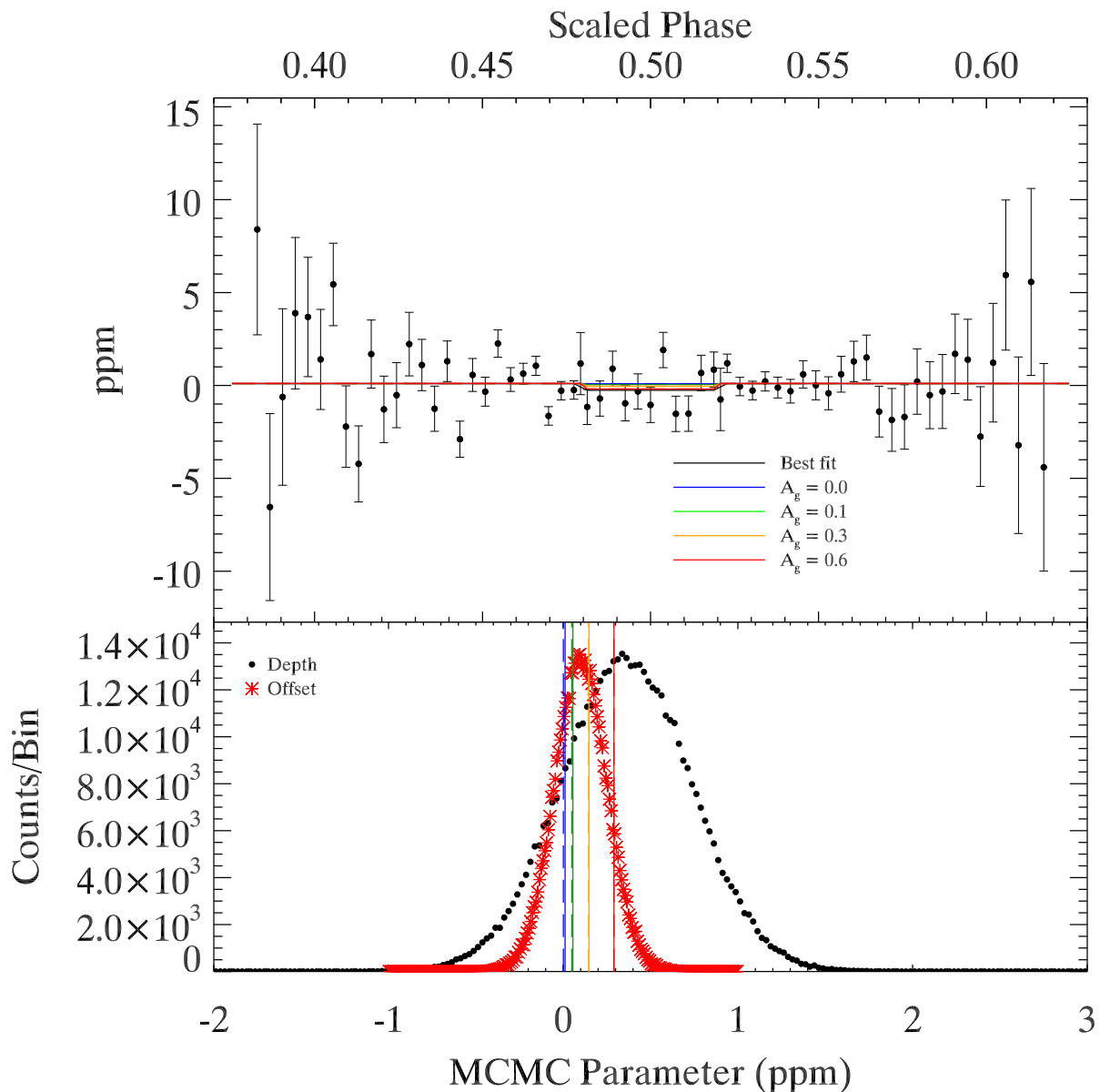


Figure 2.3 Upper panel: The light curve, centered on secondary eclipse, for the group of objects less than  $6 R_{\oplus}$  with  $(R_p/a)^2 < 1$  ppm. The binned data are shown as points. The error bars are the propagated photometric errors. The best fit curve is the solid black line. Overplotted are the reflected light plus thermal emission models for  $A_g = (2/3)A_B = 0.0$  (blue), 0.1 (green), 0.3 (orange), and 0.6 (red), with the re-radiation factor  $f = 1/4$  (dashed) and  $2/3$  (solid). Lower panel: The distributions for the two parameters of the MCMC run, with the depths from the reflected light plus thermal emission from the upper panel plotted as vertical lines. The two fitted parameters are eclipse depth ( $0.36 \pm 0.37$  ppm) and continuum offset from zero ( $0.10 \pm 0.15$  ppm).

candidates and their parameters are listed in Table 2.3.

To examine the effect that a smaller sample size, similar to that of my close-in group, would have on this result, I chose a subset of the control group randomly. For 31 candidates, noted in Table 2.3 with a footnote, I obtained 3059 eclipses, which resulted in an average eclipse depth of  $0.75^{+0.51}_{-0.50}$  ppm, again consistent with no detection. With the full control group, it is impractical to check the stacked eclipses of all of the candidates in the group. However, for the smaller control group, I found it both practical and important to screen it strongly for false positives, as I did for the close-in group discussed in Section 2.5.1. This screening identified one system (KOI 116) that I excluded, which I discuss further in Section 2.5.3.

Table 2.3. Control Group Candidate Parameters

KOI	# eclipses	$R_p^a$ ( $R_\oplus$ )	$(R_p/a)^{2a}$ (ppm)	$a/R_*^a$	Max $T_{eq}^b$ (K)	Min $T_{eq}^c$ (K)	$T_{eff}$ (K)
K00005.02 <sup>d</sup>	160	0.66	0.14	11.4	1571.3	691.4	5861
K00041.01	38	2.08	0.64	19.4	1211.9	533.3	5909
K00041.02	94	1.24	0.52	12.8	1494.4	657.6	5909
K00041.03	7	1.40	0.07	38.1	864.8	380.5	5909
K00042.01	5	2.71	0.67	22.3	1180.6	519.5	6170
K00046.02	40	0.96	0.37	13.0	1442.2	634.7	5764
K00070.04 <sup>d</sup>	144	0.91	0.38	14.4	1294.7	569.7	5443
K00070.05 <sup>d</sup>	43	1.03	0.10	31.4	878.0	386.4	5443
K00082.01	28	2.54	0.87	33.9	761.7	335.2	4908
K00082.02	40	1.34	0.44	25.1	884.6	389.3	4908
K00082.04	63	0.69	0.19	19.6	1002.2	441.0	4908
K00082.05	98	0.54	0.17	16.1	1106.2	486.8	4908
K00085.03 <sup>d</sup>	97	1.41	0.51	15.1	1435.5	631.7	6172
K00102.02 <sup>d</sup>	207	1.09	0.80	10.4	1638.5	721.0	5838
K00108.01	57	2.94	0.93	23.1	1123.1	494.2	5975
K00111.01 <sup>d</sup>	85	2.14	0.98	21.3	1118.7	492.3	5711
K00111.02 <sup>d</sup>	45	2.05	0.34	34.7	876.1	385.5	5711
K00115.03 <sup>d</sup>	230	0.64	0.34	7.5	2112.6	929.7	6398
K00117.01	47	2.93	1.00	22.8	1126.1	495.6	5949
K00117.04	89	1.08	0.31	15.1	1382.0	608.2	5949
K00118.01	19	1.69	0.19	38.6	858.7	377.9	5906
K00119.01	9	3.90	0.43	57.7	670.2	294.9	5632
K00123.02	45	2.71	0.57	23.0	1105.9	486.6	5871
K00124.02	19	3.59	0.58	27.2	1021.5	449.5	5899
K00148.03	20	2.35	0.19	55.7	628.3	276.5	5190
K00150.02	26	3.70	0.77	33.7	906.7	399.0	5822
K00152.02	33	3.10	0.49	36.8	954.6	420.1	6405
K00156.01 <sup>d</sup>	93	1.60	0.95	23.0	869.9	382.8	4619
K00156.02 <sup>d</sup>	138	1.18	0.93	17.1	1009.2	444.1	4619
K00157.02	54	3.20	0.76	31.7	913.0	401.8	5685
K00157.06	107	1.72	0.63	18.7	1188.9	523.2	5685
K00162.01	27	2.54	0.93	25.1	1049.3	461.7	5817
K00168.02 <sup>d</sup>	67	2.81	0.87	14.7	1446.4	636.5	6142
K00171.02	27	2.12	0.61	21.7	1260.0	554.5	6495
K00172.01	27	2.28	0.75	26.8	1028.0	452.4	5886
K00176.01	12	2.60	0.29	37.2	973.2	428.3	6568
K00177.01	17	1.84	0.28	30.2	946.2	416.4	5758
K00222.02	22	1.85	0.72	33.8	704.6	310.1	4533
K00232.03	44	1.82	0.25	34.4	940.5	413.9	6102
K00232.04	21	1.85	0.12	50.1	778.9	342.7	6102
K00238.01	11	2.50	0.61	27.9	1074.1	472.7	6274
K00241.01	8	2.23	0.80	30.8	860.8	378.8	5288
K00241.03	32	0.93	0.89	12.2	1367.6	601.8	5288
K00245.02	7	0.75	0.05	40.5	751.0	330.5	5288

Table 2.3 (cont'd)

KOI	# eclipses	$R_p^a$ ( $R_\oplus$ )	$(R_p/a)^{2a}$ (ppm)	$a/R_*$ <sup>a</sup>	Max $T_{eq}$ <sup>b</sup> (K)	Min $T_{eq}$ <sup>c</sup> (K)	$T_{eff}$ (K)
K00245.03	18	0.31	0.02	29.5	879.1	386.8	5288
K00246.02	43	1.11	0.27	15.8	1318.6	580.2	5793
K00247.01	13	1.94	0.82	38.3	577.3	254.0	3954
K00251.02	59	0.82	0.47	21.3	782.4	344.3	3996
K00255.02	48	0.80	0.14	37.5	...	...	... <sup>e</sup>
K00260.01 <sup>d</sup>	63	1.66	0.53	16.6	1368.8	602.3	6164
K00260.03 <sup>d</sup>	26	1.79	0.23	27.1	1069.1	470.5	6164
K00261.01	2	2.65	0.82	26.4	1000.3	440.2	5692
K00263.01	10	2.02	0.34	22.6	1106.8	487.0	5820
K00269.01	45	1.47	0.19	24.8	1155.8	508.6	6364
K00270.01	10	1.80	0.54	15.3	1281.7	564.0	5552
K00270.02	5	2.13	0.20	29.6	921.9	405.7	5552
K00271.02	6	2.33	0.24	34.2	953.0	419.4	6169
K00271.03	29	1.41	0.23	21.3	1206.7	531.0	6169
K00273.01 <sup>d</sup>	71	1.82	0.63	19.7	1178.4	518.6	5783
K00274.01	40	1.13	0.14	17.6	1310.8	576.8	6090
K00274.02	15	1.13	0.08	23.2	1143.1	503.0	6090
K00275.01	8	1.96	0.41	20.6	1154.8	508.2	5795
K00277.02 <sup>d</sup>	60	1.21	0.20	15.5	1371.0	603.3	5973
K00279.02	16	2.50	0.69	21.0	1265.0	556.7	6418
K00282.01	18	2.81	0.46	34.1	908.7	399.9	5873
K00282.02	59	1.03	0.30	15.5	1347.8	593.1	5873
K00283.01	39	2.41	0.66	26.2	1003.7	441.7	5687
K00283.02	11	0.84	0.04	35.6	861.6	379.2	5687
K00284.01	28	1.68	0.29	28.0	1012.1	445.4	5925
K00284.02	81	1.28	0.66	14.0	1431.3	629.9	5925
K00284.03	82	1.22	0.62	13.8	1442.1	634.6	5925
K00285.02	1	2.60	0.36	25.9	1045.2	459.9	5883
K00291.01	6	2.73	0.35	31.6	899.9	396.0	5600
K00294.01	3	2.30	0.21	44.7	827.8	364.3	6125
K00295.02	8	1.63	0.57	19.1	1226.7	539.8	5936
K00296.01	6	2.40	0.30	37.6	897.4	394.9	6089
K00298.01	11	1.43	0.18	31.0	938.4	413.0	5780
K00301.02	10	1.16	0.23	18.5	1331.8	586.0	6337
K00304.02 <sup>d</sup>	86	1.16	0.58	7.6	2021.5	889.6	6150
K00307.01	11	1.80	0.26	29.5	1021.5	449.5	6141
K00307.02	44	1.15	0.64	12.1	1596.4	702.5	6141
K00308.01	4	3.15	0.35	40.5	898.3	395.3	6323
K00312.01	9	1.91	0.58	19.0	1275.9	561.5	6158
K00312.02	5	1.84	0.34	23.8	1140.1	501.7	6158
K00313.01	27	2.21	0.49	33.6	833.8	366.9	5348
K00313.02	67	1.61	0.75	19.8	1085.9	477.9	5348
K00314.01	50	1.94	0.82	32.0	623.1	274.2	3900
K00314.03	67	0.79	0.20	26.4	686.4	302.1	3900

Table 2.3 (cont'd)

KOI	# eclipses	$R_p^a$ ( $R_\oplus$ )	$(R_p/a)^{2a}$ (ppm)	$a/R_*$ <sup>a</sup>	Max $T_{eq}$ <sup>b</sup> (K)	Min $T_{eq}$ <sup>c</sup> (K)	$T_{eff}$ (K)
K00316.01	35	2.63	0.79	23.0	1060.0	466.5	5622
K00321.02 <sup>d</sup>	188	0.84	0.44	10.5	1547.0	680.8	5538
K00332.02	11	0.56	0.12	17.5	...	...	... <sup>e</sup>
K00333.01	4	2.50	0.83	21.5	1273.8	560.6	6538
K00337.01	5	1.96	0.33	33.2	943.4	415.2	6014
K00339.02	8	2.06	0.61	23.2	1178.7	518.7	6278
K00343.03	8	1.58	0.08	44.3	779.5	343.0	5744
K00350.01	6	2.40	0.88	21.7	1167.1	513.6	6018
K00351.05	56	1.36	0.44	17.5	1367.7	601.9	6330
K00351.06	71	1.16	0.43	15.1	1473.1	648.2	6330
K00352.01	1	2.24	0.29	35.9	905.0	398.2	6002
K00354.01	33	2.36	0.62	26.4	1044.3	459.6	5935
K00354.02	73	1.22	0.47	15.7	1355.3	596.4	5935
K00369.01	5	1.33	0.71	12.9	1603.5	705.6	6377
K00369.02	3	1.26	0.31	18.5	1339.6	589.5	6377
K00370.01	12	4.32	0.50	28.4	1021.9	449.7	6022
K00370.02	31	2.65	0.43	18.7	1258.8	554.0	6022
K00385.01	2	2.06	0.70	23.8	1045.0	459.9	5639
K00386.01	4	3.40	0.52	38.4	905.7	398.6	6212
K00392.02	2	1.33	0.29	19.0	1222.5	538.0	5894
K00393.01	1	1.97	0.29	32.5	994.1	437.5	6269
K00416.01	10	3.00	1.01	37.4	775.4	341.2	5249
K00440.01	7	2.20	0.70	32.6	796.8	350.6	5031
K00446.01	27	1.86	0.51	38.0	678.7	298.7	4631
K00475.02	5	2.49	0.90	30.5	856.8	377.0	5236
K00490.03 <sup>d</sup>	82	1.54	0.99	20.3	985.0	433.5	4909
K00510.03	5	2.30	0.78	24.6	1009.0	444.0	5540
K00518.01	17	2.02	0.80	33.9	709.0	312.0	4565
K00523.02	10	2.90	0.31	44.8	836.3	368.0	6197
K00563.01	7	1.92	0.43	26.7	1078.8	474.7	6166
K00564.01	7	2.70	0.59	35.1	908.8	399.9	5956
K00564.03	16	1.41	0.80	15.7	1359.8	598.4	5956
K00567.02	35	2.40	0.50	34.8	891.0	392.1	5817
K00568.02 <sup>d</sup>	162	0.74	0.91	9.2	1604.1	705.9	5390
K00571.02	23	1.81	0.73	37.0	598.7	263.5	4031
K00574.01	3	2.53	0.63	40.6	740.0	325.6	5220
K00574.02	5	1.17	0.33	26.0	925.2	407.1	5220
K00584.02	12	2.08	0.37	39.0	799.4	351.8	5524
K00584.03	44	0.91	0.34	17.7	1184.9	521.4	5524
K00612.01	16	2.10	0.43	35.2	796.2	350.4	5231
K00623.01 <sup>d</sup>	80	1.40	0.45	16.2	1318.5	580.2	5877
K00623.02 <sup>d</sup>	48	1.36	0.25	21.3	1149.9	506.0	5877
K00623.03 <sup>d</sup>	133	1.18	0.73	10.8	1619.3	712.6	5877
K00623.04 <sup>d</sup>	32	1.12	0.09	29.2	983.3	432.7	5877

Table 2.3 (cont'd)

KOI	# eclipses	$R_p^a$ ( $R_\oplus$ )	$(R_p/a)^{2a}$ (ppm)	$a/R_*$ <sup>a</sup>	Max $T_{eq}^b$ (K)	Min $T_{eq}^c$ (K)	$T_{eff}$ (K)
K00624.01	4	2.37	0.59	33.1	898.5	395.4	5725
K00626.01	1	2.11	0.55	24.0	1136.5	500.1	6157
K00626.02	2	0.96	0.25	16.0	1389.0	611.2	6157
K00627.02	4	1.22	0.93	9.7	1778.2	782.5	6125
K00632.01	2	1.46	0.77	16.9	1193.3	525.1	5437
K00639.01	1	2.70	0.66	27.5	1108.1	487.6	6433
K00645.02	5	2.90	0.50	22.5	1200.2	528.2	6306
K00655.01	4	2.77	0.43	31.2	991.8	436.4	6133
K00657.02	22	2.05	0.62	36.2	715.0	314.7	4763
K00658.03	10	1.18	0.26	23.4	1106.6	487.0	5924
K00661.01	2	2.20	0.63	23.7	1131.4	497.9	6098
K00661.02	1	1.47	0.13	34.8	934.4	411.2	6098
K00662.01	3	2.10	0.91	19.1	1272.0	559.7	6148
K00664.01	3	1.98	0.59	18.6	1253.2	551.5	5986
K00664.02	3	1.29	0.51	13.0	1497.8	659.1	5986
K00670.01	3	1.77	0.79	17.2	1251.9	550.9	5754
K00671.02	43	1.23	0.50	16.4	1305.2	574.3	5845
K00671.03	18	1.45	0.25	27.4	1008.3	443.7	5845
K00671.04	31	1.17	0.27	21.2	1145.9	504.3	5845
K00672.02	4	4.03	0.56	49.5	709.7	312.3	5524
K00679.01	1	2.61	0.29	38.4	862.4	379.5	5913
K00679.02	4	0.94	0.09	24.5	1080.0	475.2	5913
K00689.01	2	1.96	0.46	31.9	870.3	383.0	5438
K00691.01	1	3.26	0.51	35.5	951.3	418.6	6277
K00691.02	1	1.39	0.21	23.7	1165.2	512.7	6277
K00693.01	2	2.04	0.20	38.8	921.5	405.5	6352
K00693.02	8	2.16	0.52	25.7	1131.5	497.9	6352
K00694.01	1	2.87	0.88	32.5	915.8	403.0	5779
K00695.01	1	2.80	0.37	36.8	927.5	408.1	6226
K00700.02 <sup>d</sup>	68	1.71	0.72	17.3	1287.0	566.3	5922
K00700.03 <sup>d</sup>	46	1.57	0.33	23.3	1108.1	487.6	5922
K00701.01	38	1.91	0.48	41.9	671.2	295.4	4807
K00701.02	120	1.23	0.94	19.3	988.0	434.8	4807
K00707.02	18	4.69	0.62	30.0	973.7	428.5	5904
K00707.03	19	4.10	0.67	25.3	1060.8	466.8	5904
K00708.01	10	2.73	0.72	28.1	1070.8	471.2	6278
K00709.01	1	2.16	0.39	36.3	848.1	373.2	5658
K00710.02	2	1.83	0.73	14.4	1582.3	696.3	6653
K00710.03	4	1.25	0.97	8.6	2054.1	903.9	6653
K00717.01	2	1.74	0.38	24.2	1045.2	459.9	5686
K00717.02	5	0.95	0.74	9.4	1677.0	738.0	5686
K00718.02	10	3.07	0.62	27.3	1001.8	440.8	5788
K00719.01	13	1.64	0.84	25.0	848.1	373.2	4689
K00719.04	41	0.81	0.59	14.8	1102.2	485.0	4689

Table 2.3 (cont'd)

KOI	# eclipses	$R_p^a$ ( $R_\oplus$ )	$(R_p/a)^{2a}$ (ppm)	$a/R_*$ <sup>a</sup>	Max $T_{eq}^b$ (K)	Min $T_{eq}^c$ (K)	$T_{eff}$ (K)
K00723.02	5	3.30	0.67	48.7	691.8	304.5	5342
K00730.02	32	1.98	0.92	18.4	1229.3	541.0	5832
K00730.03	12	2.50	0.58	29.2	974.6	428.9	5832
K00730.04	23	1.64	0.92	15.2	1349.7	593.9	5832
K00749.03	25	1.42	0.62	20.4	1110.9	488.8	5559
K00759.01	2	4.20	0.85	50.3	714.7	314.5	5608
K00775.01	4	1.93	0.61	41.2	594.3	261.5	4222
K00812.02	5	2.10	0.55	47.1	558.4	245.7	4243
K00812.04	17	1.28	0.73	24.9	767.7	337.8	4243
K00817.01	5	1.74	0.31	54.6	495.9	218.2	4055
K00829.01	17	3.10	0.88	31.3	983.5	432.8	6086
K00829.02	36	2.10	0.97	20.2	1224.2	538.7	6086
K00834.02	25	2.30	0.82	25.8	1027.8	452.3	5779
K00872.02	50	1.48	0.91	18.7	1105.8	486.6	5289
K00886.02	3	1.23	0.40	35.8	581.8	256.0	3855
K00898.03	5	2.36	0.64	44.6	628.5	276.6	4648
K00899.03	17	1.54	0.47	42.0	530.4	233.4	3803
K00904.02	2	1.56	0.18	55.4	547.5	240.9	4509
K00904.05	8	1.67	0.81	28.2	766.9	337.5	4509
K00907.02	9	3.80	0.75	36.9	873.2	384.2	5870
K00912.02	7	1.26	0.83	21.9	849.4	373.8	4397
K00921.02	16	2.90	0.96	38.2	752.9	331.3	5148
K00934.03	2	2.89	0.78	32.5	944.1	415.4	5956
K00935.04	52	1.96	0.79	17.6	1403.8	617.7	6514
K00939.04	5	1.62	0.53	23.0	1107.0	487.1	5870
K01001.01	9	4.80	0.63	22.8	1178.9	518.8	6235
K01060.01	18	2.02	0.59	19.4	1369.0	602.4	6678
K01060.03	7	1.96	0.28	27.6	1149.0	505.6	6678
K01060.04	23	1.46	0.52	14.9	1562.3	687.5	6678
K01102.03	9	3.00	0.83	26.9	1053.1	463.4	6043
K01113.01	3	2.90	0.48	34.1	977.4	430.1	6314
K01115.01	2	2.13	0.75	18.4	1198.8	527.5	5685
K01127.02	5	1.70	0.82	19.3	1151.2	506.6	5602
K01145.01	11	2.70	0.35	43.7	829.0	364.8	6064
K01148.01	1	1.87	0.58	17.6	1380.8	607.6	6419
K01148.02	1	1.59	0.14	29.9	1060.5	466.7	6419
K01151.01	6	1.46	0.47	20.2	1158.4	509.8	5759
K01151.02	9	1.15	0.46	16.0	1302.4	573.1	5759
K01151.03	12	0.70	0.26	12.9	1451.0	638.5	5759
K01151.04	4	1.10	0.13	28.4	...	...	... <sup>e</sup>
K01161.02	3	2.00	0.92	22.8	1001.1	440.5	5289
K01165.02	8	1.05	0.77	9.4	1714.5	754.5	5810
K01198.01	13	2.84	0.83	25.1	1171.6	515.6	6495
K01198.02	25	1.89	0.67	18.5	1364.8	600.6	6495

Table 2.3 (cont'd)

KOI	# eclipses	$R_p^a$ ( $R_\oplus$ )	$(R_p/a)^{2a}$ (ppm)	$a/R_*$ <sup>a</sup>	Max $T_{eq}^b$ (K)	Min $T_{eq}^c$ (K)	$T_{eff}$ (K)
K01198.03	6	2.80	0.28	42.5	900.7	396.4	6495
K01203.01	11	2.90	0.38	45.3	813.3	357.9	6057
K01203.02	20	2.40	0.78	26.3	1068.0	470.0	6057
K01215.01	17	2.92	0.80	18.1	1262.2	555.4	5946
K01215.02	9	3.36	0.45	27.9	1017.2	447.6	5946
K01216.01	2	1.79	0.59	18.4	1290.1	567.7	6117
K01218.01	1	2.27	0.27	37.9	861.6	379.2	5870
K01236.01	1	4.30	0.62	39.3	977.2	430.0	6779
K01236.02	21	2.60	0.94	19.3	1394.0	613.5	6779
K01258.01	1	4.90	0.98	54.0	697.6	307.0	5675
K01258.02	6	2.20	0.66	29.4	945.0	415.8	5675
K01261.02	2	2.02	0.51	28.0	1020.8	449.2	5976
K01279.01	5	1.56	0.33	28.1	994.5	437.6	5835
K01279.02	10	0.88	0.18	21.5	1136.9	500.3	5835
K01282.01	8	3.00	0.41	22.4	1121.1	493.4	5873
K01283.01	4	1.46	0.64	10.2	1607.0	707.2	5671
K01306.03	54	1.46	0.92	15.0	1391.1	612.1	5969
K01308.01	1	2.16	0.32	37.5	879.2	386.9	5956
K01315.01	5	1.47	0.72	13.9	1461.2	643.0	6029
K01316.01	4	1.47	0.58	9.6	1669.7	734.8	5721
K01316.02	3	1.47	0.31	13.2	1422.3	625.9	5721
K01344.01	9	1.10	0.75	12.2	1560.3	686.6	6038
K01358.02	5	1.58	0.80	24.1	847.3	372.8	4601
K01378.01	1	1.20	0.15	33.0	823.6	362.4	5234
K01379.01	6	1.15	0.62	15.0	1370.3	603.0	5870
K01408.01	4	1.25	0.30	38.6	605.6	266.5	4166
K01445.01	39	1.28	0.49	13.8	1506.3	662.9	6182
K01445.02	3	1.12	0.03	52.7	769.4	338.6	6182
K01445.03	7	0.92	0.06	27.2	1072.0	471.8	6182
K01486.02	4	2.80	0.39	44.7	804.8	354.2	5952
K01529.01	15	2.22	0.46	28.4	1070.4	471.0	6314
K01529.02	28	1.23	0.24	21.5	1230.2	541.3	6314
K01530.01	2	1.89	0.52	22.1	1204.6	530.1	6267
K01531.01	6	1.46	0.97	12.8	1533.8	674.9	6069
K01532.01	1	2.15	0.41	23.8	1193.6	525.2	6450
K01534.01	1	1.64	0.21	29.6	1063.6	468.0	6401
K01534.02	4	0.95	0.26	15.4	1475.6	649.4	6401
K01537.01	28	0.82	0.14	18.1	1287.1	566.4	6063
K01567.03	4	2.31	0.59	31.3	812.1	357.4	5027
K01573.02 <sup>d</sup>	75	1.62	0.87	16.2	1369.0	602.5	6106
K01589.02	31	2.40	0.90	22.6	1144.1	503.5	6013
K01589.03	10	2.40	0.33	37.4	888.7	391.1	6013
K01590.01	8	1.63	0.52	29.1	826.2	363.6	4931
K01590.03	8	1.14	0.94	15.1	1144.8	503.8	4931

Table 2.3 (cont'd)

KOI	# eclipses	$R_p^a$ ( $R_\oplus$ )	$(R_p/a)^{2a}$ (ppm)	$a/R_*$ <sup>a</sup>	Max $T_{eq}^b$ (K)	Min $T_{eq}^c$ (K)	$T_{eff}$ (K)
K01599.01	10	1.90	0.32	33.4	900.1	396.1	5760
K01601.01	6	1.59	0.54	23.3	1072.3	471.9	5726
K01608.01	4	1.85	0.78	17.1	1373.7	604.5	6285
K01608.02	2	1.61	0.21	28.4	1065.2	468.8	6285
K01612.01 <sup>d</sup>	67	0.78	0.85	5.9	2240.0	985.7	6027
K01613.01	21	1.07	0.14	25.6	1061.3	467.0	5945
K01616.01	1	1.38	0.24	22.9	1140.4	501.8	6037
K01618.01 <sup>d</sup>	145	0.77	0.79	6.2	2231.5	982.0	6134
K01621.01	12	2.48	0.46	18.9	1243.6	547.3	5990
K01665.01	10	1.15	0.45	16.2	1374.3	604.7	6119
K01665.02	12	0.96	0.40	14.4	1456.4	640.9	6119
K01677.02	9	0.81	0.19	20.2	1149.5	505.9	5724
K01692.02	42	0.84	0.99	8.1	1742.0	766.6	5501
K01725.01	7	1.15	0.82	43.0	446.4	196.4	3240
K01760.02	6	1.70	0.86	19.5	1099.0	483.6	5372
K01831.02	14	1.04	0.78	14.3	1269.2	558.5	5319
K01843.02	13	0.80	0.40	23.5	712.4	313.5	3823
K01860.02	26	2.50	0.99	20.5	1137.8	500.7	5708
K01867.03	48	1.07	0.90	19.7	822.0	361.7	4042
K01895.02	1	2.31	0.74	42.4	624.3	274.7	4496
K01908.01	2	1.44	0.47	33.5	678.4	298.5	4347
K01908.02	2	1.16	0.13	52.0	544.8	239.7	4347
K01909.01	29	1.48	0.33	23.4	1137.4	500.5	6095
K01909.02	62	1.11	0.58	13.3	1508.1	663.7	6095
K01916.01	2	2.16	0.38	33.6	945.2	415.9	6064
K01916.02	4	1.89	0.80	20.2	1220.2	537.0	6064
K01929.01	34	2.00	0.90	13.3	1464.1	644.3	5900
K01930.01	24	2.21	0.66	16.5	1310.9	576.8	5897
K01930.02	10	2.14	0.29	24.2	1082.8	476.5	5897
K01930.03	5	2.46	0.17	36.2	885.9	389.8	5897
K01930.04	32	1.36	0.41	12.8	1488.2	654.9	5897
K01931.02	36	1.37	0.40	23.8	1043.5	459.2	5639
K01931.03	48	1.23	0.56	18.1	1196.3	526.5	5639
K01952.02	11	2.06	0.24	38.3	875.7	385.3	6000
K01952.03	57	1.25	0.81	12.6	1529.5	673.1	6000
K01955.01	8	2.06	0.48	24.4	1182.7	520.5	6464
K01955.02	3	2.08	0.14	46.3	858.5	377.8	6464
K01964.01 <sup>d</sup>	164	0.73	0.89	7.3	1854.2	815.9	5548
K01977.02	30	0.69	0.22	23.4	822.7	362.0	4401
K02007.02	12	1.52	0.18	30.9	985.2	433.5	6064
K02025.01	23	3.10	0.90	22.5	1188.1	522.8	6234
K02025.02	8	2.80	0.44	29.1	1044.0	459.4	6234
K02025.03	37	1.64	0.47	16.5	1386.9	610.3	6234
K02036.02	4	0.98	0.64	21.2	803.0	353.4	4090

Table 2.3 (cont'd)

KOI	# eclipses	$R_p^a$ ( $R_\oplus$ )	$(R_p/a)^{2a}$ (ppm)	$a/R_*$ <sup>a</sup>	Max $T_{eq}^b$ (K)	Min $T_{eq}^c$ (K)	$T_{eff}$ (K)
K02038.02	16	2.20	0.83	26.4	996.9	438.7	5666
K02038.03	5	1.56	0.26	33.5	884.0	389.0	5666
K02038.04	5	1.61	0.17	42.3	787.7	346.6	5666
K02051.01	9	2.82	0.47	36.8	883.7	388.9	5929
K02051.02	19	1.59	0.46	20.9	1172.4	515.9	5929
K02110.01 <sup>d</sup>	84	1.14	0.63	10.3	1818.9	800.4	6470
K02113.01	10	2.80	0.96	31.6	832.0	366.1	5177
K02113.02	9	2.38	0.97	26.7	905.4	398.4	5177
K02149.01	14	1.53	0.32	17.3	1371.8	603.7	6314
K02160.01	14	1.78	0.33	32.6	919.0	404.4	5810
K02160.02	15	1.41	0.25	29.7	963.8	424.1	5810
K02163.01	7	1.95	0.76	20.2	1201.3	528.7	5980
K02169.01	51	0.97	0.53	13.2	1355.6	596.5	5447
K02169.02	86	0.75	0.64	9.3	1618.2	712.1	5447
K02169.03	51	0.71	0.40	11.1	1477.2	650.1	5447
K02169.04	113	0.48	0.43	7.2	1838.2	808.9	5447
K02174.01	3	1.35	0.95	22.2	835.6	367.7	4356
K02174.03	6	0.95	0.39	24.4	796.1	350.3	4356
K02195.01	4	2.50	0.48	25.4	1165.3	512.8	6502
K02195.02	1	2.10	0.20	33.2	...	...	... <sup>e</sup>
K02218.02	20	1.43	0.23	31.4	935.8	411.8	5803
K02220.04	9	1.10	0.37	17.1	...	...	... <sup>e</sup>
K02220.05	6	1.20	0.24	23.0	...	...	... <sup>e</sup>
K02248.02	5	1.56	0.64	23.8	980.5	431.5	5294
K02261.01	17	1.05	0.99	12.3	1337.0	588.3	5179
K02261.02	9	0.82	0.31	17.2	1129.9	497.2	5179
K02295.01	2	0.67	0.06	28.2	927.9	408.3	5453
K02311.02	5	0.77	0.08	24.9	1044.1	459.4	5765
K02352.01	19	1.15	0.16	19.6	1355.9	596.7	6638
K02352.02	46	0.82	0.26	11.0	1810.4	796.7	6638
K02352.03	33	1.09	0.27	14.2	1594.0	701.5	6638
K02390.01	6	1.66	0.31	22.4	1155.5	508.5	6052
K02414.01	17	1.18	0.10	36.5	881.1	387.7	5889
K02433.01	16	2.07	0.51	25.6	1085.6	477.7	6084
K02442.01	1	1.89	0.27	43.3	711.9	313.3	5184
K02442.02	1	1.40	0.39	27.0	...	...	... <sup>e</sup>
K02443.01	7	1.20	0.49	14.4	1503.2	661.5	6314
K02443.02	7	1.02	0.17	20.9	1247.5	549.0	6314
K02457.01 <sup>d</sup>	70	1.14	0.87	7.0	2293.9	1009.4	6733
K02462.01	30	1.43	0.33	15.9	1369.1	602.5	6050
K02545.01	25	0.78	0.20	12.9	1589.9	699.7	6321
K02595.01	33	1.82	0.67	12.0	1757.2	773.3	6742
K02595.02	20	2.07	0.46	16.4	1502.1	661.0	6742
K02597.01	42	1.63	0.70	16.2	1433.7	630.9	6392

### 2.5.3 Individual Candidates

I consider Kepler-10b on its own, shown in Figure 2.4, using 898 eclipses from Q2 to Q15, excluding Q8 and Q12. Data do not exist for these two quarters for this planet because of hardware failure (Fogtmann-Schulz et al., 2014). The bin size is approximately 0.008 in phase. I perform a similar MCMC procedure as for the close-in group, but now I include a third term, the semi-amplitude of a sinusoidal phase curve which peaks at phase 0.5. This sine curve reproduces the phase curve seen in previous studies of Kepler-10b, and its inclusion is supported by the BIC. I find a semi-amplitude of  $2.96 \pm 1.36$  ppm for the phase curve, since I am only fitting from phase 0.25 to phase 0.75, and an eclipse depth of  $7.08 \pm 1.06$  ppm, giving a geometric albedo of  $0.60 \pm 0.09$  if due solely to reflected light. If the semi-amplitude from phase 0.25 to phase 0.75 represents half of the peak-to-peak amplitude of the phase curve, then my eclipse depth and amplitude values are consistent with those found by Batalha et al. (2011); Demory (2014); Fogtmann-Schulz et al. (2014); Rouan et al. (2011), shown in Table 2.4. Figure 2.4 also shows the distributions for the three parameters in the MCMC chain, as well as the calculated reflected light plus thermal emission eclipse depths for several geometric albedo values.

I find that KOI 102.01 also has a significant, physically plausible detection at  $7.40_{-2.45}^{+2.42}$  ppm, shown in Figure 2.5. I keep this candidate in the average for Figure 2.2 because at a magnitude in the *Kepler* bandpass of 12.57, it does not dominate the weighted average. For the individual analysis of this candidate, I include data that is  $\pm 5$  times the duration of the full eclipse, centered on phase 0.5 to improve

Table 2.3 (cont'd)

KOI	# eclipses	$R_p^a$ ( $R_\oplus$ )	$(R_p/a)^{2a}$ (ppm)	$a/R_*$ <sup>a</sup>	Max $T_{eq}$ <sup>b</sup> (K)	Min $T_{eq}$ <sup>c</sup> (K)	$T_{eff}$ (K)
K02597.02	32	1.70	0.44	21.3	1251.1	550.5	6392
K02597.03	57	1.37	0.81	12.7	1620.1	712.9	6392
K02632.01	13	1.14	0.39	11.5	1722.2	757.9	6461
K02639.01	5	3.10	0.60	32.6	965.0	424.6	6102
K02650.02	7	1.13	0.67	24.3	742.9	326.9	4050
K02674.02	7	1.37	0.35	17.0	1309.0	576.1	5973
K02720.01	1	0.80	0.24	14.3	1457.7	641.5	6109
K02722.01	11	1.43	0.76	12.2	1687.5	742.6	6534
K02722.02	6	1.41	0.33	18.4	1377.8	606.3	6534
K02722.03	18	1.14	0.84	9.3	1939.4	853.4	6534
K02722.04	5	1.30	0.38	15.7	1488.2	654.9	6534
K02768.01	4	1.30	0.31	26.0	995.1	437.9	5612
K02801.01	29	1.56	0.74	8.0	1947.0	856.8	6095
K02956.01	39	0.77	0.37	7.5	2217.2	975.7	6717
K03097.01	17	1.82	0.51	13.1	1574.5	692.8	6306
K03097.02	25	1.25	0.50	9.0	1898.1	835.3	6306
K03097.03	24	1.09	0.28	10.6	1752.3	771.1	6306
K03158.01	10	0.50	0.21	9.9	...	...	... <sup>e</sup>
K03158.04	5	0.83	0.21	16.5	...	...	... <sup>e</sup>
K03158.05	3	0.84	0.16	19.2	...	...	... <sup>e</sup>
K03196.01	21	0.65	0.21	9.3	...	...	... <sup>e</sup>
K03196.02	14	0.97	0.30	11.5	...	...	... <sup>e</sup>
K03225.01	14	0.96	0.56	7.7	...	...	... <sup>e</sup>
K04146.01	17	0.83	0.75	11.8	...	...	... <sup>e</sup>

<sup>a</sup> $R_p$ ,  $a$ , and  $R_*$  are taken from the Exoplanet Archive candidate table, and  $(R_p/a)^2$  and  $a/R_*$  are calculated from them.

<sup>b</sup>Assumes  $f = 2/3$  (instant re-radiation) and  $A_B = 0.0$ .

<sup>c</sup>Assumes  $f = 1/4$  (complete redistribution) and  $A_B = 0.9$  (i.e.  $A_g = 0.6$ ).

<sup>d</sup>Included in smaller control group of 31 candidates.

<sup>e</sup>Stellar effective temperature not given in the Exoplanet Archive candidate table.

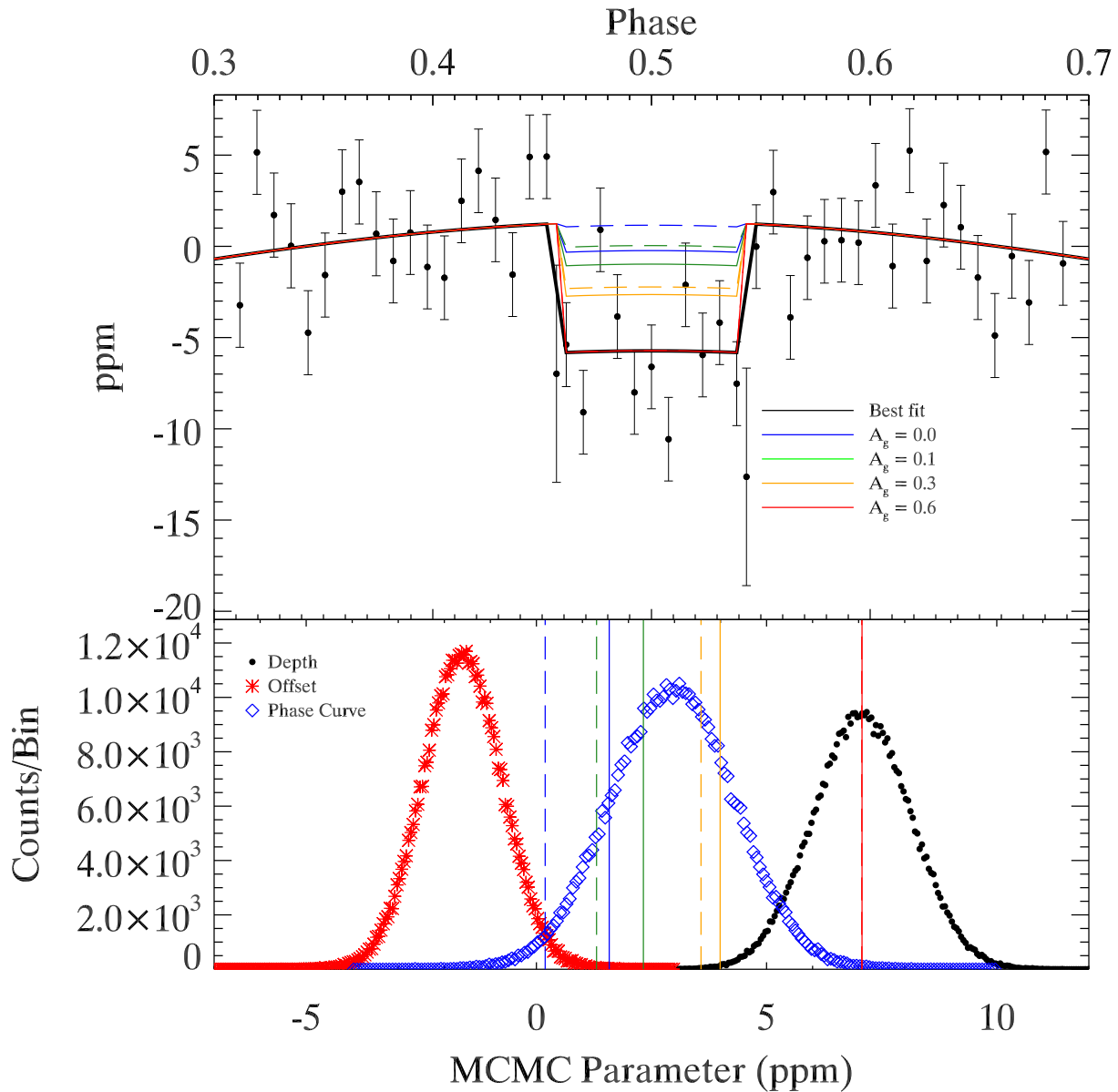


Figure 2.4 Upper panel: The light curve, centered on secondary eclipse, for Kepler-10b. The binned data are shown as points. The error bars are the propagated photometric errors. The best fit curve is the solid black line. Overplotted are the reflected light plus thermal emission models for  $A_g = (2/3) * A_B = 0.0$  (blue), 0.1 (green), 0.3 (orange), and 0.6 (red), with the re-radiation factor  $f = 1/4$  (dashed) and  $2/3$  (solid). Note that the best fit curve is very similar to the red  $A_g = 0.6$  line and that the ingress and egress bins have large error bars due to the small size of those two bins (cf. Section 2.3). Lower panel: The distributions for the three parameters of the MCMC run, with the depths from the reflected light plus thermal emission from the upper panel plotted as vertical lines. The three fitted parameters are eclipse depth ( $7.08 \pm 1.06$  ppm), continuum offset from zero ( $-1.61 \pm 0.86$  ppm), and semi-amplitude of the phase curve ( $2.96 \pm 1.36$  ppm).

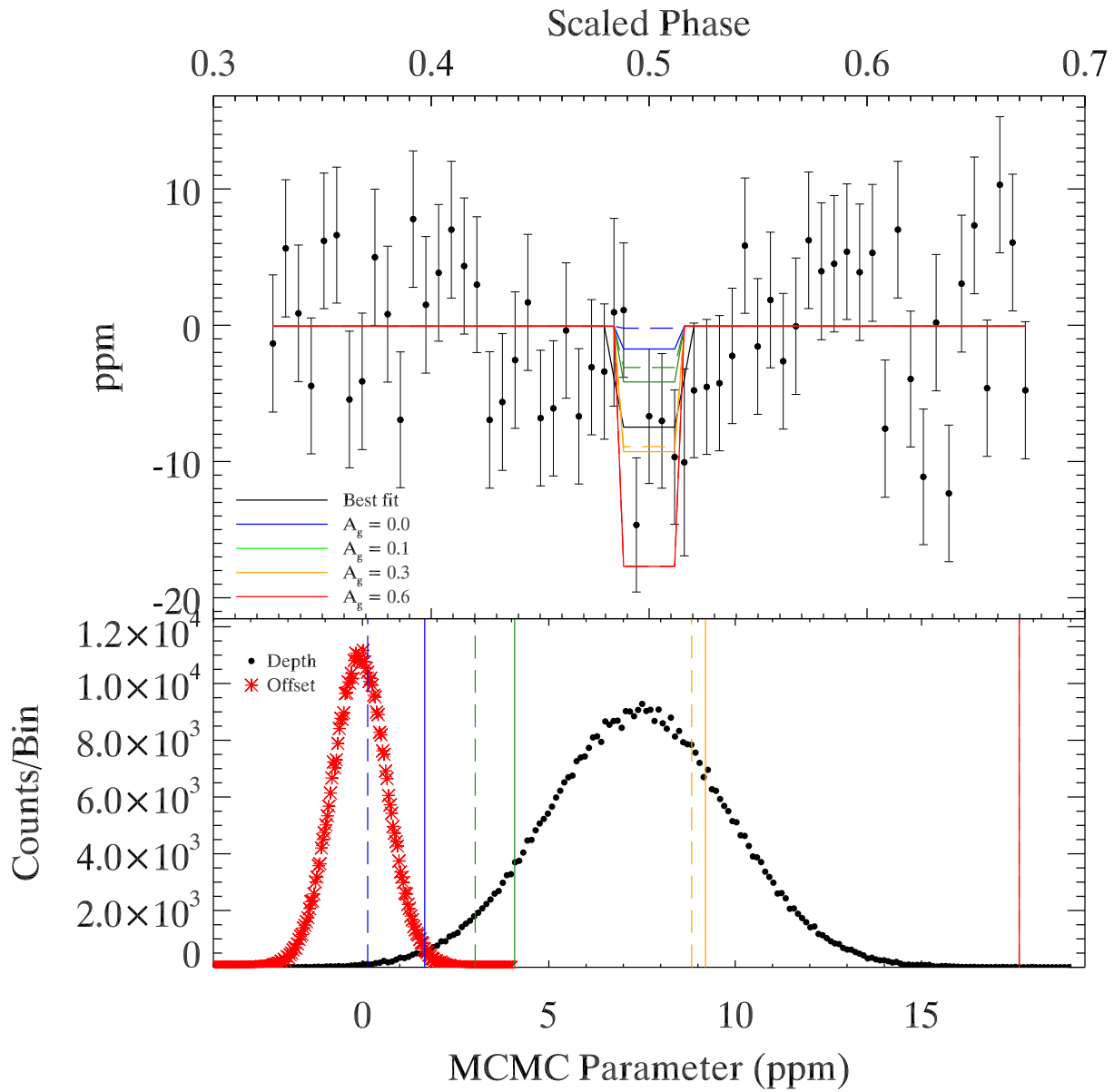


Figure 2.5 Upper panel: The light curve, centered on secondary eclipse, for KOI 102.01. The binned data are shown as points. The error bars are the propagated photometric errors. The best fit curve is the solid black line. Overplotted are the reflected light plus thermal emission models for  $A_g = (2/3) * A_B = 0.0$  (blue), 0.1 (green), 0.3 (orange), and 0.6 (red), with the re-radiation factor  $f = 1/4$  (dashed) and  $2/3$  (solid). Lower panel: The distributions for the two parameters of the MCMC run, with the depths from the reflected light plus thermal emission from the upper panel plotted as vertical lines. The two fitted parameters are eclipse depth ( $7.40^{+2.42}_{-2.45}$  ppm) and continuum offset from zero ( $-0.08 \pm 0.73$  ppm).

Table 2.4. Kepler-10b Studies

Authors	Phase Curve Amplitude (ppm)	Eclipse Depth (ppm)
Batalha et al. (2011)	$7.6 \pm 2.0$	$5.8 \pm 2.5$
Rouan et al. (2011)	$5.6 \pm 2.0$	$5.6 \pm 2.0$
Fogtman-Schulz et al. (2014)	$8.13 \pm 0.68$	$9.91 \pm 1.01$
Demory (2014)	...	$7.4^{+1.1}_{-1.0}$
This Work	$5.92 \pm 2.72$	$7.08 \pm 1.06$

the baseline. I also change the bin size to approximately 0.0058 in phase, such that there are 5 bins within full eclipse. The candidate has  $(R_p/a)^2 = 29.36$  ppm, resulting in a geometric albedo of  $0.25 \pm 0.08$  if due only to reflected light. With  $R_p = 3.69 R_\oplus$ , this albedo puts the candidate in a class of reflective hot Neptunes.

KOI 676.02 may have an eccentric orbit. [Ioannidis et al. \(2014\)](#) suggest the most probable configuration for the KOI 676 (Kepler-210) system is that the inner planets, KOI 676.01 and KOI 676.02, have a large eccentricity, based on the mismatch of  $a/R_*$  between the two. A third member of the system is hypothesized from transit timing variations (TTVs). The suggested configuration has the major axis of the orbit of KOI 676.02 along the line-of-sight to Earth. I include KOI 676.02 in my close-in group at the moment but will remove it if the eccentricity is confirmed. Note that KOI 676 has  $T_{eff} < 4500$  K, so this candidate was not included in the averages above for stars with  $T_{eff} > 5000$  K and  $T_{eff} > 4500$  K.

I exclude KOI 116 (Kepler-106) from my control group. The original control group contained KOI 116.01 (Kepler-106c), KOI 116.03 (Kepler-106b), and KOI 116.04 (Kepler-106d). KOI 116.03 is the innermost of 4 known planets in this system,

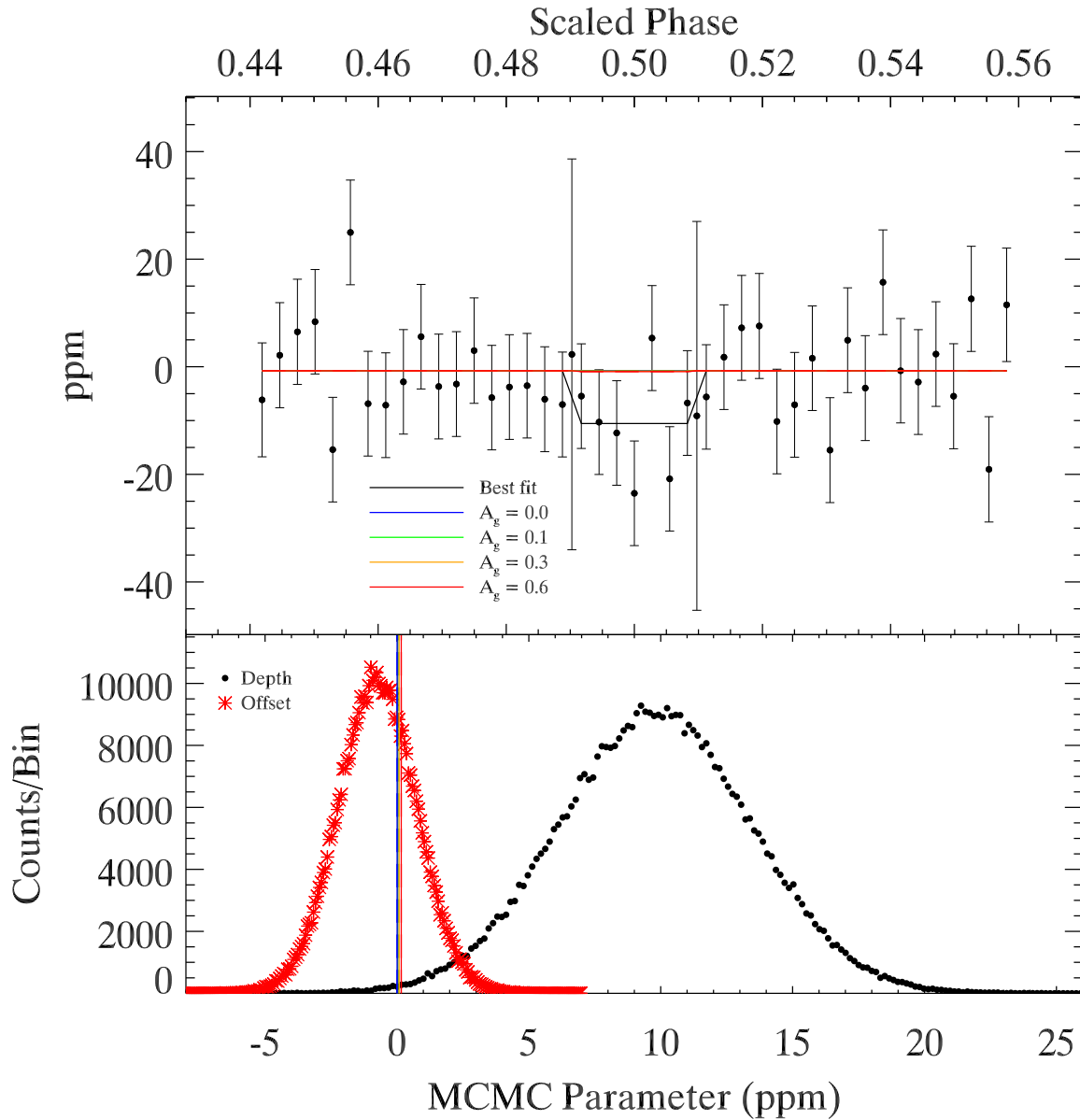


Figure 2.6 Upper panel: The light curve, centered on secondary eclipse, for KOI 116.03. The binned data are shown as points. The error bars are the propagated photometric errors. The best fit curve is the solid black line. Overplotted are the reflected light plus thermal emission models for  $A_g = (2/3) * A_B = 0.0$  (blue), 0.1 (green), 0.3 (orange), and 0.6 (red), with the re-radiation factor  $f = 1/4$  (dashed) and  $2/3$  (solid). Note that the ingress and egress bins have large error bars due to the small size of those two bins (cf. Section 2.3). Lower panel: The distributions for the two parameters of the MCMC run, with the depths from the reflected light plus thermal emission from the upper panel plotted as vertical lines. The two fitted parameters are eclipse depth ( $9.80^{+3.64}_{-3.65}$  ppm) and continuum offset from zero ( $-0.75 \pm 1.48$  ppm).

with periods of 6.2 days, 13.6 days, 24.0 days, and 43.8 days. When considering the shortened control group, I found that KOI 116.03 has a  $2\sigma$  detection of an eclipse on its own,  $9.80_{-3.65}^{+3.64}$  ppm, which is far deeper than expected even for a high geometric albedo. I use a bin size of approximately 0.0028 in phase, which corresponds to 7 bins inside of full eclipse. The candidate has  $(R_p/a)^2 = 0.273$  ppm. The candidate has a maximum equilibrium temperature of 1434 K, assuming  $A_B = 0$  and instantaneous re-radiation, so thermal emission due to stellar irradiation cannot explain the large eclipse depth either. Given the value of  $(R_p/a)^2$ , the nominal eclipse is much greater in amplitude than would be possible for a normal planet, and I conservatively exclude this system from my average. In principle, the presence of multiple planets of this type in my sample could bias my average result. This, however, is a very obvious and easily detected case, and there is no evidence for other comparable systems in my sample. Although the evidence for the planetary nature of KOI 116.03 seems solid (Marcy et al., 2014), my stacked eclipse data suggest that there may be other effects at play in this system. Possibilities include the presence of a highly back-scattering dust cloud surrounding the planet, or the transit of a Mercury-sized planet in an orbit with half the period of KOI 116.03. Exploration of these possibilities is beyond the scope of this work. I show my stacked eclipses for KOI 116.03 in Figure 2.6.

#### 2.5.4 Advantages and Limitations of the Technique

My average is biased towards brighter, and hence closer, stars, due to the weighting by photometric noise. There is no reason to expect a correlation between

the stellar distance from Earth and planet type or albedo, so I do not expect this bias to favor bright or dark planets. The case of Kepler-10b shows that I must be careful in my sample selection, however, when the sample size is small, because an atypically bright planet around an atypically bright star in the sample can alter the results. Likewise, false positives could have a bigger influence when the sample size is small, so it is important to screen the individual candidates for any obvious signs that they could be strongly influencing the result. To limit the risk of including false positives, I only considered objects deemed to be “planet candidates”, which means that the candidate has not failed any of the false positive tests in [Batalha et al. \(2013\)](#) applied thus far. I also examined the stacked eclipses of each candidate individually, to discriminate against non-physically large effects such as I find for KOI 116.03, but found no further irregularities.

The major disadvantage of my technique is that I cannot tell whether the average represents a typical object in the group. The underlying distribution could be bimodal, with the average representing a non-existent object in between the two groups.

There are a number of astrophysical dilution effects that must be considered when interpreting my result. I mention these effects here, but I defer my quantitative consideration of them to Chapter 3, where the much larger sample available in long cadence gives me a better statistical basis for rejecting them. If any of the planet candidates are in eccentric orbits, their eclipses would not occur at the expected phase and would destructively add to the signal. False positives could also dilute the signal, because there may be no eclipse to detect. For example, eclipsing binaries

in which the two stars are of similar type could have primary and secondary eclipses that are approximately equal. If the binary is blended with the KOI star, both the primary and the secondary eclipses would look like planetary transits at half the period of the binary, and, if included in the average, the object would add in a flat signal when looking at phase 0.5 based on the planetary interpretation (e.g. [Borucki et al., 2011](#)). Cases in which we see a planetary transit but do not see the eclipse due to the geometry of system would result in extra light at the expected eclipse, creating a bump in the light curve that would decrease my average signal. This scenario would only occur if the orbits are not circular, and I expect that the orbits of the close-in candidates have circularized. Uncertainties in the host star parameters could also be detrimental, as the planet radius is tied directly to the stellar radius when measured using the transiting technique. Changing the size of a planet would affect my calculated albedo, since the calculation depends on the planet radius.

In spite of its limitations, an overwhelming advantage of my technique is that I reach a much greater signal-to-noise ratio in the eclipse light curve than is achievable for many of these planet candidates individually. Moreover, I can use a large sample of planet candidates to obtain information about the average albedo without being biased towards the candidates that are most easily measured, which tend to be more reflective than average. Future space missions such as TESS ([Ricker et al., 2015](#)) and PLATO ([Rauer et al., 2014](#)) will discover even greater numbers of transiting planets, many of which will be too faint to allow individual characterization of their atmospheres. Grouping planets to determine their average atmospheric properties

will become an increasingly relevant and important tool in the future.

## 2.6 Implications for Atmospheres and Surfaces of Sub-Saturns

### 2.6.1 Presence of Atmospheres in My Sample

[Heng & Kopparla \(2012\)](#) model the stability of atmospheres on tidally-locked Earth-like planets, where the body is mostly rocky with a thin atmosphere of varying mean molecular weights ( $\mu$ ). They consider the stability against condensation on the night-side of the planet, for planets around G, K, and M dwarfs. They place *Kepler* candidates up to  $6 R_{\oplus}$  on these stability diagrams in their Figures 3 and 6. Two of my close-in candidates have F dwarf hosts, but I can locate the remaining 30 candidates around G, K, and M dwarfs on their stability diagrams. All but one candidate lie in the stable region if the atmospheres have low  $\mu$ , but none are stable with an Earth-like atmospheric composition. The single candidate outside the stable region even at low  $\mu$  is KOI 356.01, though it is very close to the boundary.

Many of my close-in candidates, however, are likely to be more Neptune-like than Earth-like. [Lopez & Fortney \(2014\)](#) suggest a cut-off radius for rocky planets of  $1.75 R_{\oplus}$ , based on the radius-composition relation they find in their planet formation models. [Rogers \(2015\)](#) sets the bar even lower, determining a cut-off of  $1.6 R_{\oplus}$  through a hierarchical Bayesian analysis of *Kepler* planets with mass limits determined from radial velocity studies. Of my 32 close-in candidates, 12 would be considered rocky based on these cut-off values. KOI 356.01 would be more Saturn-like, at a radius of  $5.73 R_{\oplus}$ . There remains a small probability that

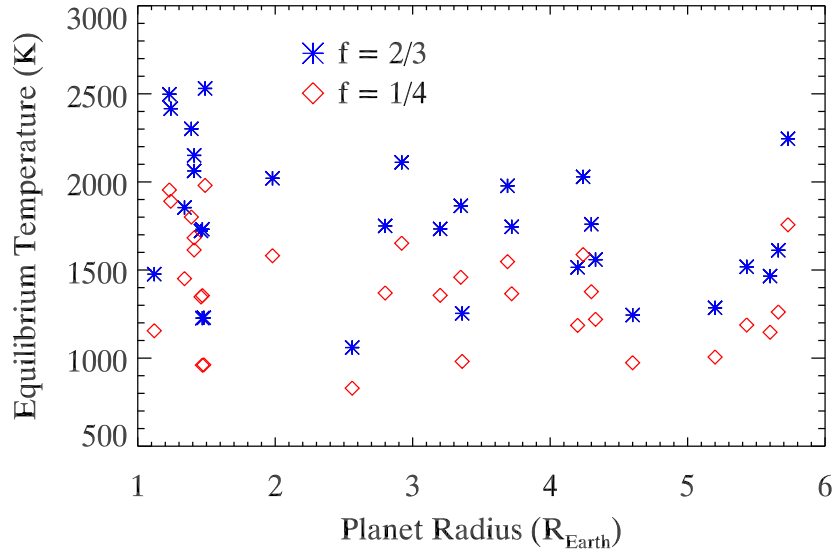


Figure 2.7 The calculated equilibrium temperatures of the close-in group, excluding Kepler-10b, plotted versus planet radius. The equilibrium temperatures are calculated assuming our average geometric albedo and Lambert’s law. The blue symbols use  $f = 2/3$ , for instantaneous re-radiation, while the red symbols use  $f = 1/4$ , for complete redistribution of heat.

the planet candidates above  $1.6 R_{\oplus}$  could be rocky. Kepler-10c, despite being  $2.35 R_{\oplus}$ , has a density of  $7.1 \text{ g cm}^{-3}$  (Dumusque et al., 2014), suggesting a rocky nature with a significant amount (5 to 20 wt.%) of water or some other high  $\mu$  volatile. The candidates smaller than  $1.5 R_{\oplus}$  are quite likely to be rocky, while the candidates above  $2.5 R_{\oplus}$  are likely Neptune-like with substantial atmospheres, and KOI 299.01, at  $1.98 R_{\oplus}$ , may fall somewhere in between the two types, like Kepler-10c.

## 2.6.2 Expected Albedos

The candidates in my close-in group in Section 2.5.1 are too hot to have water clouds in their upper atmospheres (Morley et al., 2014). Figure 2.7 shows the equilibrium temperature, calculated using my average geometric albedo, versus planet radius for all of the objects in the close-in group, excluding Kepler-10b. If the candidates all have poor heat redistribution (i.e.  $f = 2/3$ ), they are all above 1000 K. Thus the albedo I determine cannot be due to water clouds.

For giant planets, Sudarsky et al. (2000) show that alkali metals like Na strongly absorb visible light in atmospheres that are too hot for water clouds but cool enough that a silicate layer does not form. Above 900 K, a silicate layer forms, but it forms at low enough altitudes that the alkali metals above the layer still absorb a significant amount of the incident visible light, producing the lowest albedos. As the temperature increases, the silicate layer forms higher up in the atmosphere, potentially reflecting the incident light before it can interact with the alkali metals, producing much higher albedos. The Bond albedo due to silicates could be as high as 0.55, which translates to a geometric albedo of 0.37 for Lambertian surfaces. Demory et al. (2011) find  $A_g = 0.32 \pm 0.03$  for Kepler-7b, which agrees with the predictions of Sudarsky et al. (2000) for reflective cloud layers, but they find that the high albedo can also be explained solely with Rayleigh scattering if the planet's atmosphere is depleted in alkali metals relative to solar abundances by a factor of 10-100. Other hot Jupiters with similar equilibrium temperatures, such as HD 209458b, have been found to be very dark, with upper limits on the geometric

albedo of 0.12 (Rowe et al., 2008), suggesting that if reflective clouds produce the high albedo of Kepler-7b, then there must be some mechanism that suppresses the cloud formation in HD 209458b and other dark hot Jupiters.

Miguel et al. (2011) model rocky planets at these temperatures with tenuous atmospheres due to vaporization of the surface. For atmospheres up to nearly 2900 K, monatomic Na dominates the atmosphere, with the fraction of SiO increasing with temperature, and, by 2900 K, the atmosphere becomes dominated by SiO and monatomic Na. If the smaller planets can also form a silicate layer high in their atmospheres, that could boost their albedos. Alternatively, if their atmospheres are tenuous enough, the light may be reflecting off the surfaces such as in the “lava ocean” model proposed for Kepler-10b and Kepler-78b (Léger et al., 2011; Rouan et al., 2011; Sanchis-Ojeda et al., 2013).

My average albedo for the close-in sub-Saturns suggests that the high albedos of Kepler-10b and Kepler-78b are atypical and that sub-Saturns are typically more reflective than hot Jupiters. Limiting my close-in group to planets  $< 2R_{\oplus}$ , excluding Kepler-10b, results in a non-detection of an eclipse with a depth of  $2.14 \pm 1.96$  ppm, using an MCMC trial similar to those described above. This result gives less than a 1% chance of an average geometric albedo  $\geq 0.6$  and a 21% chance of an average geometric albedo  $\geq 0.3$ . Moreover, thermal emission alone cannot explain the eclipse depth of Kepler-10b, unless the planet has some source of internal heat or a spectrum that is not a blackbody curve (Fogtman-Schulz et al., 2014). If the “lava ocean” model proposed for Kepler-10b and Kepler-78b is indeed the source of the high albedo needed to match the eclipse depths for these two planets, then

close-in super-Earths more typically have darker surfaces, or absorption due to alkali metals or hazes in their tenuous atmospheres. They could also have mildly reflective clouds that shield the more reflective lava ocean surface.

Limiting my close-in group to the planets  $> 2R_{\oplus}$  results in an average eclipse depth of  $4.68 \pm 1.22$  ppm, giving a geometric albedo of  $0.23 \pm 0.06$ . The Neptune-like sub-Saturns likely also have clouds or hazes that reflect the incident light back before being substantially absorbed by the alkali metals in their atmospheres. Alternatively, the average eclipse depth I find could be due to thermal inversions in the Neptune-like atmospheres, as have been seen in and modeled for some hot Jupiters (e.g. [Fortney et al., 2008](#); [Zahnle et al., 2009](#)). [Spiegel et al. \(2010\)](#) note that Neptune and Uranus have much higher metallicities than Jupiter, and so Neptune-like planets could have extra absorbers due to the increased metals that could aid the creation of thermal inversions. If a thermal inversion exists, the thermal emission contribution to the eclipse depths could be greater, reducing the albedo necessary to match the depths.

## 2.7 Chapter 2 Summary

I average eclipses of 31 close-in planet candidates  $< 6R_{\oplus}$  to determine the average albedo of the group. I find that, on average, close-in sub-Saturns are not extremely dark, with an average geometric albedo of 0.22. This albedo is consistent with the results for close-in super-Earths by [Demory \(2014\)](#), and it is in contrast to many hot Jupiters, which have albedos  $< 0.1$ , and to Kepler-10b and Kepler-78b,

which have albedos of 0.4-0.6. The super-Earths may have darker surfaces than Kepler-10b and Kepler-78b, or they may have clouds or hazes in their tenuous alkali metal atmospheres that either absorb some of the light or reflect the light before it can reach the higher albedo surface. The Neptune-like planets may also have reflective clouds or hazes, preventing absorption lower in their atmospheres by the alkali metals that produce the very low albedos in hot Jupiters. The Neptune-like planets may also have thermal inversions that add extra thermal emission to the eclipse depths, making the albedo appear higher than it is.

## Chapter 3: Statistical Eclipses of Long Cadence Close-in *Kepler* Sub-Saturns

### 3.1 Introduction

Secondary eclipses of a transiting planet occur when the planet passes behind the star, resulting in a slight decrease in the total light from the system. Secondary eclipses are often measured in the infrared, where the planet-to-star contrast is optimal due to infrared emission from the planet (e.g. [Charbonneau et al., 2005](#); [Deming et al., 2005](#)). In the *Kepler* bandpass, however, reflected light dominates. The reflected light signal is proportional to the square of the ratio of the planet radius to its semi-major axis ( $(R_p/a)^2$ ), which is, at best, tens of parts per million (ppm), but more typically a few ppm or smaller. This is difficult to detect for most individual candidates, even in the *Kepler* data (e.g. [Angerhausen et al., 2015](#); [Batalha et al., 2011](#); [Coughlin & López-Morales, 2012](#); [Demory, 2014](#); [Esteves et al., 2013, 2015](#)). Detecting reflected light provides insight into the atmosphere and/or surface by constraining the albedo. In [Sheets & Deming \(2014\)](#), henceforth Chapter 2, I demonstrated that short cadence *Kepler* light curves of many individual candidates can be co-added constructively to detect an average secondary eclipse for the

group of planets.

In this chapter, I adapt the statistical method of Chapter 2 to the *Kepler* long cadence data. The two main challenges presented by the long cadence data are the distortion of the eclipse by convolution with the 30-minute integration time for each observed data point, and also the subsequent reduction in the number of data points per eclipse compared to the short cadence data. The long cadence data, however, offer a larger sample of planet candidates, allowing me to group the planets into more restrictive and more physically meaningful radius bins than the broad 1 to 6  $R_{\oplus}$  bin of Chapter 2.

In Section 3.2, I describe the *Kepler* candidate data selection. In Section 3.3, I discuss the modifications to the data processing and averaging method for the long cadence data. In Section 3.4, I describe how I modify the thermal plus reflected light models for the long cadence data. Section 3.5 considers the potential effects of false positives on my results, and Section 3.6 presents the results for super-Earths (1-2  $R_{\oplus}$ ), mini-Neptunes (2-4  $R_{\oplus}$ ), super-Neptunes (4-6  $R_{\oplus}$ ), as well as a discussion which explores the implications of the albedo results. Lastly, Section 3.7 provides a summary of the chapter.

## 3.2 *Kepler* Data and Candidate Selection

The number of planets confirmed by follow-up observation (985) is a small fraction of the total planet candidates identified (4696) by the *Kepler* mission (Coughlin et al., 2016). To provide a larger sample, I therefore select my targets

from the planet candidates. The false positive rate for objects labeled as planet candidates is low, near 10 percent (e.g. Désert et al., 2015; Fressin et al., 2013), so I expect that the benefit of additional targets to increase my signal to noise will outweigh the potential interference of false positives. In Section 3.5, I discuss scenarios in which false positives may influence my results.

I select candidates with radii of 1 to 2  $R_{\oplus}$ , 2 to 4  $R_{\oplus}$ , and 4 to 6  $R_{\oplus}$  from the cumulative table of the NASA Exoplanet Archive’s Kepler Objects of Interest catalog<sup>1</sup>, downloaded on 23 Feb 2015. I further limit the selection to candidates in these radius bins with  $(R_p/a)^2 \geq 10$  parts per million (ppm), where  $R_p$  is the planet radius and  $a$  is the semi-major axis of the orbit. The expected depth of the secondary eclipse, assuming reflected light only, is the geometric albedo times this value, so I am selecting candidates that are most likely to be detectable in aggregate. I exclude candidates with grazing transits (i.e. impact parameter  $b \geq 1 - (R_p/R_*)$ , where  $R_p$  is the planet candidate radius and  $R_*$  is the host star radius). I adopt circular orbits, with the center of the transit at phase 0.0 and the center of the secondary eclipse at phase 0.5. I address the possibility of non-circular orbits in the discussion in Section 3.5.4. The KOI catalog has evolved while this manuscript was in preparation. Using the Feb 2015 download of the KOI cumulative table, my selection criteria combined with the tests performed in Section 3.3.1 result in 56 super-Earth (1-2  $R_{\oplus}$ ) candidates, 38 mini-Neptune (2-4  $R_{\oplus}$ ) candidates, and 16 super-Neptune (4-6  $R_{\oplus}$ ) candidates, whose parameters are given in Table 3.1 and Table 3.2. The various catalogs that feed into the cumulative table were finalized

---

<sup>1</sup><http://exoplanetarchive.ipac.caltech.edu/>

late in 2015, resulting in some of these objects changing status to false positives. Additionally, [Morton et al. \(2016\)](#) provided false positive probabilities for nearly all of the candidates in the cumulative table. To demonstrate the robustness of my results against false positives, I present in Section 3.6 both the results using the Feb 2015 catalog, as well as the results using subsets of the 3 groups, from which I have removed planet candidates with a false positive probability greater than 1% and a few newly-identified false positives. The shortened groups contain 40 super-Earth candidates, 28 mini-Neptune candidates, and 13 super-Neptune candidates. The objects removed are identified in [Table 3.1](#) and [Table 3.2](#) with a footnote. Most of the host stars in my sample are sun-like or nearly so; The distribution of spectral types and stellar effective temperatures is given in [Fig. 3.1](#) for the Feb 2015 version of the groups.

Table 3.1. Candidate Parameters

KOI	# eclipses	<sup>a</sup> $R_p^b$ ( $R_\oplus$ )	$(R_p/a)^{2b}$ (ppm)	$a/R_*$ <sup>b</sup>	Max $T_{eq}^c$ (K)	Min $T_{eq}^d$ (K)	$T_{eff}$ (K)
Kepler-10b							
K00072.01	814 (792)	1.45	13.51	3.4	2748.6	1209.6	5627
super-Earths							
K00191.03 <sup>e</sup>	1315 (0)	1.25	12.60	3.7	2674.6	1177.0	5700
K00739.01	1005 (957)	1.42	10.46	7.9	1201.1	528.6	3733
K00936.02	1296 (1193)	1.22	13.77	6.8	1236.9	544.3	3581
K00952.05 <sup>e</sup>	1024 (0)	1.88	38.52	5.5	1429.6	629.1	3727
K01050.01	866 (788)	1.78	13.41	5.8	1915.8	843.1	5095
K01169.01 <sup>e</sup>	1829 (0)	1.29	12.56	3.6	2691.3	1184.3	5676
K01202.01	1385 (1311)	1.47	13.56	5.1	1962.3	863.5	4894
K01239.01	1210 (1160)	1.74	18.35	3.6	2903.7	1277.8	6108
K01300.01	1828 (1673)	1.10	16.31	4.7	1849.5	813.9	4441
K01367.01	2159 (1985)	1.40	23.12	3.7	2394.6	1053.8	5076
K01424.01	1071 (1026)	1.58	10.88	6.1	1766.0	777.1	4845
K01442.01	1379 (1291)	1.21	11.49	3.1	2904.2	1278.0	5626
K01475.01	717 (671)	1.81	11.95	8.6	1252.3	551.1	4056
K01510.01	1485 (1412)	1.70	20.22	4.7	2052.6	903.3	4924
K01655.01	1108 (1071)	1.48	11.48	4.0	2651.6	1166.8	5902
K01662.01 <sup>e</sup>	1319 (0)	1.66	18.81	4.2	2401.8	1056.9	5463
K01875.02	1691 (1595)	1.31	19.00	3.0	3119.6	1372.8	5953
K01880.01	1041 (940)	1.56	14.41	7.1	1307.1	575.2	3855
K01981.01	900 (876)	1.61	11.99	4.3	2307.6	1015.5	5265
K02119.01	2032 (1904)	1.38	20.76	3.2	2625.0	1155.1	5203
K02223.01	1104 (1070)	1.64	13.80	5.4	1950.4	858.3	5002
K02250.02	1040 (985)	1.71	29.98	3.5	2385.5	1049.8	4922
K02266.01	827 (782)	1.70	17.12	5.1	1984.1	873.1	4949
K02325.01 <sup>e</sup>	1181 (0)	1.35	10.09	4.9	2050.7	902.4	5035
K02350.01	1132 (1109)	1.75	14.46	4.3	2325.8	1023.5	5325
K02355.01	1047 (1007)	1.64	12.07	5.7	1837.2	808.5	4859
K02393.02 <sup>e</sup>	1247 (0)	1.11	10.34	4.5	2082.2	916.3	4894
K02396.01	2287 (2037)	1.88	44.52	2.8	3008.5	1323.9	5529
K02409.01	1732 (1604)	1.47	25.49	3.7	2469.3	1086.6	5256
K02453.01 <sup>e</sup>	778 (0)	1.54	11.31	10.5	994.8	437.8	3565
K02480.01 <sup>e</sup>	1875 (0)	1.31	20.57	4.8	1649.8	726.0	3990
K02493.01	1537 (1446)	1.48	19.70	3.9	2375.5	1045.4	5166
K02589.01	1920 (1816)	1.19	12.56	3.8	2388.7	1051.2	5177
K02607.01 <sup>e</sup>	1620 (0)	1.49	15.53	3.9	2697.9	1187.2	5883
K02668.01	1321 (1227)	1.25	13.67	4.0	2534.2	1115.2	5596
K02694.01	1422 (1360)	1.57	16.83	4.1	2151.2	946.6	4818
K02699.01	2069 (1916)	1.51	24.85	3.5	2514.9	1106.7	5216
K02708.01	1438 (1366)	1.71	19.72	4.8	1967.6	865.9	4790
K02716.01	1281 (1218)	1.48	11.86	4.9	2322.0	1021.8	5693
K02735.01 <sup>e</sup>	2195 (0)	1.39	21.39	3.5	2507.3	1103.3	5154
K02763.01 <sup>e</sup>	2337 (0)	1.13	18.46	3.4	2354.9	1036.3	4787

Table 3.1 (cont'd)

KOI	# eclipses <sup>a</sup>	$R_p$ <sup>b</sup> ( $R_\oplus$ )	$(R_p/a)^{2b}$ (ppm)	$a/R_*$ <sup>b</sup>	Max $T_{eq}$ <sup>c</sup> (K)	Min $T_{eq}$ <sup>d</sup> (K)	$T_{eff}$ (K)
K02796.01 <sup>f</sup>	2262 (0)	1.01	10.62	2.8	3270.6	1439.2	6108
K02797.01	1275 (1243)	1.80	16.28	3.7	2904.4	1278.1	6173
K02817.01	956 (895)	1.45	20.62	3.9	2399.8	1056.0	5238
K02852.01	1600 (1498)	1.44	16.07	3.4	2913.1	1281.9	5966
K02882.02	1528 (1381)	1.04	17.46	3.7	2094.6	921.8	4467
K02886.01	1250 (1184)	1.28	10.16	4.7	2186.0	961.9	5260
K03089.01 <sup>e</sup>	1284 (0)	1.36	12.03	4.2	2335.0	1027.5	5269
K03246.01	1126 (1118)	1.86	27.52	1.9	3218.6	1416.4	4854
K03867.01	1390 (1346)	1.55	12.20	4.4	2508.0	1103.7	5825
K04002.01 <sup>e</sup>	1609 (0)	1.42	23.04	2.9	2856.2	1256.9	5396
K04109.01	1450 (1436)	1.53	20.19	1.8	3367.4	1481.9	4968
K04325.01	2017 (1908)	1.19	12.39	3.2	2993.9	1317.5	5936
K04512.01 <sup>e</sup>	1800 (0)	1.07	13.50	3.4	2576.4	1133.8	5286
K04595.01 <sup>e</sup>	2081 (0)	1.25	18.73	4.2	2203.3	969.6	4985

<sup>a</sup>Listed are the number of eclipses used for the group based on the Feb 2015 catalog. In parenthesis are the number of eclipses used for the shortened group.

<sup>b</sup> $R_p$ ,  $a$ , and  $R_*$  are taken from the Exoplanet Archive candidate table, and  $(R_p/a)^2$  and  $a/R_*$  are calculated from them.

<sup>c</sup>Assumes  $f = 2/3$  (instant re-radiation) and  $A_B = 0.0$ .

<sup>d</sup>Assumes  $f = 1/4$  (complete redistribution) and  $A_B = 0.9$  (i.e.  $A_g = 0.6$ ).

<sup>e</sup>Has false positive probability (Morton et al., 2016)  $> 1$  %.

<sup>f</sup>Is now listed as a false positive in the cumulative candidate table due to a non-transit-like shape.

Table 3.2. Candidate Parameters

KOI	# eclipses	<sup>a</sup> $R_p$ <sup>b</sup> ( $R_\oplus$ )	$(R_p/a)^{2b}$ (ppm)	$a/R_*$ <sup>b</sup>	Max $T_{eq}$ <sup>c</sup> (K)	Min $T_{eq}$ <sup>d</sup> (K)	$T_{eff}$ (K)
mini-Neptunes							
K00102.01	583 (576)	3.76	31.79	5.0	2324.7	1023.0	5731
K00104.01	461 (438)	2.49	11.63	11.0	1156.4	508.9	4238
K00191.02 <sup>e</sup>	383 (0)	2.79	12.14	8.4	1773.9	780.6	5700
K00220.01	525 (521)	3.60	19.98	8.9	1695.6	746.2	5588
K00439.01	676 (656)	3.92	32.24	7.7	1774.8	781.0	5438
K00496.01	796 (764)	2.54	17.58	5.2	2145.3	944.1	5417
K00517.01	429 (420)	3.64	16.30	7.1	1955.2	860.4	5749
K00526.01	619 (608)	2.96	14.50	7.3	1908.7	839.9	5705
K00676.02 <sup>e</sup>	436 (0)	2.23	10.58	11.9	1027.4	452.1	3914
K00697.01	205 (205)	3.49	12.83	5.7	2292.6	1008.9	6042
K00732.01	944 (895)	3.69	45.88	5.2	2193.5	965.2	5546
K00780.01	551 (529)	2.38	10.22	9.4	1472.0	647.8	4989
K00800.01	472 (462)	3.62	14.93	8.1	1962.1	863.4	6167
K00844.01	271 (267)	3.96	13.33	11.7	1475.3	649.2	5576
K00916.01	395 (387)	3.63	12.75	9.9	1613.6	710.1	5609
K00926.01	401 (401)	3.97	15.32	9.3	1778.9	782.8	6007
K00941.02	382 (376)	2.67	11.66	7.4	1727.8	760.3	5188
K01357.01 <sup>e</sup>	356 (0)	3.09	10.93	9.0	1570.4	691.1	5209
K01393.01 <sup>e</sup>	650 (0)	2.55	22.10	8.8	1177.7	518.3	3872
K01428.01	1360 (1252)	2.10	27.68	4.7	2053.5	903.6	4911
K01557.01	268 (257)	3.80	15.81	9.8	1416.2	623.2	4910
K01762.01 <sup>e</sup>	1480 (0)	2.24	29.72	4.3	2619.3	1152.6	5985
K01835.02	338 (337)	2.55	10.90	4.4	2225.9	979.5	5192
K01845.01	615 (609)	3.35	22.17	3.9	2231.5	982.0	4883
K01988.01	1312 (1280)	3.48	64.88	2.2	2907.0	1279.2	4777
K02034.01	228 (226)	3.47	10.55	11.3	1525.3	671.2	5668
K02104.01	590 (551)	3.11	15.45	6.5	2174.7	957.0	6153
K02269.01 <sup>e</sup>	1850 (0)	2.78	57.60	2.6	3634.2	1599.3	6517
K02715.02	271 (262)	3.26	21.13	9.2	1306.3	574.8	4385
K02795.01 <sup>e</sup>	424 (0)	3.87	18.04	7.2	2105.6	926.6	6237
K02842.01	310 (292)	2.61	29.11	9.6	1015.7	447.0	3485
K03913.01 <sup>e</sup>	2126 (0)	2.53	59.23	3.0	3275.9	1441.6	6263
K03984.01	858 (849)	2.20	14.62	3.6	2513.6	1106.1	5305
K04098.01 <sup>e</sup>	814 (0)	2.38	20.85	1.9	3330.4	1465.6	5023
K04561.01	58 (50)	2.34	14.25	4.5	2692.0	1184.6	6302
K04928.01	85 (80)	2.27	16.50	27.1	557.7	245.4	3212
K05566.01	30 (30)	3.19	37.45	1.7	4445.5	1956.3	6456
K05717.01 <sup>e</sup>	125 (0)	3.94	60.91	6.1	1689.1	743.3	4611
super-Neptunes							
K00007.01	258 (258)	4.14	16.13	6.2	2104.8	926.2	5781
K00046.01	350 (349)	4.36	15.74	8.3	1803.3	793.6	5761
K00141.01 <sup>e</sup>	430 (0)	5.14	34.63	9.1	1610.4	708.7	5377
K00221.01	371 (367)	4.55	22.78	12.2	1377.7	606.2	5332

Table 3.2 (cont'd)

KOI	# eclipses <sup>a</sup>	$R_p^b$ ( $R_\oplus$ )	$(R_p/a)^{2b}$ (ppm)	$a/R_*$ <sup>b</sup>	Max $T_{eq}^c$ (K)	Min $T_{eq}^d$ (K)	$T_{eff}$ (K)
K00240.01	303 (296)	4.07	10.62	11.1	1688.4	743.0	6225
K00242.01	177 (175)	5.70	10.88	17.2	1228.1	540.4	5638
K00433.01	261 (259)	4.86	17.99	11.7	1467.9	646.0	5551
K00470.01	273 (268)	4.74	17.40	11.0	1576.6	693.8	5776
K00531.01 <sup>e</sup>	322 (0)	5.69	36.88	14.3	962.8	423.7	4030
K00766.01	307 (306)	4.46	12.89	10.3	1737.0	764.4	6174
K00782.01	196 (196)	5.38	11.69	14.6	1418.4	624.2	5992
K00851.01	262 (260)	5.69	20.52	13.1	1450.6	638.3	5815
K00953.01	349 (348)	4.87	20.15	10.8	1579.6	695.1	5739
K01815.01	354 (353)	5.46	31.55	5.1	1943.8	855.4	4854
K01845.02 <sup>e</sup>	219 (0)	5.99	20.24	7.3	1631.3	717.9	4883
K02688.01	140 (139)	5.20	19.31	18.3	874.4	384.8	4141

<sup>a</sup>Listed are the number of eclipses used for the groups based on the Feb 2015 catalog. In parenthesis are the number of eclipses used for the shortened groups.

<sup>b</sup> $R_p$ ,  $a$ , and  $R_*$  are taken from the Exoplanet Archive candidate table, and  $(R_p/a)^2$  and  $a/R_*$  are calculated from them.

<sup>c</sup>Assumes  $f = 2/3$  (instant re-radiation) and  $A_B = 0.0$ .

<sup>d</sup>Assumes  $f = 1/4$  (complete redistribution) and  $A_B = 0.9$  (i.e.  $A_g = 0.6$ ).

<sup>e</sup>Has false positive probability (Morton et al., 2016)  $> 1\%$ .

I use the long cadence ( $\approx 30$  min exposure) Pre-search Data Conditioning (PDC) data from the Mikulski Archive for Space Telescopes (MAST<sup>2</sup>), for quarters 0 through 17. I first eliminate statistical outliers from the photometric data by removing any point that is more than three times the photometric error away from the median value of the point and the four points to each side. I normalize the light curves by dividing the photometric time series for each quarter by its mean value, and then subtracting 1 and multiplying by  $10^6$  to convert to ppm. I mask any transits of other known objects in the system. I select data within  $\pm 12$  hours of each eclipse time, with two restrictions, and I fit a quadratic baseline to the portion of those data

<sup>2</sup><http://archive.stsci.edu/kepler/>

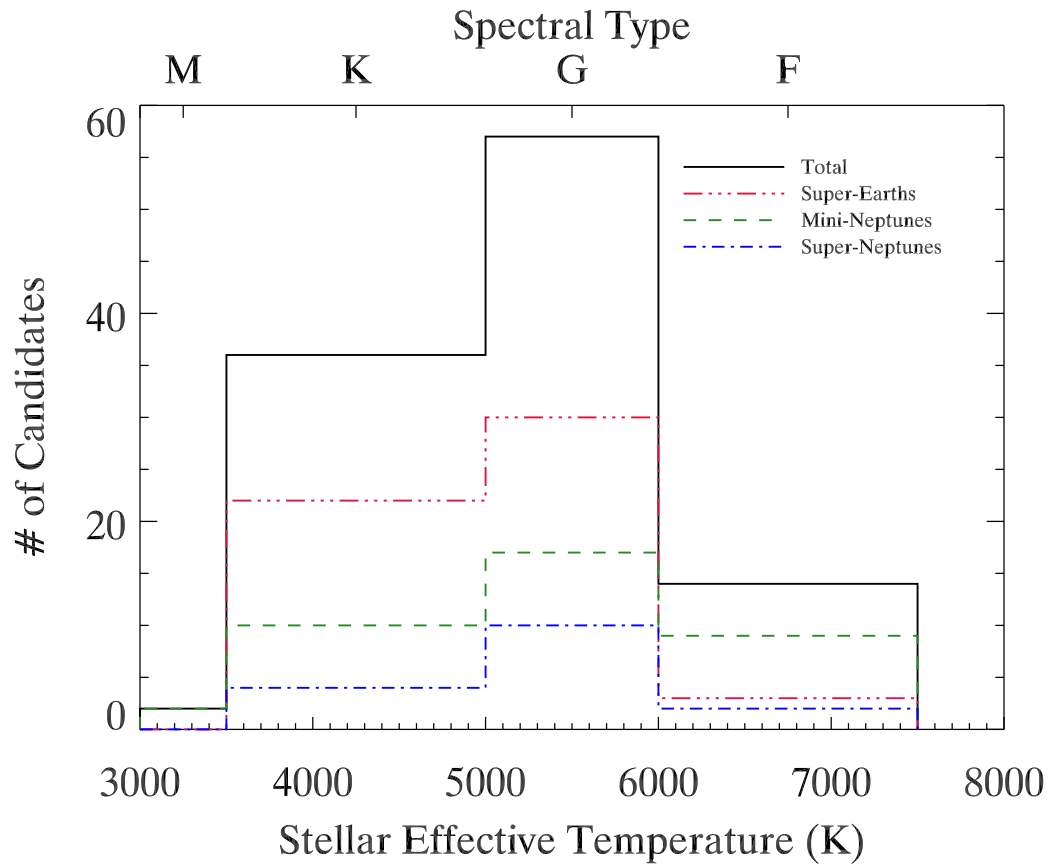


Figure 3.1 The spectral types of the host stars for each radius group. Super-Earths are in red, mini-Neptunes in green, and super-Neptunes in blue. Also shown is the total of the 3 groups in black. Most of the host stars are G and K stars. The two M stars in the sample host mini-Neptunes.

that lie outside of the eclipse. For candidates with transits (and, therefore, eclipses) whose duration is greater than 4 hours, I widen the data selection window from 12 hours to 3 times the duration of the candidate’s transit. This provides a better baseline for longer-duration eclipses. For candidates with orbital periods around 1 day or less, the 12 hour selection window around the eclipse center would include the transits, so I also adapt the data selection window for these candidates to be short enough to avoid the transits. I then subtract the quadratic fit, and repeat the process for all eclipses of the candidate in each photometric data file. For the long cadence data, each file spans one observing quarter, which is about 3 months. I eliminate any eclipses that do not have at least 1 point whose midpoint of the exposure time falls between second and third contact, and I also eliminate eclipses that do not have at least 8 data points before eclipse and at least 8 data points after eclipse. I eliminate additional statistical outliers from the photometric data by removing any point that is more than three times the standard deviation of the data points around the quadratic fit.

### 3.3 Averaging the Long Cadence Data

#### 3.3.1 Scaling and Stacking the Individual Eclipses

I apply four tests to individual eclipses for each object in each group to eliminate excessive noise or instrument artifacts. The 30 min integration time of the long cadence data means that there are fewer data points per eclipse, thus I cannot apply the red noise test used for the short cadence data in Chapter 2. In its place, I use

two tests. First, I check that the scatter of the points ( $\sigma$ ) around the quadratic fit from Section 3.2 is consistent with the mean photometric noise ( $\sigma_{phot}$ ). The mean photometric noise is the average of the propagated photometric errors for the data points. I record the value of  $\sigma/\sigma_{phot}$  for every eclipse, whether it passes or fails, for all of my selected candidates, and plot a histogram of the values. The histograms of these values are consistent with a Gaussian distribution until a ratio of about 1.3, shown in Figure 3.2, so I eliminate any eclipse with a ratio greater than 1.3. I also check that the scatter of the points inside eclipse ( $\sigma_{ecl}$ ) is consistent with the overall scatter of the points ( $\sigma$ ). The histograms of the ratio  $\sigma_{ecl}/\sigma$  begin to deviate from Gaussian at a value of about 1.5, shown in Figure 3.3. For the Feb 2015 versions of the 3 radius groups, I allowed values up to 2, but for the shortened groups I used the cut-off of 1.5. Note that the typical photometric errors for a single eclipse are several orders of magnitude larger than the eclipse signatures for these candidates, so this test should not be eliminating the signal of interest (see Sections 3.3.2.4-5).

The third test I perform is a modification of the projection test from Chapter 2. An example of an eclipse which fails this test is given in Figure 3.4. I take a linear fit to the data points before ingress and use that fit to calculate a value for each of the data points after egress. Previously I considered only the difference between the mean value of the calculated points after egress and the mean value of the actual data points after egress. Now I instead eliminate eclipses where the difference is more than three times the mean photometric noise of the data (i.e. more than  $3\sigma$ ). I also fit a line to the points after egress and project that line to the points before ingress. The eclipse fails the test if either of the two projections fail to match the

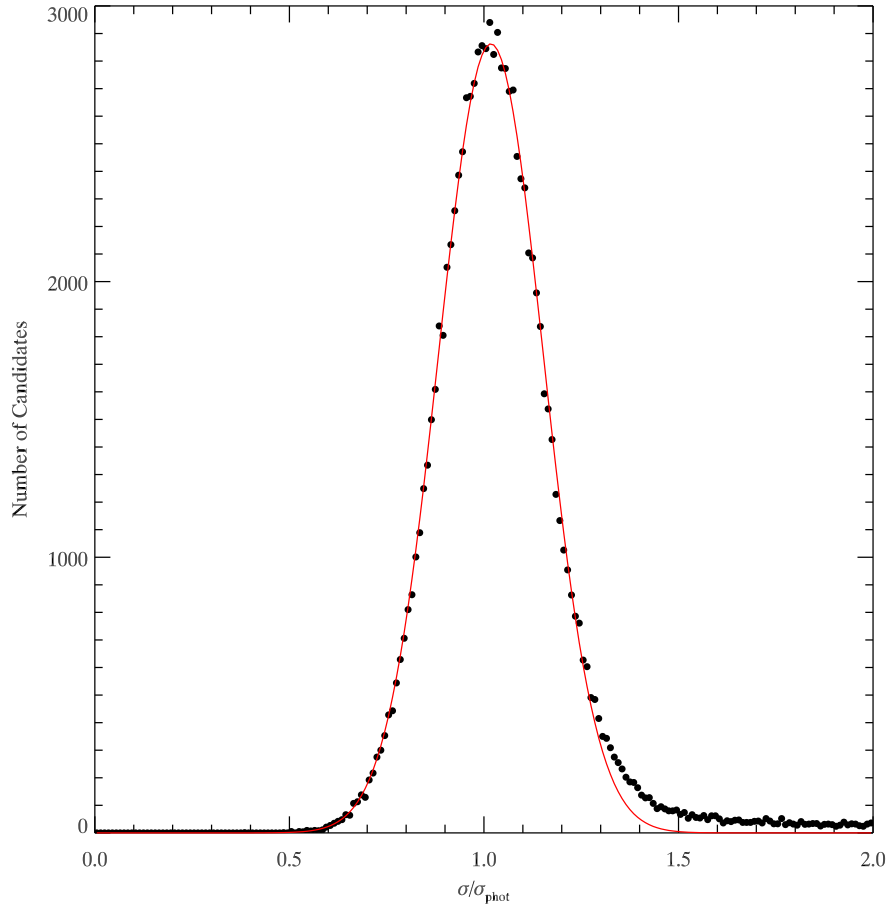


Figure 3.2 Shown is the histogram of the ratio of the scatter about the quadratic fit ( $\sigma$ ) to the photometric noise ( $\sigma_{phot}$ ) for all eclipses. I use a cut-off of 1.3 for this parameter, keeping all eclipses with a value less than the cut-off.

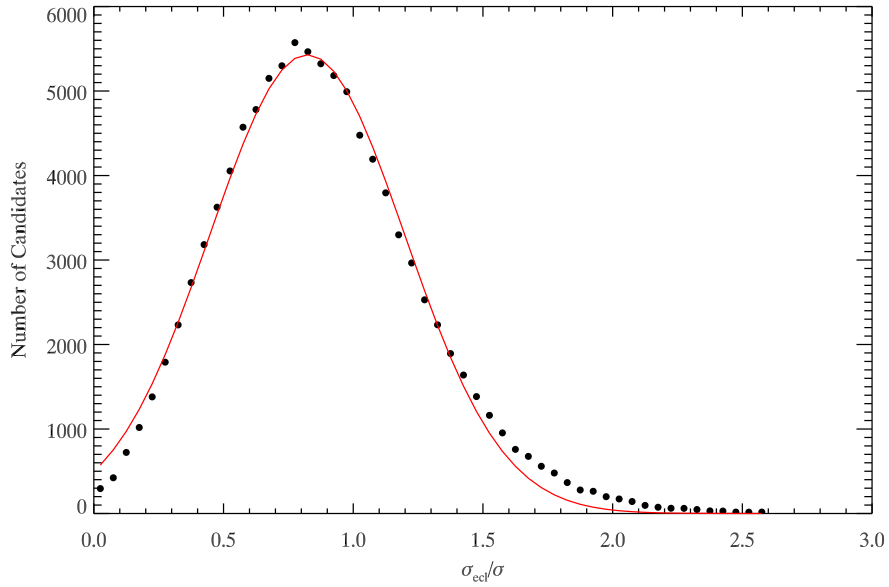


Figure 3.3 Shown is a histogram of the ratio of the scatter about the quadratic fit for the in-eclipse points only ( $\sigma_{ecl}$ ) over the scatter about the quadratic fit for all of the points ( $\sigma$ ). I use a cut-off of 2.0 for the parameter for the groups using the Feb 2015 catalog, keeping all eclipses with a value less than the cut-off. I use a slightly more restrictive cut-off of 1.5 for the results using the shortened groups.

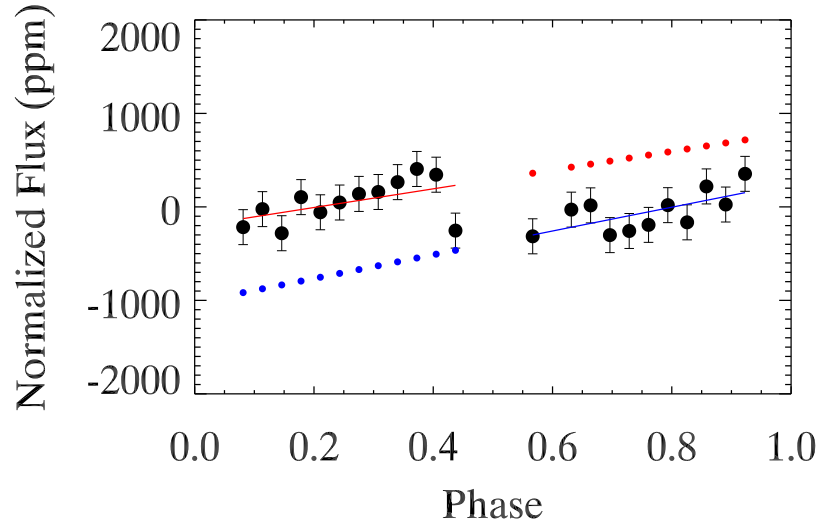


Figure 3.4 Shown is a single eclipse from KOI 1300.01 which fails the long cadence projection test. In the test, a line (in red) is fit to the data points (in black, with error bars) on the left (before ingress) and extrapolated (red points) for the data points (again, in black with error bars) on the right. Similarly, a line (in blue) is fit to the black points on the right (after egress) and extrapolated (blue points) for the black points on the left. For each side of the eclipse, the mean of the extrapolated points is calculated, as is the mean of the data points. If the mean of the extrapolated points differs from the mean of the data points, on one side or the other, by more than three times the mean photometric errors, the eclipse is excluded.

data.

The fourth test I perform is the slope test from Chapter 2. I use the slopes from the linear fits in the projection test and check that they are both consistent with zero. Any phase curve variation would be well below the photometric noise of an individual eclipse, and so no slope should be detectable. If the slope of both of the fits before ingress and after egress are within  $3\sigma$  of zero, the eclipse is retained.

I track the number of eclipses kept for each candidate as well as the number of eclipses rejected by each of the four tests above. Candidates with more total rejected eclipses than retained eclipses are eliminated from the groups entirely. I eliminate four super-Earths (KOIs 1957.01, 2324.01, 2548.01, and 3204.01), three mini-Neptunes (KOIs 2035.01, 2276.01, and 2678.01), and four super-Neptunes (KOIs 3.01, 1779.01, 1803.01, and 1804.01).

To average the light curves constructively, I use the same equations as Section 2.3 to transform the phase before binning the data. Transforming the phase ensures that I am adding data points inside of eclipse for one object to points inside of eclipse for another object, and likewise for points outside of eclipse. Though I use points at phase outside of the 0.25 to 0.75 range to normalize the data, I only average points inside of this range. For my assumption of circular orbits, phases of 0.25 and 0.75 are the inflection points of the phase curve, so I select these points as limits. The only modifications I make to accommodate the long cadence data are to remove the separate ingress and egress bins that I utilized for the short cadence data and to reduce the number of bins within eclipse to 7 from 11. Ingress and egress are typically quite short compared to the 30 min cadence, so separate bins for these two stages are no longer useful.

As I stack the eclipses of all of the candidates in each group, I also check the stacked eclipses for each candidate alone for significant secondary eclipses. I eliminate candidates with a significant secondary eclipse (i.e. greater than  $3\sigma$  detection) if the depth of the eclipse is incompatible with the planet interpretation, such as for KOIs 4294.01 and 4351.01 (see Sections 3.3.2.4-5).

### 3.3.2 Notes on Individual Candidates

We first constructed lists for the three radius bins from the cumulative table downloaded from the NASA Exoplanet Archive on 27 August 2014. The various versions of the catalog that are combined to create the cumulative table were not all finalized at that time. Many of the candidates discussed in this subsection came to our attention either while working with the Aug 2014 version of the cumulative table, or while comparing the Aug 2014 version, the downloaded version from 23 Feb 2015, and the now-finalized versions of the catalogs through the Q1-17 DR 24 release (Coughlin et al., 2016). We comment here on the objects that we found notable, as guidance for other investigations.

#### 3.3.2.1 KOI 1662.01

KOI 1662.01 was listed as a  $1.66 R_{\oplus}$  candidate in the Q1-12 catalog with a period of 0.784 days. It is now listed as a false positive in the Q1-17 catalog due to a significant secondary eclipse. The period is still listed as 0.784 days, but the true period is twice this value. The Q1-17 DR25 TCE (Threshold-Crossing Events) table at the NASA Exoplanet Archive lists two “planets” for this star: one at the 0.784 day period and one at twice that period. Fig. 3.5 shows the data phase-folded at the 1.568 day period, with a significant secondary eclipse, indicating that it is a blended eclipsing binary. It is included as a super-Earth in the tests discussed in Section 3.5 as well as the Feb 2015 group in Section 3.6, but removed from the shortened group of super-Earths.

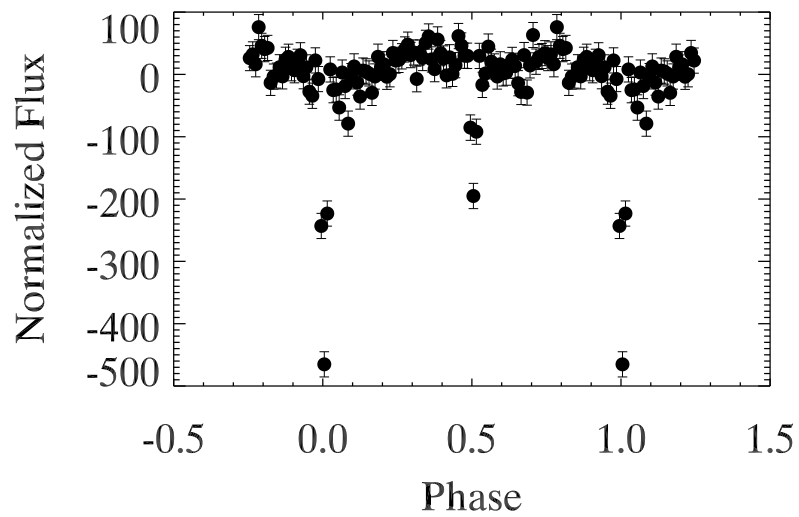


Figure 3.5 The light curve for KOI 1662.01, phase-folded at twice the period listed in the current KOI catalog. This KOI is now listed as a false positive for a significant secondary eclipse, and I confirm that the secondary eclipse is significantly different in depth than the primary eclipse, making it some type of eclipsing binary.

### 3.3.2.2 KOIs 2396.01 and 2882.02

KOIs 2396.01 and 2882.02 are also now listed in the Q1-17 catalog as false positives for significant secondaries. I retain these two candidates in my shortened group of super-Earths because I do not see a secondary eclipse when folding at their planet candidate periods, nor do I see a significant difference between the “primary” and “secondary” eclipse depths when folding at twice the listed period. Furthermore, they have less than a 1% false positive probability in [Morton et al. \(2016\)](#), unlike KOI 1662.01.

### 3.3.2.3 KOI 2795.01

KOI 2795.01 is listed as a  $2.4 R_{\oplus}$  candidate in the Q1-8 catalog and as a false positive due to a significant secondary eclipse in the Q1-17 DR 24 catalog. I find that the signal strength for 2795.01 changes depending on the orientation of the telescope. It appears strongly in Q6, Q10, and Q14, and to a lesser extent in Q7, Q11, and Q15. There are no data for Q0-3, and the signal appears only weakly in the remaining quarters. Furthermore, the shape of the light curve changes when comparing the weak signal quarters, shown in [Fig. 3.6](#), to the strong signal quarters, shown in [Fig. 3.7](#). The spacecraft rolls by 90 degrees at the end of each quarter, and so on every fourth quarter, a target returns to the same CCD. This correlation with certain orientations of the telescope suggests contamination by electrical cross-talk, a column anomaly, or internal reflections ([Coughlin et al., 2014](#)). It is included in my tests discussed in [Section 3.5](#) and my Feb 2015 mini-Neptunes group in [Section](#)

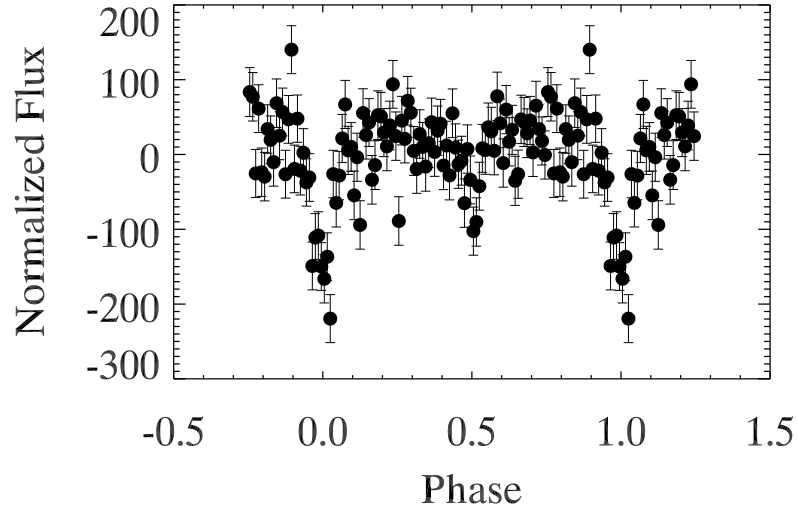


Figure 3.6 Averaged light curve for KOI 2795.01 from Q4, Q5, Q8, Q9, Q12, Q13, Q16, and Q17, where only a weak signal is present. Here I see a significant secondary eclipse at phase 0.5.

3.6, but it is not included in the shortened group of mini-Neptunes.

#### 3.3.2.4 KOI 4294.01

KOI 4294.01 was listed as a  $5.02 R_{\oplus}$  candidate in the cumulative KOI table downloaded on 27 August 2014. I detected a significant secondary eclipse that was much too deep to be the secondary eclipse of a planet. It was independently found to have a significant secondary in the Q1-17 DR 24 catalog and is now listed as a false positive. I do not include it in either of my super-Neptune groups.

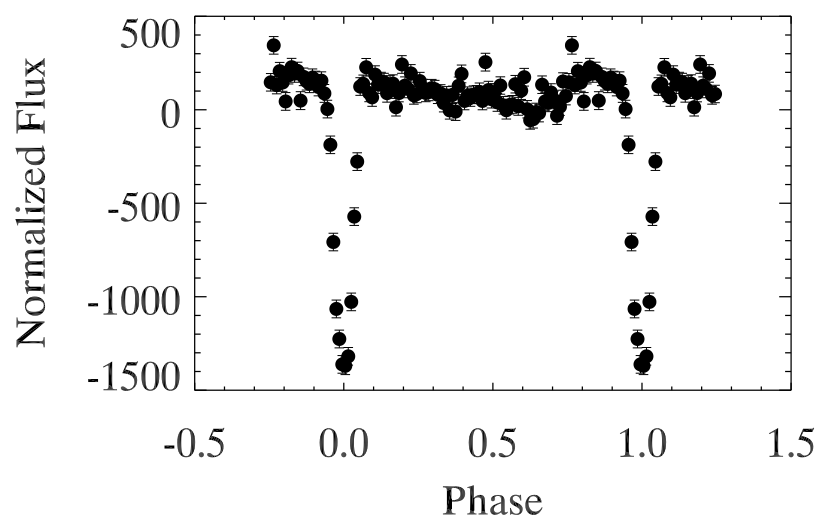


Figure 3.7 Averaged light curve for KOI 2795.01 from Q6, Q10, and Q14, where a strong signal is present. Here I see a much stronger primary eclipse at phase 0.0 (and repeated at phase 1.0) than the primary eclipse in Fig. 3.6.

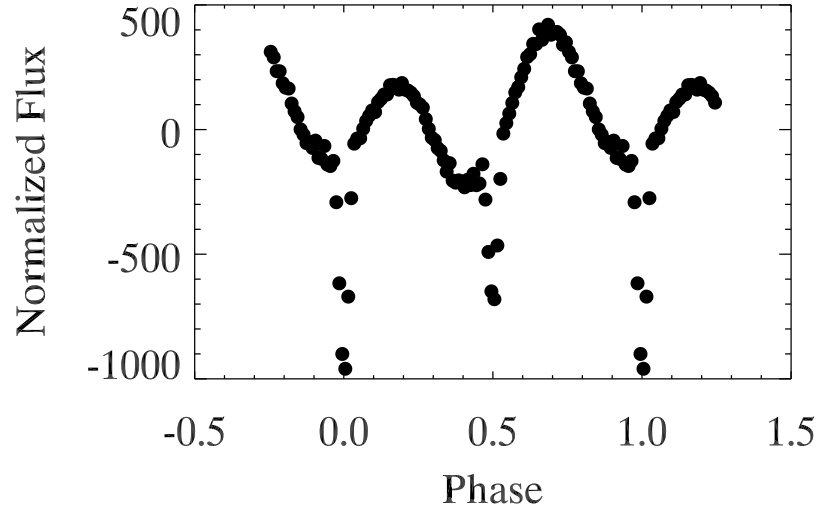


Figure 3.8 Averaged light curve for KOI 4351.01, which is listed in the KOI catalog as a planet candidate. It shows a significant secondary eclipse at phase 0.5 and so must be an eclipsing binary.

### 3.3.2.5 KOI 4351.01

KOI 4351.01 was listed as a  $5.47 R_{\oplus}$  candidate in the cumulative KOI table downloaded on 27 August 2014. Like KOI 4294.01 above, I detected a significant, non-planetary secondary eclipse while screening the candidates to be used in my average, indicating the object is actually an eclipsing binary. Unlike KOI 4294.01, this candidate was not re-evaluated in the Q1-17 DR 24 catalog (Coughlin, private communication). It is listed in the finalized Q1-12 catalog and the current cumulative table as a  $24.4 R_{\oplus}$  candidate. The secondary eclipse is shown in Fig. 3.8. I do not include it in either of my super-Neptune groups.

### 3.3.2.6 KOI 4924.01

KOI 4924.01 was listed as a  $3.65 R_{\oplus}$  candidate in the cumulative KOI table downloaded on 27 August 2014. Subsequently, it was listed as a false positive in the cumulative KOI table downloaded on 23 February 2015. In the finalized Q1-16 catalog, it is still listed as a false positive due to a centroid offset flag, but in the finalized Q1-17 DR 24 catalog, it is listed as a  $3.49 R_{\oplus}$  candidate. I do not include it in either of my mini-Neptune groups.

## 3.4 Modeling Reflected Light and Thermal Emission

As in Chapter 2, the reflected light is given by Equation 1.1, while the thermal emission calculation begins with the equilibrium temperature from Equation 1.2. I again consider  $f = 1/4$  for uniform redistribution of heat around the planet and  $f = 2/3$  for instantaneous re-radiation (see, e.g. Esteves et al., 2013; Hansen, 2008; López-Morales & Seager, 2007; Rowe et al., 2006). I also adopt  $A_B = (3/2)A_g$ , which is the relation for a Lambertian surface. I treat the planet as a blackbody with this effective temperature, integrated over the bandpass of *Kepler* using its transmission function<sup>3</sup>. I calculate the planet’s intensity for the two extremes of  $f$ . I integrate the ATLAS<sup>4</sup> model atmosphere (Kurucz, 1979) over the bandpass for the appropriate stellar parameters to calculate the stellar intensities. I finally divide the planet’s intensity by the stellar intensity and scale by  $(R_p/R_*)^2$ .

---

<sup>3</sup>[http://keplergo.arc.nasa.gov/kepler\\_response\\_hires1.txt](http://keplergo.arc.nasa.gov/kepler_response_hires1.txt)

<sup>4</sup><http://kurucz.harvard.edu/>

The combination of the thermal emission and reflected light gives the expected depth of the secondary eclipse. I then take that depth and multiply it by a [Mandel & Agol \(2002\)](#) model for the eclipse, which has been rescaled so that the continuum is 0 and full eclipse is -1. To account for the 30 min cadence of the long cadence data, I oversample the [Mandel & Agol \(2002\)](#) model and average it over the 30 min exposure corresponding to each data point before multiplying by the expected depth for the thermal emission plus reflected light. I then build up a thermal emission and reflected light model for the averaged data by generating a model point for each data point and averaging the model points just as the data are averaged. To determine the average geometric albedo, I iteratively adjust the geometric albedo used to calculate the model until the averaged model matches the fitted depth of the averaged data.

### 3.5 False Positive and Other Detrimental Scenarios

In anticipation of my results, I here discuss possible scenarios that could falsely drive down my measured albedos.

#### 3.5.1 Dilution by Unknown Objects in Aperture

I considered the possibility that some of the host stars in my candidate sample may have a close, unresolved companion star in the *Kepler* data, due to the large pixel scale of  $3.98 \text{ arcsec pixel}^{-1}$  ([Koch et al., 2010](#)). Unresolved companions dilute the signal from the planet in transit and in eclipse, making the planet seem smaller

than it truly is. This possible dilution means that some of my candidates may be in the wrong radius bin. Even if the inferred radius of a candidate is wrong, however, the geometric albedo calculated from the candidate is unaffected. For clarity, I demonstrate that the inferred albedo is unaffected for one particular example of dilution. This demonstration, however, is easily generalized to an arbitrary degree of dilution.

If there is only one star, the undiluted transit depth is just  $R_p^2/R_*^2$ , where  $R_p$  is the real planet radius and  $R_*$  is the host star radius. If there are two stars, and the diluting star is equally as bright as the host star, then the observed transit depth is

$$\frac{R_{p,inf}^2}{R_*^2} = \frac{1}{2} \frac{R_p^2}{R_*^2} \quad (3.1)$$

where  $R_{p,inf}^2$  is the inferred planet radius from the diluted transit. Thus the inferred radius is

$$R_{p,inf} = \frac{R_p}{\sqrt{2}} \quad (3.2)$$

The real secondary eclipse depth is  $A_g * (R_p/a)^2$ , where  $A_g$  is the actual geometric albedo of the planet and  $a$  is the semi-major axis of its orbit, while the observed eclipse depth is

$$\frac{A_{g,inf} R_{p,inf}^2}{a^2} = \frac{A_g R_p^2}{2a^2} \quad (3.3)$$

where  $A_{g,inf}$  is the inferred geometric albedo from the diluted transit. Substituting Equation 3.2 into Equation 3.3 gives

$$\frac{A_{g,inf} R_p^2}{2a^2} = \frac{A_g R_p^2}{2a^2} \quad (3.4)$$

which means that  $A_{g,inf} = A_g$ . I thus conclude that dilution has no effect on my

inferred albedos. It does affect the radius groups to which I assign each planet, but I do not believe this secondary effect is of importance to my analysis.

### 3.5.2 Eccentric Eclipsing Binaries

Eccentric eclipsing binaries lurking in my sample could weaken the average secondary eclipse measured. I believe that my inspection of individual candidates in Section 3.3.2, combined with the use of the false positive probabilities from [Morton et al. \(2016\)](#), eliminates significant contamination of my sample by conventional eclipsing binaries. There remains, however, the possibility that unusual eclipsing binaries, such as those with highly eccentric orbits, may still be present in the sample. The eccentric binary might have a weak secondary eclipse that occurs at a phase much different than 0.5, or the eccentricity may be so high that, due to viewing geometry, only the primary eclipse or the secondary eclipse occurs, but not both. In either case, it would introduce a flat light curve where I am expecting a secondary eclipse for a planet. I tested the effect of possible eccentric eclipsing binaries as false positives contaminating my sample. [Santerne et al. \(2013\)](#) and references therein report that less than 1% of eclipsing binaries with periods under 10 days have significant eccentricity. This is the period regime of my candidate sample. I fit a model to stacked eclipses of each individual candidate to find the candidate's eclipse depth and calculated the weight of the candidate in the overall stacked eclipse. I then used those weights and candidate eclipse depths to determine a weighted average eclipse depth for the group. I considered the worst case scenario,

where all the candidates in the sample are eclipsing binaries, with 1% being eccentric (Santerne et al., 2013). I randomly drew  $\sim 1\%$  of the individual eclipse depths and set them to zero to represent an absence of the eclipse at phase 0.5. I repeated this 100,000 times and found that the resulting average depth varies from the original average depth by at most a few hundredths of a ppm, so I conclude that eccentric eclipsing binaries are not a significant source of concern within my sample.

### 3.5.3 Half-Period Eclipsing Binaries

An eclipsing binary consisting of two similar stars would result in a light curve with a primary eclipse and secondary eclipse that have similar depths. This mimics a planet at half the period of the binary, resulting in a flat light curve at phase 0.5 when phase-folding to the planet candidate period. The false positive probability calculations of Morton et al. (2016) take into account this scenario. Only a few of my original candidates show greater than a 1% chance of being an eclipsing binary false positive for this scenario, so I do not believe this could be a significant contributor to the low albedos I find in Section 3.6.

### 3.5.4 Eccentric Planets

I also considered my adoption of circular orbits of the planets. If any of the planet candidates in my sample are eccentric, the secondary eclipse is displaced from phase 0.5. To test how this affects my results, I assigned each object in the super-Earth group (excluding Kepler 10b) a random eccentricity, drawing from a

Rayleigh distribution with scale parameter  $\sigma_e = 0.017$ . [Hadden & Lithwick \(2014\)](#) found that small planets ( $< 2.5 R_{\oplus}$ ) in multi-planet systems have eccentricities with this distribution, while larger planets have smaller eccentricities, with  $\sigma_e = 0.008$ . Because planets in multi-planet systems can have non-zero eccentricities due to mutual perturbations, this is a worst-case scenario for my sample, which contains many single-planet systems. After assigning a random eccentricity and a random argument of pericenter (uniformly distributed from 0 to  $2\pi$ ), I calculated a thermal plus reflected light model for each individual eclipse for every candidate, assuming  $f = 1/4$  and  $A_g = 0.108$ , which is the average albedo I found for the group (see Section 3.6.1). I then averaged the model eclipse curves just as the data are averaged. I repeated this for a total of 100 trials, and the resulting averaged model curves are shown in green in Figure 3.9. Overplotted in black is the model curve using zero eccentricity for all of the candidates. The 100 averaged model curves have a mean depth of 2.449 ppm, and the shallowest averaged model curve has a depth of 2.412 ppm, versus the depth for the zero eccentricity of 2.473 ppm. The difference is similar to the error bars on the measured depth of the averaged data, which means that this effect does not drastically change the measured albedo for the group.

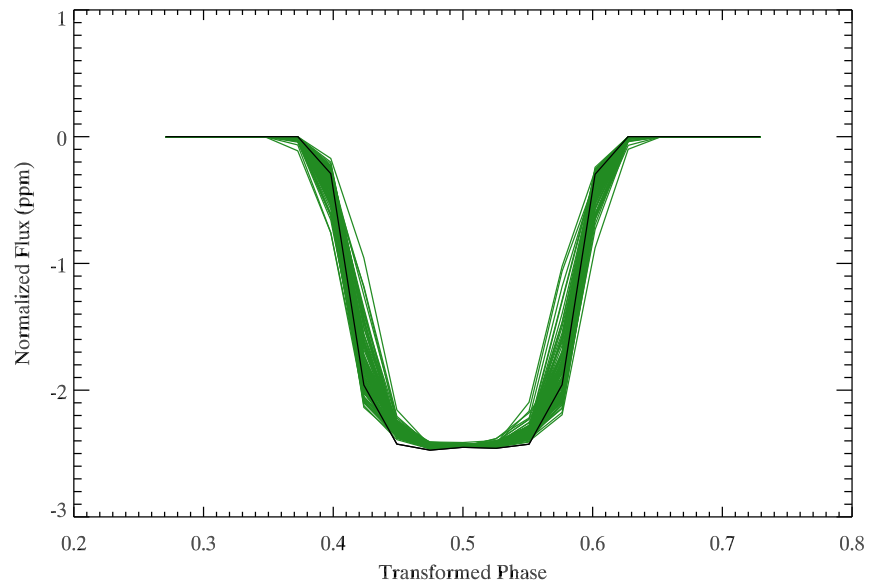


Figure 3.9 Shown are the averaged model curves for 100 trials of the super-Earth group, in green, assuming eccentricities for the planets drawn from a Rayleigh distribution. In black is the averaged model curve assuming zero eccentricity for all planets.

## 3.6 Results and Discussion

### 3.6.1 Super-Earths

#### 3.6.1.1 Excluding Kepler-10b

As in Chapter 2, I average the 1-2  $R_{\oplus}$  group without Kepler-10b, because Kepler-10 dominates the average. Kepler-10 is a bright star, and the weighting is done by the photometric errors. Kepler-10b also has an unusually deep secondary eclipse, requiring either a high albedo or some emission source beyond the blackbody emission for a planet in equilibrium with the incoming stellar light. To determine the fitted depth of the averaged data, I generate a model for the eclipse. I create a model point that corresponds to each data point, using the [Mandel & Agol \(2002\)](#) model, scaled so that the continuum is 0 and full eclipse is -1, and averaged over the 30 min exposure for the corresponding data point. I average the model points with the same weights as the corresponding data points. I then use a simple 2-parameter Markov Chain Monte Carlo (MCMC) procedure with 500,000 steps, as in Chapter 2, fitting the equation  $F_b + \delta x$ , where  $F_b$  adjusts the continuum level,  $x$  is the model, and  $\delta$  is the depth of the eclipse.

The result for the Feb 2015 list of super-Earths is shown in Figure [3.10](#). This group contains 55 candidates and 79,678 individual eclipses. The weighted average depth is  $2.44 \pm 0.99$  ppm, which corresponds to a geometric albedo  $A_g = 0.11 \pm 0.06$  in the case of complete redistribution of heat. In the case of instantaneous re-radiation, the measured depth corresponds to an unphysical, negative value for

albedo, but I can set an upper,  $3\sigma$  limit of  $A_g < 0.17$ . The shortened group, removing false positives identified in the finalized catalogs and candidates with high false positive probability, gives similar results, shown in Figure 3.11. The shortened group contains 39 candidates and 50,805 eclipses. The weighted average depth is  $2.63^{+1.13}_{-1.14}$  ppm, but the weighted average  $(R_p/a)^2$  increases as well, from  $1.517 R_\oplus$  to  $1.578 R_\oplus$ , and so the change in eclipse depth is not sufficient to change the values of the albedos significantly. I know that the Feb 2015 list contained one definite false positive, KOI 1662.02, which was removed from the shortened list. Including KOI 1662.02 in the average was adding a flat curve at secondary eclipse. Since removing it did not appreciably change the group’s average albedo, this suggests that most of the candidates are indeed dark, rather than the average being pulled down by false positives.

### 3.6.1.2 Including Kepler-10b

Adding Kepler-10b to the group, not surprisingly, increases the average albedo. The result for the Feb 2015 group is shown in Figure 3.12, with 56 candidates and 80,492 individual eclipses. The weighted average eclipse depth is  $3.56 \pm 0.65$  ppm, corresponding to an average geometric albedo of  $A_g = 0.19 \pm 0.04$  in the case of full heat redistribution, or  $A_g = 0.04 \pm 0.07$  for instantaneous re-radiation. The shortened list result, consisting of 40 candidates and 51,597 eclipses, is shown in Figure 3.13, with the same eclipse depth of 3.56 ppm, but slightly larger error bars of  $\pm 0.67$  ppm. This results in the same geometric albedo as the Feb 2015 group for

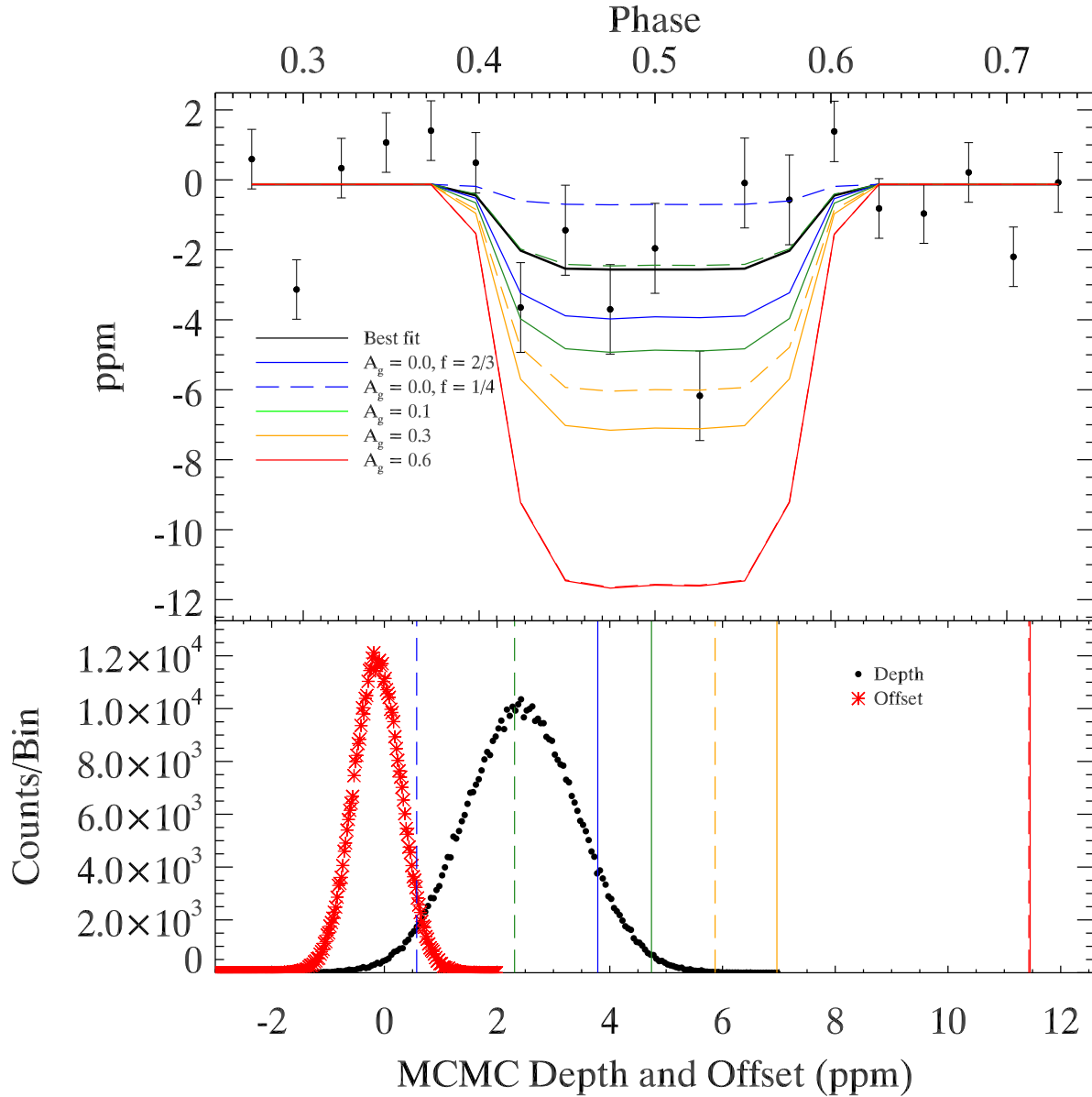


Figure 3.10 Upper panel: The averaged light curve, centered on secondary eclipse, for the super-Earth group using the Feb 2015 catalog, excluding Kepler-10b. The binned data are shown as points. The error bars are the propagated photometric errors. The best fit curve is the solid black line. Overplotted are the reflected light plus thermal emission models for  $A_g = (2/3) * A_B = 0.0$  (blue), 0.1 (green), 0.3 (orange), and 0.6 (red), with the re-radiation factor  $f = 1/4$  (dashed) and  $2/3$  (solid). Lower panel: The distributions for the two parameters of the MCMC run, with the depths from the reflected light plus thermal emission from the upper panel plotted as vertical lines. The two fitted parameters are eclipse depth ( $2.44 \pm 0.99$  ppm) and continuum offset from zero ( $-0.12 \pm 0.42$  ppm).

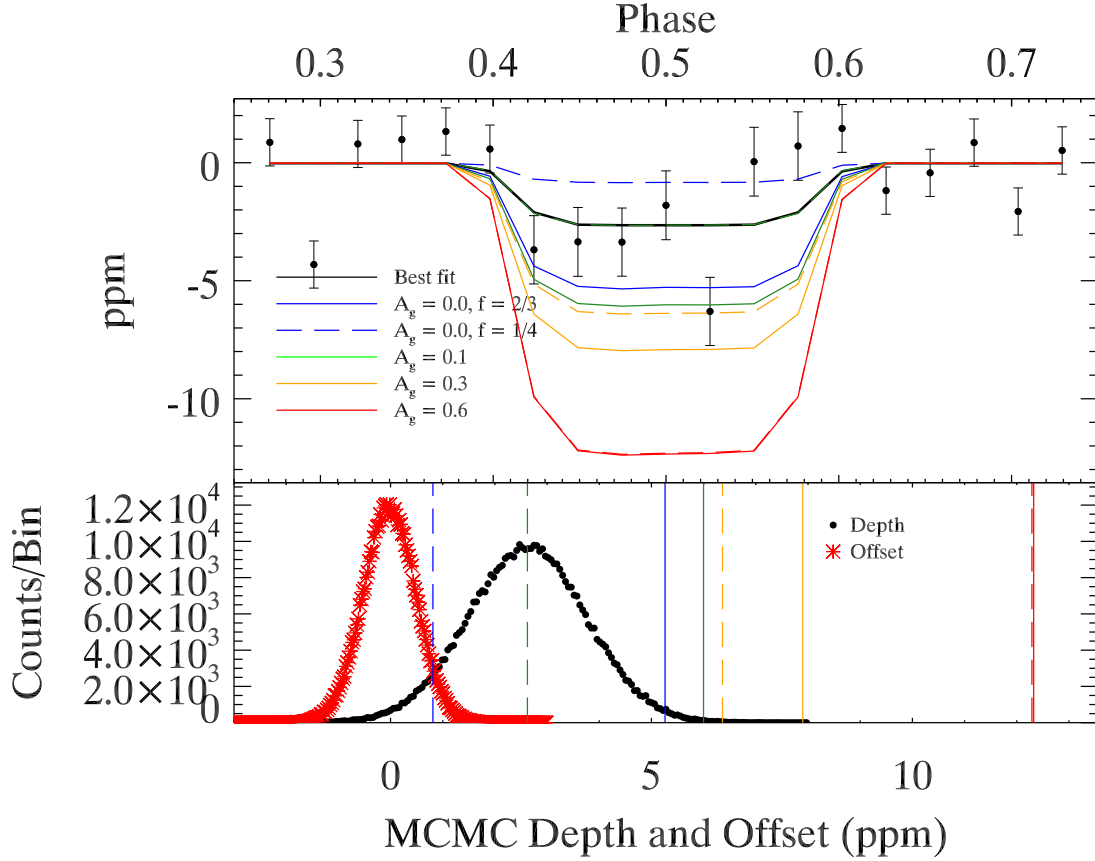


Figure 3.11 Upper panel: The averaged light curve, centered on secondary eclipse, for the shortened super-Earth group using the finalized catalog and false positive probabilities, excluding Kepler-10b. The binned data are shown as points. The error bars are the propagated photometric errors. The best fit curve is the solid black line. Overplotted are the reflected light plus thermal emission models for  $A_g = (2/3) * A_B = 0.0$  (blue), 0.1 (green), 0.3 (orange), and 0.6 (red), with the re-radiation factor  $f = 1/4$  (dashed) and  $2/3$  (solid). Lower panel: The distributions for the two parameters of the MCMC run, with the depths from the reflected light plus thermal emission from the upper panel plotted as vertical lines. The two fitted parameters are eclipse depth ( $2.6 \pm 1.1$  ppm) and continuum offset from zero ( $-0.02 \pm 0.50$  ppm).

the case of full heat redistribution, but a slightly (though not significantly) lower  $A_g = 0.02_{-0.08}^{+0.07}$  for the case of instantaneous re-radiation.

### 3.6.2 Mini-Neptunes

The average secondary eclipse for the Feb 2015 list of mini-Neptunes is shown in Figure 3.14. This group contains 38 candidates and 22,677 eclipses, with an average secondary eclipse depth of  $2.42 \pm 0.76$  ppm. The depth corresponds to  $A_g = 0.07 \pm 0.03$  for full heat redistribution. For instantaneous re-radiation, as with the super-Earths, I can only set an upper,  $3\sigma$  limit, but this limit is much lower,  $A_g < 0.04$ , than for the super-Earths. The shortened list consists of 28 candidates and 13,580 eclipses, with the result shown in Figure 3.15. The average secondary eclipse depth is  $1.69 \pm 0.85$  ppm, corresponding to  $A_g = 0.05 \pm 0.04$  for full heat redistribution. Again I can only set an upper,  $3\sigma$  limit of  $A_g < 0.07$  for instantaneous re-radiation.

### 3.6.3 Super-Neptunes

Figure 3.16 shows the result for the Feb 2015 group of super-Neptunes, which contains 16 candidates and 4,572 eclipses. The average secondary eclipse depth is  $2.16_{-1.38}^{+1.37}$  ppm. This depth corresponds to a geometric albedo  $A_g = 0.12 \pm 0.08$  for full heat redistribution and  $A_g = 0.09 \pm 0.08$  for instantaneous re-radiation. The shortened group contains 13 candidates and 3,574 eclipses, and the result is shown in Figure 3.17. The average secondary eclipse depth is  $1.99_{-1.38}^{+1.37}$  ppm, which

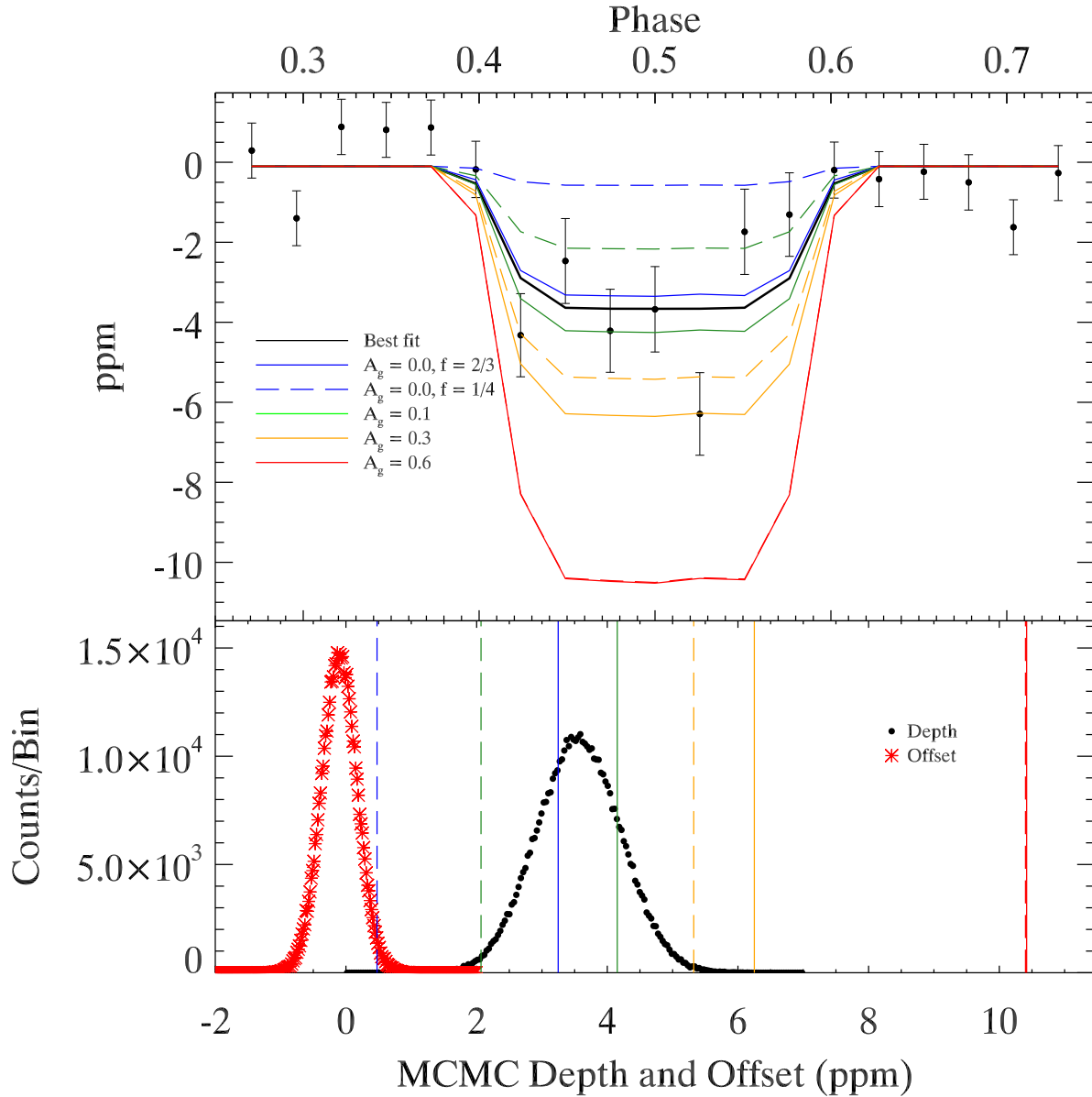


Figure 3.12 Upper panel: The averaged light curve, centered on secondary eclipse, for the super-Earth group with the Feb 2015 catalog, including Kepler-10b. The binned data are shown as points. The error bars are the propagated photometric errors. The best fit curve is the solid black line. Overplotted are the reflected light plus thermal emission models for  $A_g = (2/3) * A_B = 0.0$  (blue), 0.1 (green), 0.3 (orange), and 0.6 (red), with the re-radiation factor  $f = 1/4$  (dashed) and  $2/3$  (solid). Lower panel: The distributions for the two parameters of the MCMC run, with the depths from the reflected light plus thermal emission from the upper panel plotted as vertical lines. The two fitted parameters are eclipse depth ( $3.56 \pm 0.65$  ppm) and continuum offset from zero ( $-0.10 \pm 0.27$  ppm).

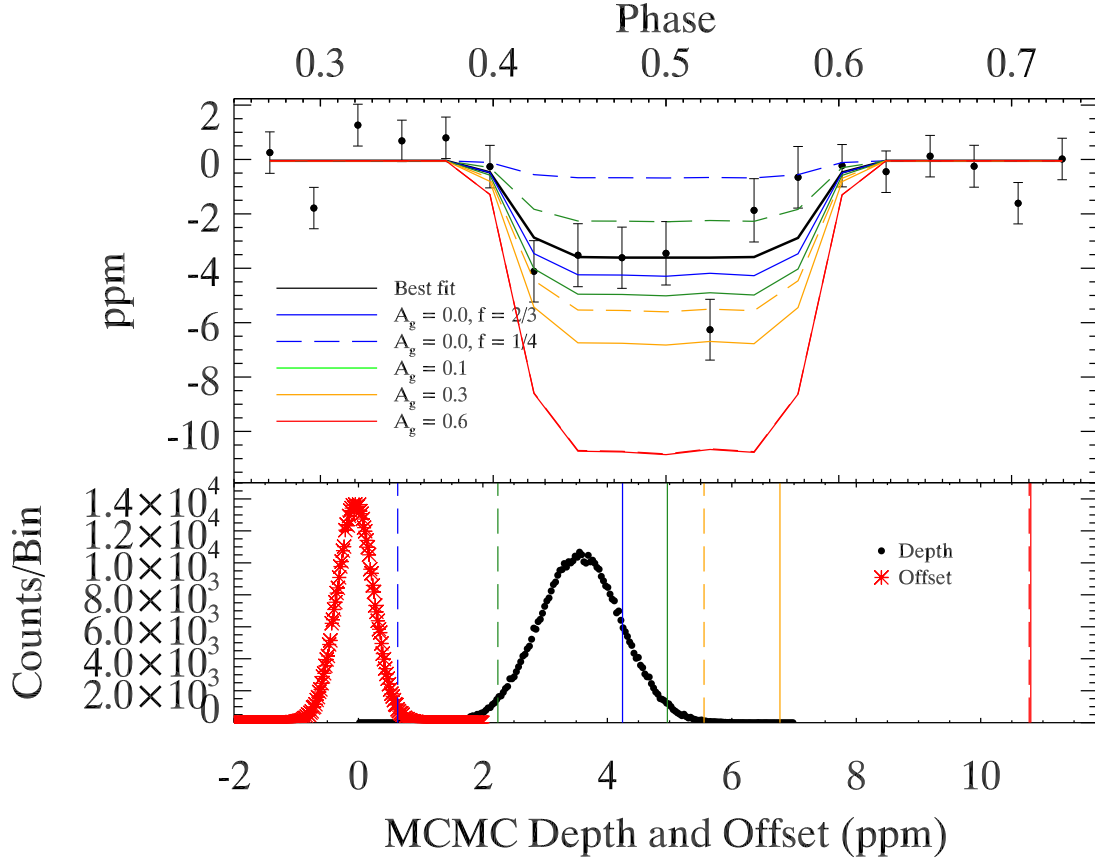


Figure 3.13 Upper panel: The averaged light curve, centered on secondary eclipse, for the shortened super-Earth group with the finalized catalog and false positive probabilities, including Kepler-10b. The binned data are shown as points. The error bars are the propagated photometric errors. The best fit curve is the solid black line. Overplotted are the reflected light plus thermal emission models for  $A_g = (2/3) * A_B = 0.0$  (blue), 0.1 (green), 0.3 (orange), and 0.6 (red), with the re-radiation factor  $f = 1/4$  (dashed) and  $2/3$  (solid). Lower panel: The distributions for the two parameters of the MCMC run, with the depths from the reflected light plus thermal emission from the upper panel plotted as vertical lines. The two fitted parameters are eclipse depth ( $3.56 \pm 0.67$  ppm) and continuum offset from zero ( $-0.05 \pm 0.29$  ppm).

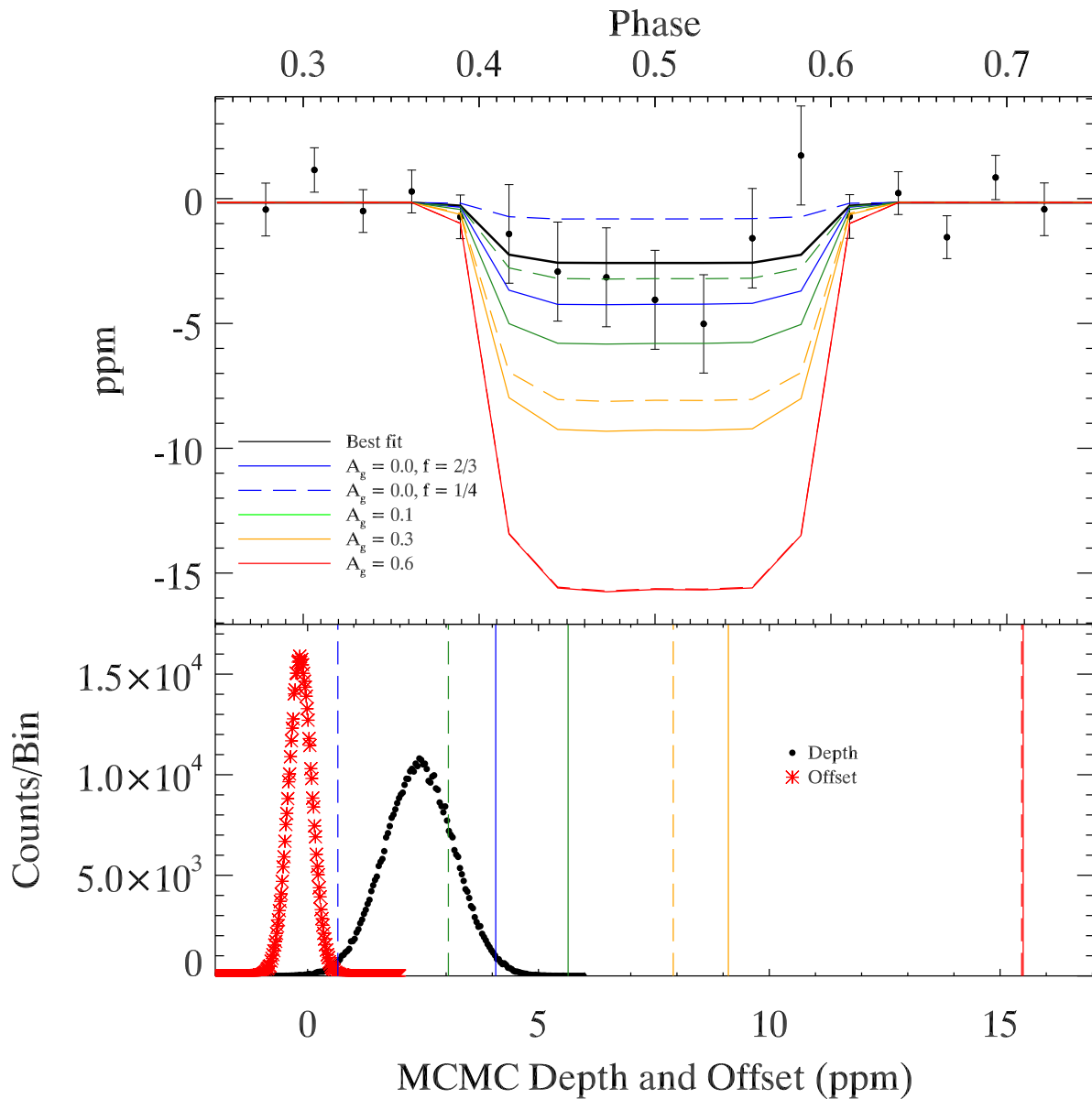


Figure 3.14 Upper panel: The averaged light curve, centered on secondary eclipse, for the mini-Neptune group with the Feb 2015 catalog. The binned data are shown as points. The error bars are the propagated photometric errors. The best fit curve is the solid black line. Overplotted are the reflected light plus thermal emission models for  $A_g = (2/3)A_B = 0.0$  (blue), 0.1 (green), 0.3 (orange), and 0.6 (red), with the re-radiation factor  $f = 1/4$  (dashed) and  $2/3$  (solid). Lower panel: The distributions for the two parameters of the MCMC run, with the depths from the reflected light plus thermal emission from the upper panel plotted as vertical lines. The two fitted parameters are eclipse depth ( $2.42 \pm 0.76$  ppm) and continuum offset from zero ( $-0.16 \pm 0.25$  ppm).

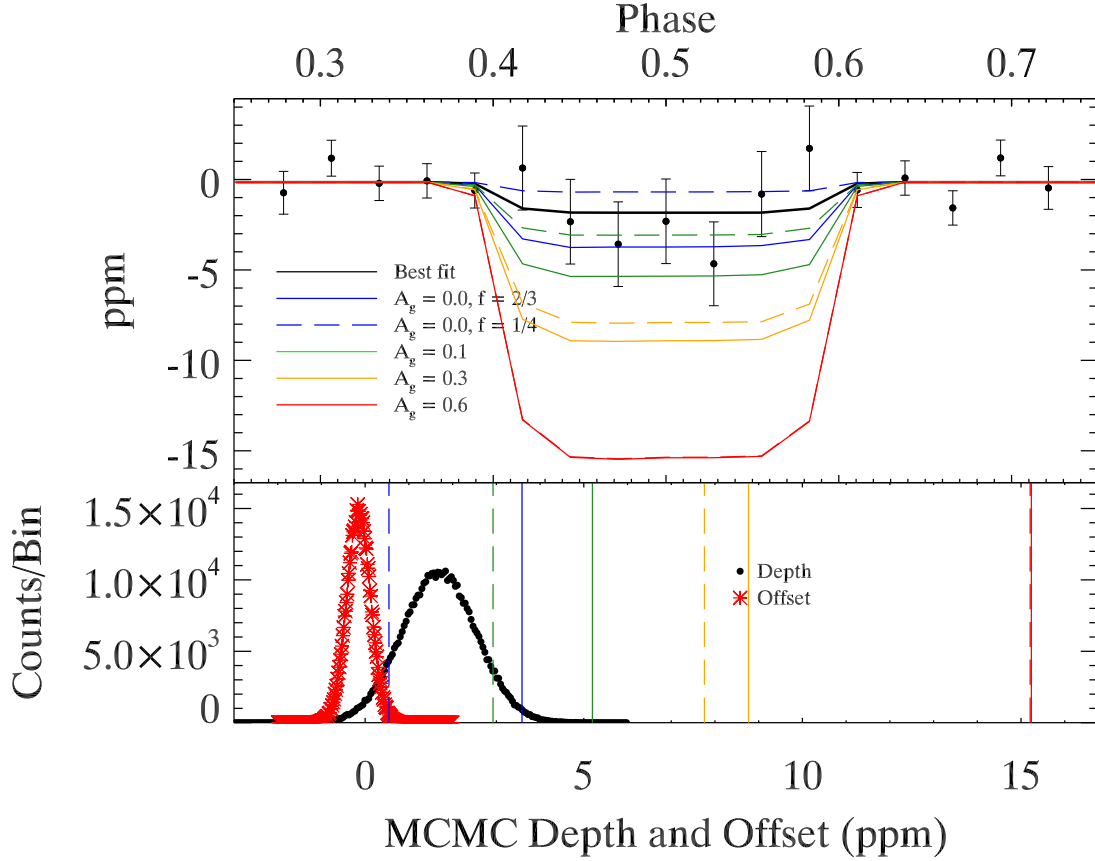


Figure 3.15 Upper panel: The averaged light curve, centered on secondary eclipse, for the shortened mini-Neptune group with the finalized catalog and false positive probabilities. The binned data are shown as points. The error bars are the propagated photometric errors. The best fit curve is the solid black line. Overplotted are the reflected light plus thermal emission models for  $A_g = (2/3) * A_B = 0.0$  (blue), 0.1 (green), 0.3 (orange), and 0.6 (red), with the re-radiation factor  $f = 1/4$  (dashed) and  $2/3$  (solid). Lower panel: The distributions for the two parameters of the MCMC run, with the depths from the reflected light plus thermal emission from the upper panel plotted as vertical lines. The two fitted parameters are eclipse depth ( $1.69 \pm 0.85$  ppm) and continuum offset from zero ( $-0.15 \pm 0.27$  ppm).

corresponds to  $A_g = 0.11 \pm 0.08$  for full redistribution of heat and  $A_g = 0.09 \pm 0.09$  for instantaneous re-radiation.

### 3.6.4 Comparison to Short Cadence

To compare my results in this chapter with those of Chapter 2, I also take the average of the three radius bins combined, matching the 1-6  $R_\oplus$  radius bin of the earlier work. Figure 3.18 shows the result for the Feb 2015 group of 1-6  $R_\oplus$  candidates, excluding Kepler-10b. There are 109 candidates for a total of 106,927 eclipses. The average eclipse depth is  $2.50 \pm 0.62$  ppm, for  $A_g = 0.10 \pm 0.03$  for full heat redistribution, and  $A_g < 0.07$  for instantaneous re-radiation. The shortened group result, shown in Figure 3.19, is similar, with a depth of  $2.36 \pm 0.71$  ppm, corresponding to  $A_g = 0.09 \pm 0.04$  for full redistribution of heat, and  $A_g < 0.08$  for instantaneous re-radiation. The shortened group contains 80 candidates, with 67,959 eclipses. Including Kepler-10b with the Feb 2015 group, shown in Figure 3.20, brings the average eclipse depth to  $3.26 \pm 0.48$  ppm, corresponding to  $A_g = 0.16 \pm 0.03$  for full heat redistribution, and to  $A_g = 0.01 \pm 0.04$  for instantaneous re-radiation. For the shortened group, shown in Figure 3.21, adding Kepler-10b brings the average eclipse depth to  $3.09 \pm 0.50$  ppm. This gives  $A_g = 0.15 \pm 0.03$  for full heat redistribution, and  $A_g = 0.00 \pm 0.05$  for instantaneous re-radiation.

For the short cadence data, excluding Kepler-10b, I found  $A_g = 0.22 \pm 0.06$ , when only considering reflected light, and the inclusion of thermal emission changed the albedo by less than the uncertainty. The albedos found from the long cadence

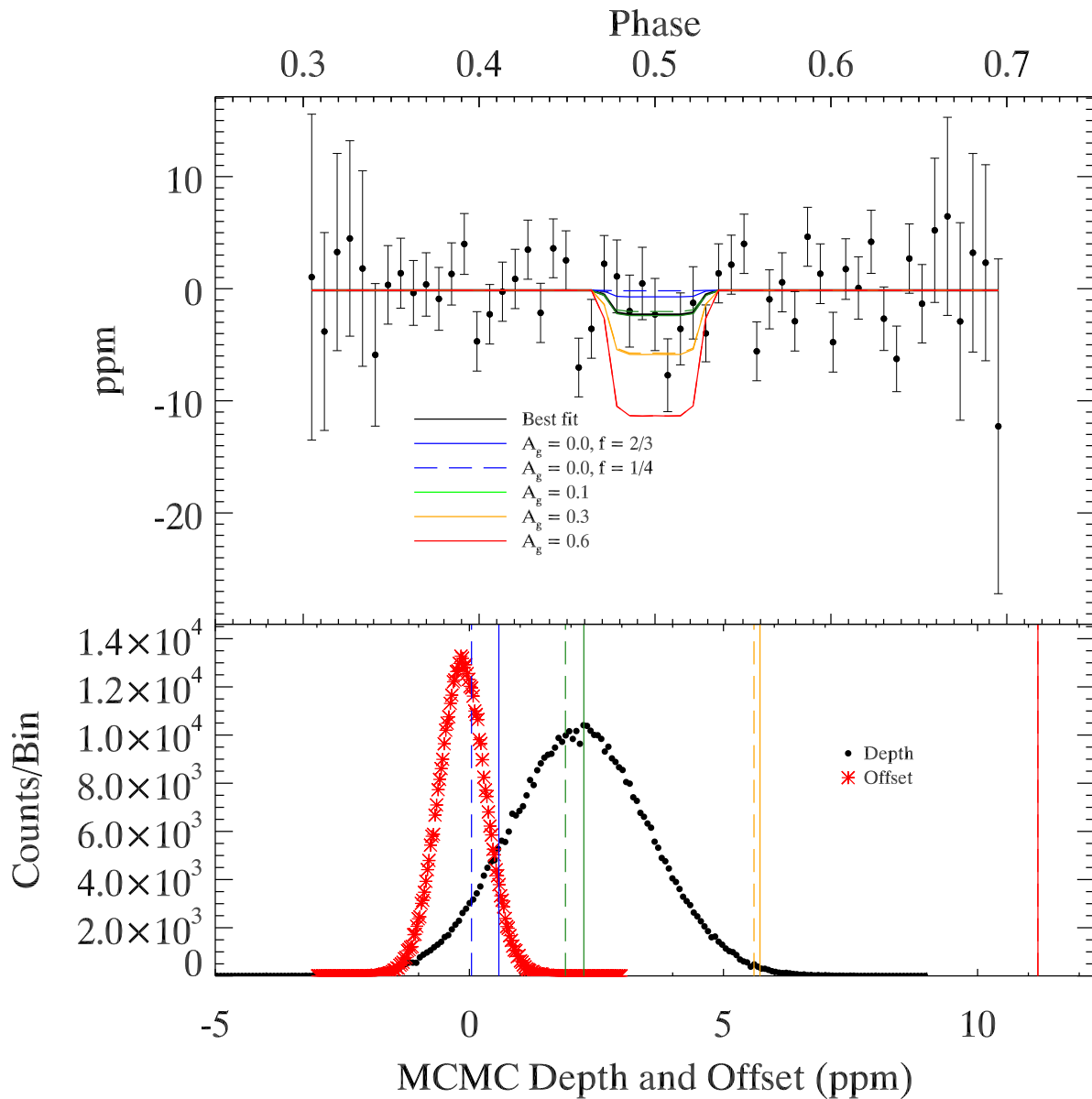


Figure 3.16 Upper panel: The averaged light curve, centered on secondary eclipse, for the super-Neptune group with the Feb 2015 catalog. The binned data are shown as points. The error bars are the propagated photometric errors. The best fit curve is the solid black line. Overplotted are the reflected light plus thermal emission models for  $A_g = (2/3)A_B = 0.0$  (blue), 0.1 (green), 0.3 (orange), and 0.6 (red), with the re-radiation factor  $f = 1/4$  (dashed) and  $2/3$  (solid). Lower panel: The distributions for the two parameters of the MCMC run, with the depths from the reflected light plus thermal emission from the upper panel plotted as vertical lines. The two fitted parameters are eclipse depth ( $2.16 \pm 1.38$  ppm) and continuum offset from zero ( $-0.14 \pm 0.46$  ppm).

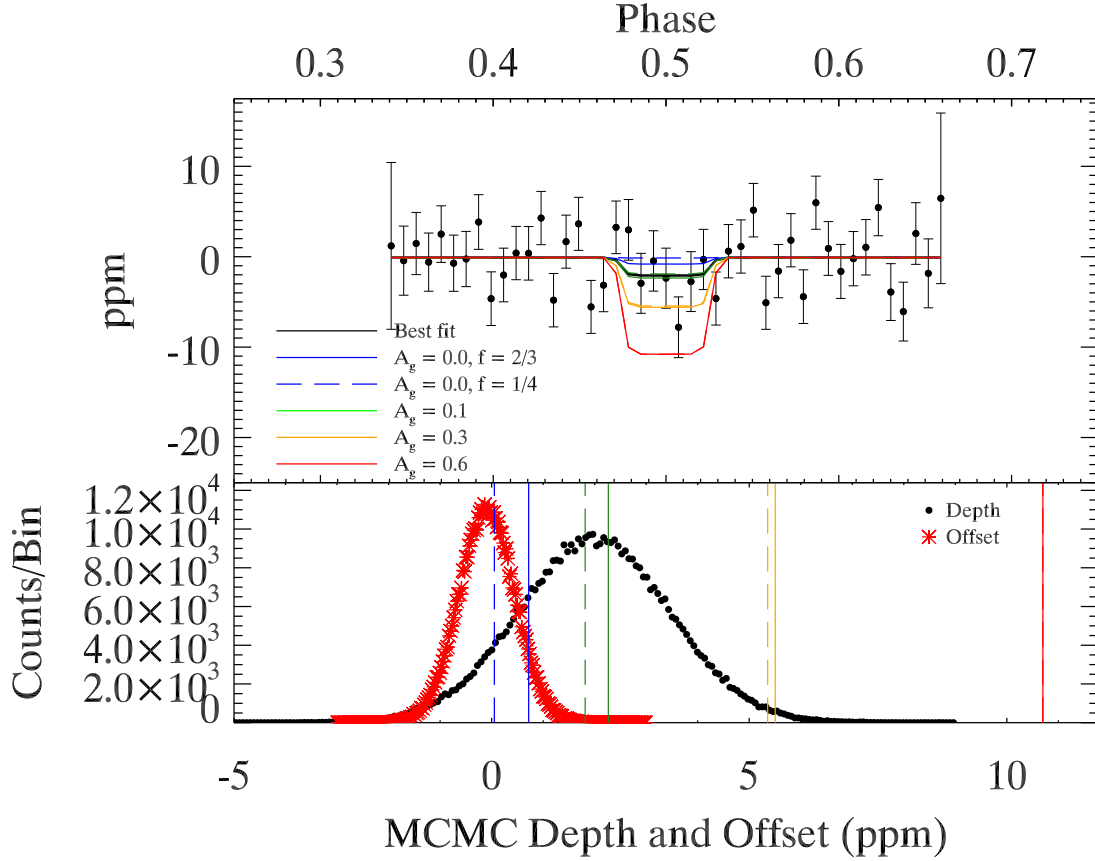


Figure 3.17 Upper panel: The averaged light curve, centered on secondary eclipse, for the shortened super-Neptune group with the finalized catalog and false positive probabilities. The binned data are shown as points. The error bars are the propagated photometric errors. The best fit curve is the solid black line. Overplotted are the reflected light plus thermal emission models for  $A_g = (2/3) * A_B = 0.0$  (blue), 0.1 (green), 0.3 (orange), and 0.6 (red), with the re-radiation factor  $f = 1/4$  (dashed) and  $2/3$  (solid). Lower panel: The distributions for the two parameters of the MCMC run, with the depths from the reflected light plus thermal emission from the upper panel plotted as vertical lines. The two fitted parameters are eclipse depth ( $1.99 \pm 1.47$  ppm) and continuum offset from zero ( $-0.09 \pm 0.54$  ppm).

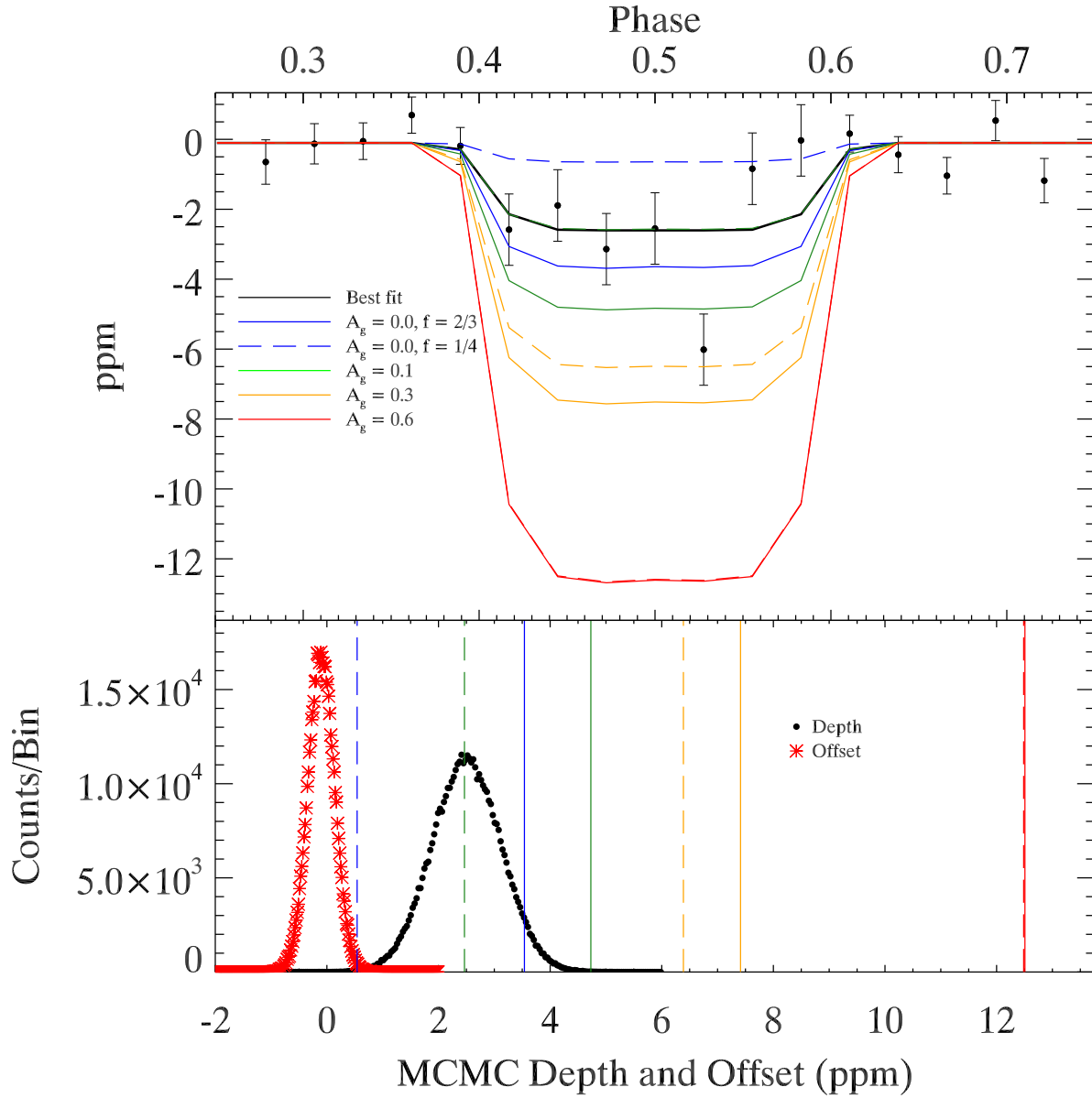


Figure 3.18 Upper panel: The averaged light curve, centered on secondary eclipse, for the 1 to 6  $R_{\oplus}$  group with the Feb 2015 catalog, excluding Kepler-10b. The binned data are shown as points. The error bars are the propagated photometric errors. The best fit curve is the solid black line. Overplotted are the reflected light plus thermal emission models for  $A_g = (2/3) * A_B = 0.0$  (blue), 0.1 (green), 0.3 (orange), and 0.6 (red), with the re-radiation factor  $f = 1/4$  (dashed) and  $2/3$  (solid). Lower panel: The distributions for the two parameters of the MCMC run, with the depths from the reflected light plus thermal emission from the upper panel plotted as vertical lines. The two fitted parameters are eclipse depth ( $2.50 \pm 0.62$  ppm) and continuum offset from zero ( $-0.10 \pm 0.24$  ppm).

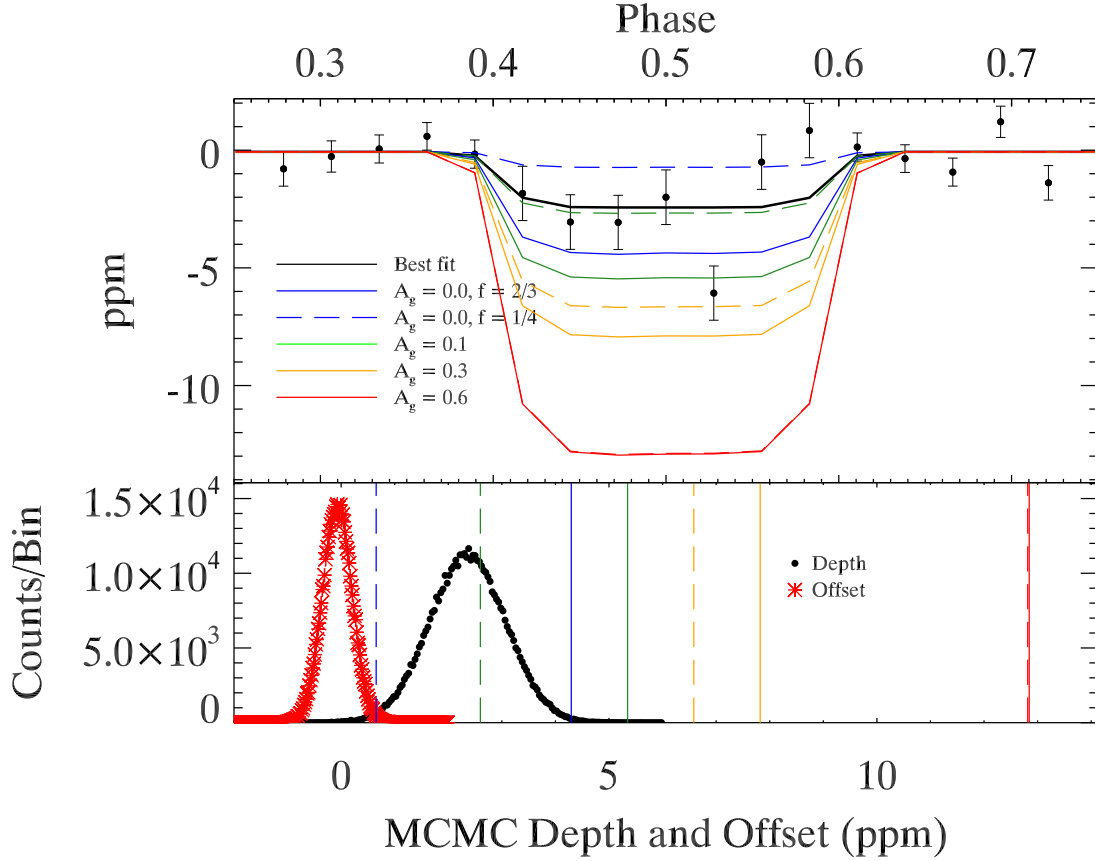


Figure 3.19 Upper panel: The averaged light curve, centered on secondary eclipse, for the shortened 1 to 6  $R_{\oplus}$  group with the finalized catalog and false positive probabilities, excluding Kepler-10b. The binned data are shown as points. The error bars are the propagated photometric errors. The best fit curve is the solid black line. Overplotted are the reflected light plus thermal emission models for  $A_g = (2/3) * A_B = 0.0$  (blue), 0.1 (green), 0.3 (orange), and 0.6 (red), with the re-radiation factor  $f = 1/4$  (dashed) and  $2/3$  (solid). Lower panel: The distributions for the two parameters of the MCMC run, with the depths from the reflected light plus thermal emission from the upper panel plotted as vertical lines. The two fitted parameters are eclipse depth ( $2.36 \pm 0.71$  ppm) and continuum offset from zero ( $-0.07 \pm 0.28$  ppm).

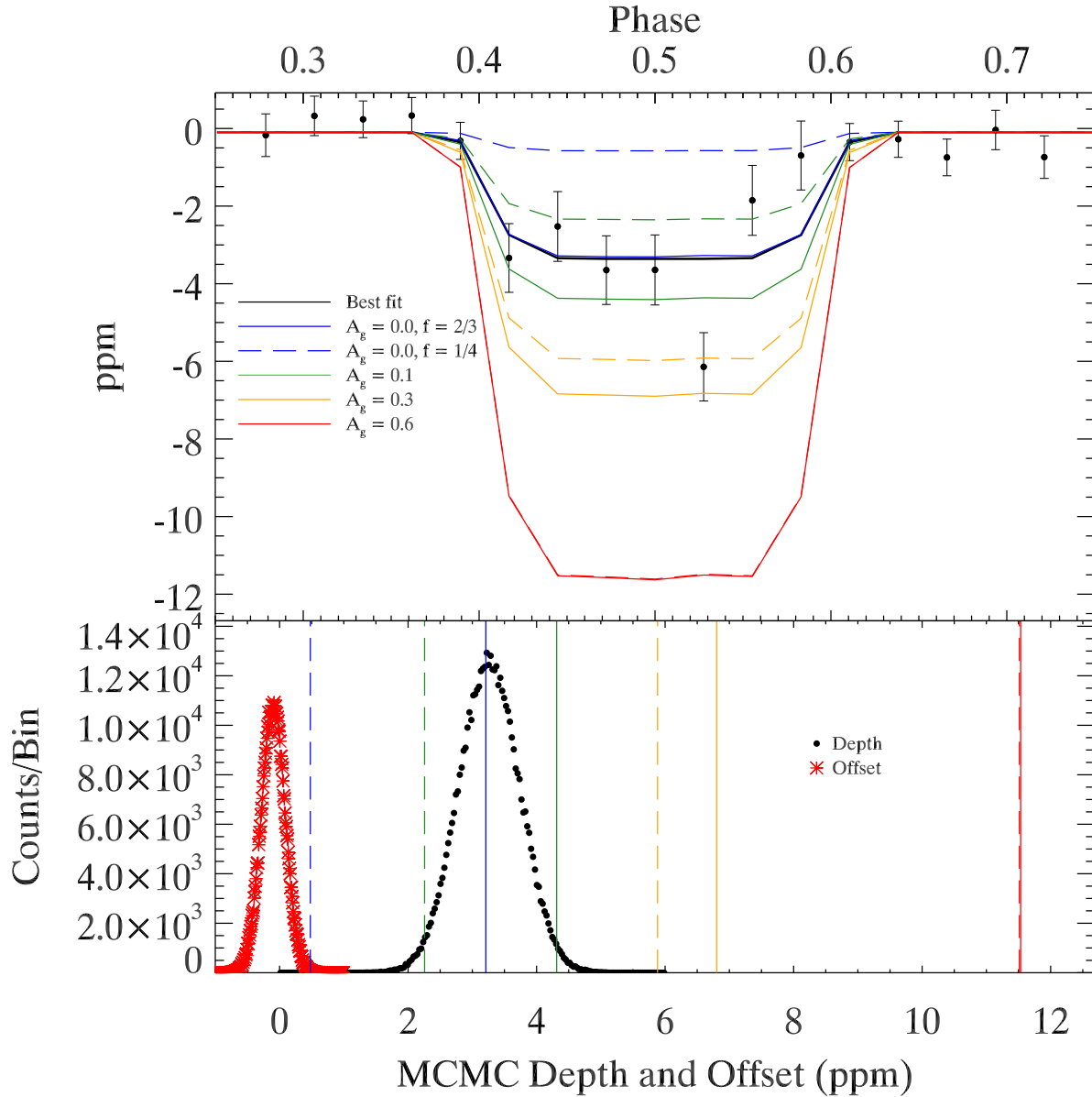


Figure 3.20 Upper panel: The averaged light curve, centered on secondary eclipse, for the 1 to 6  $R_{\oplus}$  group for the Feb 2015 catalog, including Kepler-10b. The binned data are shown as points. The error bars are the propagated photometric errors. The best fit curve is the solid black line. Overplotted are the reflected light plus thermal emission models for  $A_g = (2/3) * A_B = 0.0$  (blue), 0.1 (green), 0.3 (orange), and 0.6 (red), with the re-radiation factor  $f = 1/4$  (dashed) and  $2/3$  (solid). Lower panel: The distributions for the two parameters of the MCMC run, with the depths from the reflected light plus thermal emission from the upper panel plotted as vertical lines. The two fitted parameters are eclipse depth ( $3.26 \pm 0.48$  ppm) and continuum offset from zero ( $-0.10 \pm 0.18$  ppm).

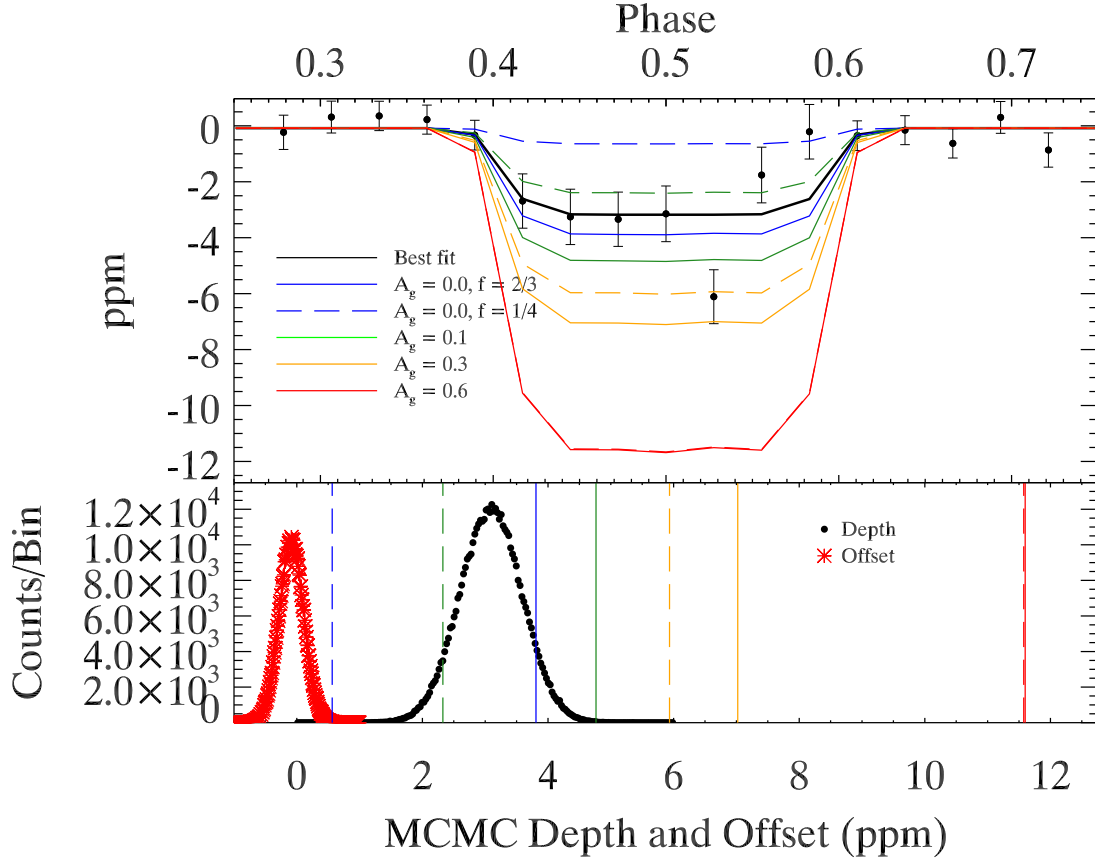


Figure 3.21 Upper panel: The averaged light curve, centered on secondary eclipse, for the shortened 1 to 6  $R_{\oplus}$  group for the finalized catalog and false positive probabilities, including Kepler-10b. The binned data are shown as points. The error bars are the propagated photometric errors. The best fit curve is the solid black line. Overplotted are the reflected light plus thermal emission models for  $A_g = (2/3) * A_B = 0.0$  (blue), 0.1 (green), 0.3 (orange), and 0.6 (red), with the re-radiation factor  $f = 1/4$  (dashed) and  $2/3$  (solid). Lower panel: The distributions for the two parameters of the MCMC run, with the depths from the reflected light plus thermal emission from the upper panel plotted as vertical lines. The two fitted parameters are eclipse depth ( $3.09 \pm 0.50$  ppm) and continuum offset from zero ( $-0.08 \pm 0.20$  ppm).

data using the Feb 2015 groups are plotted versus the average group radius in Figure 3.22, along with the short cadence results. Including Kepler-10b in the short cadence raised the albedo to  $A_g = 0.37 \pm 0.05$ . While the albedos found in this chapter are lower than those I found for the short cadence data, excluding Kepler-10b, the difference is only  $0.12 \pm 0.07$ , and so is consistent within  $2\sigma$ . A possible explanation for the lower albedos found here is the greater number of candidates included. The short cadence analysis only had 31 candidates, plus Kepler-10b, so if any of those candidates are part of the higher-albedo population of candidates like Kepler-10b, it would more strongly influence the mean. Also note that, in Figure 3.22, the  $1-6 R_{\oplus}$  long cadence group, including Kepler-10b, contains the most data and therefore shows greater separation between the  $f = 1/4$  and  $f = 2/3$  thermal models.

There are also eight candidates in my short cadence list that now, with updates to their parameters since publication of Chapter 2, have radii between 6 and 8  $R_{\oplus}$  (KOIs 356.01 and 1784.01), or have  $(R_p/a)^2 < 10$  ppm (KOIs 5.01, 299.01, 505.03, 755.01, 1128.01, and 1805.01). One might expect removing the latter six candidates from the long cadence sample to increase the average albedo, rather than lower it, since their maximum eclipse depths would be smaller than expected and thus appear to have a lower albedo. The albedo does not increase, so perhaps some of these are part of the higher-albedo population or are false positives. One short cadence candidate, KOI 2678.01, was eliminated from the long cadence group due to a high failure rate of the tests in Section 3.3.1, while another, KOI 2700.01, was not included in the long cadence because of its revised impact parameter.

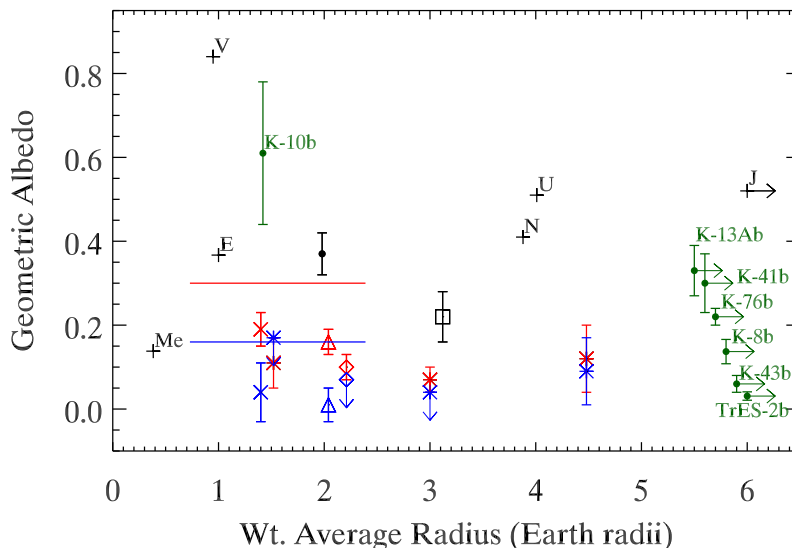


Figure 3.22 The geometric albedo is plotted versus the weighted average radius for the long cadence data for the super-Earth (excluding Kepler-10b), mini-Neptune, and super-Neptune groups with an asterisk (\*), for the super-Earth group including Kepler-10b with an x, for the 1 to 6  $R_{\oplus}$  group without Kepler-10b with a diamond, and for the 1 to 6  $R_{\oplus}$  group with Kepler-10b with a triangle. Points in red assume a redistribution factor  $f = 1/4$ , while points in blue assume a redistribution factor of  $f = 2/3$ . Also shown in black are the short cadence results for the 1 to 6  $R_{\oplus}$  without Kepler-10b (square) and with Kepler-10b (dot). The error bars show the  $1\sigma$  uncertainty on the albedo. Points with down arrows instead of error bars (for  $f = 2/3$ : the super-Earths without Kepler-10b, the mini-Neptunes, and 1 to 6  $R_{\oplus}$  without Kepler-10b) represent  $3\sigma$  upper limits. The radius range and median albedo for the super-Earths in [Demory \(2014\)](#) are shown as the solid red ( $f = 1/4$ ) and solid blue ( $f = 2/3$ ) lines. Also included are solar system planets with a black + (Me = Mercury, V = Venus, E = Earth, J = Jupiter, U = Uranus, and N = Neptune). Radii for the solar system are taken from [Table 1.1](#), while the albedos are from [Traub & Oppenheimer \(2010\)](#). Plotted with green points is a representative sample of the bright and dark hot Jupiters and Kepler-10b from [Table 1.1](#). Right arrows indicate that the true radius is larger than plotted. Jupiter and the hot Jupiters are plotted near a radius of 6 to fit within the plot.

### 3.6.5 Comparison to [Demory \(2014\)](#)

The study of 27 long cadence super-Earths by [Demory \(2014\)](#) finds a median geometric albedo  $A_g = 0.30$  after thermal decontamination, assuming a null Bond albedo ( $A_B$ ) and efficient heat redistribution, and a median  $A_g = 0.16$  after thermal decontamination, assuming  $A_B = 0$  and no redistribution of heat. While I adopt  $A_B = (3/2)A_g$  rather than  $A_B = 0$  for thermal removal, this cannot explain my lower mean albedos. Adopting non-zero Bond albedos means that my equilibrium temperatures overall are lower, therefore weakening the thermal contribution and requiring a higher albedo for a given eclipse depth. I instead look to several differences in the candidate sample selection to explain my lower albedos. Only two candidates in my long cadence sample overlap with the sample of [Demory \(2014\)](#). Kepler-10b is one of the candidates, and the other is KOI 1169.01, which now has a high false positive probability from [Morton et al. \(2016\)](#). My long cadence sample is larger, with 56 candidates including Kepler-10b, or 40 for the shortened group with Kepler-10b, and it is comprised of candidates with fainter host stars and larger  $(R_p/a)^2$  values. As with the comparison between my short cadence and my long cadence results, the larger sample size could be a factor, since the error in the mean should decrease with a larger sample size. Furthermore, the selection cut of [Demory \(2014\)](#) based on a total albedo uncertainty of less than 1.0 may be preferentially selecting high-albedo candidates from the lower signal-to-noise stars.

### 3.6.6 Biases in the Albedo Due to Averaging

The average albedo is slightly biased toward the objects in the group with larger  $(R_p/a)^2$ . Since I do not know the underlying albedo distribution, I tested the bias by randomly assigning each candidate an albedo  $A_g$ , uniformly distributed between 0 and 0.6. I calculated the depth of an eclipse the assigned albedo would produce, using  $A_g * (R_p/a)^2$  and took a weighted average of the depth and of  $(R_p/a)^2$ . The weights for the average are determined as a sum for each object of its weight in each phase bin times the weight of the phase bin in the overall fit of the model curve to the binned data. To mimic how I obtain an average albedo from my average eclipse depth, I divide the weighted average depth by the weighted average  $(R_p/a)^2$ . I then take a weighted average of the assigned albedos. I repeat this process 100,000 times. The mean fractional difference between the calculated average albedo and the average assigned albedo for the super-Earth group (excluding Kepler-10b) is less than 1%, and at worst is 27%. This is less than the error bar on my actual calculated albedo for the group, so it does not significantly affect the result.

Similarly, the average albedo is slightly biased by objects with larger albedo. I assigned a random albedo to each object in the group, uniformly distributed between 0 and 0.6. I calculated model eclipses for all the data points, including thermal and reflected light, for the assigned albedos. I then applied my method for determining the average albedo to the model eclipses. I performed these calculations 100 times for each group, for each of the 2 values for heat redistribution. I compared the results to the weighted average of the known albedos. I found that for  $f = 1/4$ , the

determined average varied from the known average by  $-1_{-10}^{+13}\%$  for the 1-2  $R_{\oplus}$  group (excluding Kepler-10b) and by  $-1_{-8}^{+10}\%$  for the 2-4  $R_{\oplus}$  group, where the error bars define the central 68% of the trials. For  $f = 2/3$ , the determined average varied from the known average by  $-4_{-7}^{+5}\%$  for the 1-2  $R_{\oplus}$  group (excluding Kepler-10b) and by  $-4_{-10}^{+11}\%$  for the 2-4  $R_{\oplus}$  group. I conclude that this source of bias is not significant to my analysis.

### 3.6.7 Implications of the Low Albedos

The super-Earths in my sample are sufficiently hot that they likely have, at most, a tenuous atmosphere dominated by vaporized sodium (e.g. [Castan & Menou, 2011](#); [Kite et al., 2016](#); [Miguel et al., 2011](#); [Schaefer & Fegley, 2009](#)). I may in some cases be seeing bare surfaces. While I have determined that super-Earths, on average, appear to have low albedos, there is a subset of higher-albedo planets ([Demory, 2014](#)), including Kepler-10b ([Batalha et al., 2011](#)), which appear to be bright. The low-albedo hot super-Earths likely have no clouds present, and the measured albedo is of the surface. Three potential scenarios could explain the subset of higher albedos: embedded higher-albedo particulates in a lava ocean surface, clouds, and thermal inversions. The lava ocean scenario proposed by [Léger et al. \(2011\)](#) for CoRoT-7b would have a Bond albedo less than 0.1 if made mostly of pure  $\text{Al}_2\text{O}_3$ , but [Rouan et al. \(2011\)](#) propose that solid particles of  $\text{ThO}_2$  floating in the lava ocean, depending on particle size, could produce an overall Bond albedo for the lava ocean of nearly 0.50, which could help to explain the unusual brightness of Kepler-10b.

Alternatively, under certain conditions, the tenuous sodium atmospheres could support the formation of silicate clouds (e.g. [Castan & Menou, 2011](#); [Miguel et al., 2011](#); [Schaefer & Fegley, 2009](#)), which would have higher albedos. Cloud properties and coverage would depend on many factors, including composition, particle size, and winds, which would explain the existence of the bright and dark populations in similar temperature regimes. Silicates in the atmosphere could also absorb UV and visible light and lead to a thermal inversion ([Ito et al., 2015](#)), producing emission lines that would then make the secondary eclipse deeper than expected from just the combination of reflected light and thermal emission at the equilibrium temperature.

The mini-Neptunes and super-Neptunes should have substantial atmospheres. Hot Jupiters were expected to show a range of albedos depending on temperature ([Sudarsky et al., 2000](#)), depending on the type of clouds that could form and their location in the atmosphere. Kepler-7b and Kepler-12b are good examples of the complex nature of cloud formation and properties. Despite both planets receiving similar amounts of light from their stars, Kepler-7b is relatively bright, with  $A_g \approx 0.35$  and shows evidence for cloud coverage that varies with longitude; Meanwhile, Kepler-12b is dark, with  $A_g = 0.08$ , and shows no evidence for longitudinal variation ([Heng & Demory, 2013](#), and references therein).

The consistency of the average albedo across the three size groups considered here, as well as with the hot Jupiters studied in the literature, suggests that most of these hot planets have minimal or no cloud coverage. The known outliers in albedo, however, demonstrate the complex and important role of cloud formation.

### 3.7 Chapter 3 Summary

I apply the averaging technique used in [Sheets & Deming \(2014\)](#) to long cadence *Kepler* data, for three radius groups: 1-2  $R_{\oplus}$ , 2-4  $R_{\oplus}$ , and 4-6  $R_{\oplus}$ . I find that all three groups are similarly dark, with average geometric albedos of  $0.11 \pm 0.06$ ,  $0.05 \pm 0.04$ , and  $0.11 \pm 0.08$ , respectively, if heat is completely redistributed. In the case of instantaneous re-radiation, there is a larger thermal contribution to the eclipse depths, making the geometric albedo even lower. The albedo results are summarized in [Table 3.3](#). These average albedos are slightly lower than the average albedo I found using short cadence data, and are similar to some of the dark hot Jupiters. As with bright hot Jupiters like Kepler-7b, there are outliers at higher albedo for super-Earths, too. The simplest solution therefore is that a similar mechanism may be at work to create the outliers across the range in radius. Such a mechanism may be silicate clouds, which are postulated for high temperature atmospheres across a wide range of pressures ([Helling et al., 2016](#)). Given the low average albedo, though, these clouds must be somewhat uncommon.

Table 3.3. Albedo Results

Candidate Group	# of Candidates	total # of eclipses	Eclipse Depth (ppm)	$A_g$ (f = 1/4)	$A_g$ (f = 2/3)
Super-Earths					
Feb 2015 w/o Kepler-10b	55	79,678	$2.44 \pm 0.99$	$0.11 \pm 0.06$	$< 0.17^a$
Shortened, w/o Kepler-10b	39	50,805	$2.63^{+1.13}_{-1.14}$	$0.11 \pm 0.06$	$< 0.17^a$
Feb 2015 w/ Kepler-10b	56	80,492	$3.56 \pm 0.65$	$0.19 \pm 0.04$	$0.04 \pm 0.07$
Shortened, w/ Kepler-10b	40	51,597	$3.56 \pm 0.67$	$0.19 \pm 0.04$	$0.02^{+0.07}_{-0.08}$
Mini-Neptunes					
Feb 2015	38	22,677	$2.42 \pm 0.76$	$0.07 \pm 0.03$	$< 0.04^a$
Shortened	28	13,580	$1.69 \pm 0.85$	$0.05 \pm 0.04$	$< 0.07^a$
Super-Neptunes					
Feb 2015	16	4,572	$2.16^{+1.37}_{-1.38}$	$0.12 \pm 0.08$	$0.09 \pm 0.08$
Shortened	13	3,574	$1.99^{+1.37}_{-1.38}$	$0.11 \pm 0.08$	$0.09 \pm 0.09$

<sup>a</sup> $3\sigma$  upper limit.

## Chapter 4: Refraction and Future Work

### 4.1 Background

Refraction of light through a planet's atmosphere depends on the scale height of the atmosphere. As with transmission spectroscopy, the refraction effect is stronger in large-scale-height atmospheres, and thus in low-mean-molecular-weight atmospheres. The scale height  $H$  of the atmosphere is given by

$$H = \frac{k_B T}{\mu g} \quad (4.1)$$

where  $k_B$  is the Boltzmann constant,  $T$  is the temperature of the planet's atmosphere,  $\mu$  is the mean molecular weight of the atmosphere, and  $g$  is the planet's surface gravity. For any given group of planets, detecting strong refraction suggests atmospheres which are typically cloud-free and H<sub>2</sub>-rich, while detecting weak or no refraction suggests the hazy or high mean molecular weight models. The refraction effect is most obvious in the light curve just before first contact and just after last contact, creating shoulders on the transit, above the continuum flux level.

Early work by [Hui & Seager \(2002\)](#) modeled the effect of refraction on the shape of the transit of extrasolar planets, building on a technique used to probe the atmospheres of planets in our own solar system as they occult other stars (e.g.

Elliot & Olkin, 1996, and references therein). The authors concluded that, when the viewing geometry and atmospheric parameters are right to produce refraction, additional flux is removed from the light curve during transit, and the effect is strongly wavelength-dependent due to Rayleigh scattering and atmospheric absorption lines.

Sidis & Sari (2010) then modeled the refraction of light through the atmosphere of a transparent planet, during and just outside of transit, without and with Rayleigh scattering in the atmosphere included. Refraction produces an illuminated crescent within the atmosphere of the planet outside of transit, which is an image of the host star. This illuminated crescent adds to the total light in the light curve near transit. The light curve produced by the Sidis & Sari (2010) model without scattering, shown in Figure 4.1, looks quite like the light curve produced for opaque planets with the same parameters, with the overall depth of the transit reaching the expected  $(R_p/R_*)^2$ . There are two slight differences, however. First, the modest brightening just before and just after transit produced by refraction is apparent in the light curve as small shoulders just outside first and last contact ( $X = 1 + (R_p/R_*)$  and  $X = -1 - (R_p/R_*)$ , where  $X$  is the projected distance on the sky of the center of the planet from the center of the star, in units of stellar radius). Second, the bottom of the transit is slightly rounded. This rounding mimics the rounding of the transit seen in opaque planet transits due to limb-darkening of the star, but here it is due only to refraction. The Sidis & Sari (2010) model does not take into account limb-darkening.

Refracted light has been seen during the transits of Venus. Pasachoff et al. (2011) presented images of the 2004 transit taken with NASA's *Transition Region*

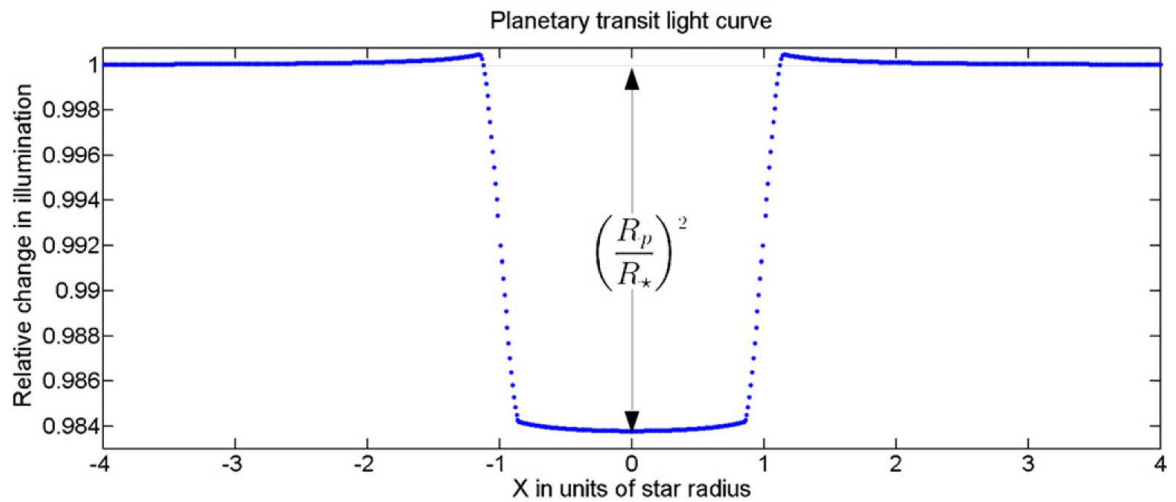


Figure 4.1 Figure 4 from [Sidis & Sari \(2010\)](#), which shows the light curve for a star and a transiting transparent planet, including refraction by the planet's atmosphere and excluding stellar limb-darkening. The X coordinate is the distance between the planet center and star center, projected on the sky, in units of stellar radius. The parameters for the system here are somewhat non-realistic, to exaggerate the refraction effect to make it visible.

And *Coronal Explorer*, or *TRACE*, satellite, and [Tanga et al. \(2012\)](#) developed the first framework to analyze and measure the refraction effect in these images as well as in ground-based imaging. [Tanga et al. \(2012\)](#) also developed a model of the refraction to determine how the cloud-top altitude and scale height of the atmosphere vary with latitude. [García Muñoz & Mills \(2012\)](#) also included refraction in their modeling of the interaction of sunlight with the atmosphere of Venus in preparation for observations of the 2012 Venus transit. While the images and analysis of [Pasachoff et al. \(2011\)](#) and [Tanga et al. \(2012\)](#) focused on ingress and egress, [García Muñoz & Mills \(2012\)](#) developed the model further to include out-of-transit and in-transit predictions as well.

Refraction also limits the altitude to which a super-Earth atmosphere can be probed during transit by transmission spectroscopy. [García Muñoz et al. \(2012\)](#) further investigated the effects of refraction on transmission spectra by modeling lunar eclipse spectra, since the illumination of the Moon during umbral eclipse is due to sunlight that has refracted through Earth's atmosphere. The authors found that the Earth's radius, if measured in transit from outside the solar system, varies by about 12 km over the course of the transit due to refraction effects, and that the lowest 12 to 14 km of the Earth's atmosphere cannot be probed by transmission spectroscopy at mid-transit due to refraction. [Misra et al. \(2014\)](#) and [Bétrémieux & Kaltenegger \(2014\)](#) also modeled the effects of refraction on transmission spectra and pointed out that in general, Earth-like planets in the habitable zone around Sun-like stars can only be probed to very low pressures, around 0.3 bar, at mid-transit, because rays from the star passing lower in the atmosphere are bent out of the line of sight to the

observer (see Figure 4.2). Both studies also concluded that Earth-like planets in the habitable zones of the coolest stars could be probed to much higher pressures, nearly 1 bar. The refraction effect just outside of transit, however, can probe these higher pressures for the habitable zones around Sun-like stars (Misra et al., 2014). Thus, looking for refracted light in spectra when the planet is just outside of transit may be the only way to properly determine the compositions of these types of planets.

Lastly, as Misra & Meadows (2014) point out, using a broad bandpass measurement of refracted light just outside of transit offers a relatively fast way of determining whether an individual candidate is a good target for transmission spectroscopy. While *Kepler* candidates are for the most part orbiting stars too faint for spectroscopic follow-up, upcoming missions such as TESS (Ricker et al., 2015) and PLATO (Rauer et al., 2014) will find candidates around brighter stars. A broad bandpass measurement of refraction outside of transit can be acquired with much less telescope time than required for a transmission spectrum, thus preventing a significant investment only to determine that the transmission spectrum cannot be measured due to clouds or haze.

Refracted light is therefore a useful tool to develop for the study of exoplanet atmospheres. Sidis & Sari (2010) provide analytic approximations to their numerical models for two regimes: near transit and far from transit. They also provide expressions to modify the refraction effect for basic Rayleigh scattering in the planet's atmosphere. The predicted effect of the refraction for Super-Earths is a peak brightening of 10 to 140 ppm just outside transit, assuming a predominantly molecular hydrogen composition and a density comparable to that of GJ 1214b. Tanga et al.

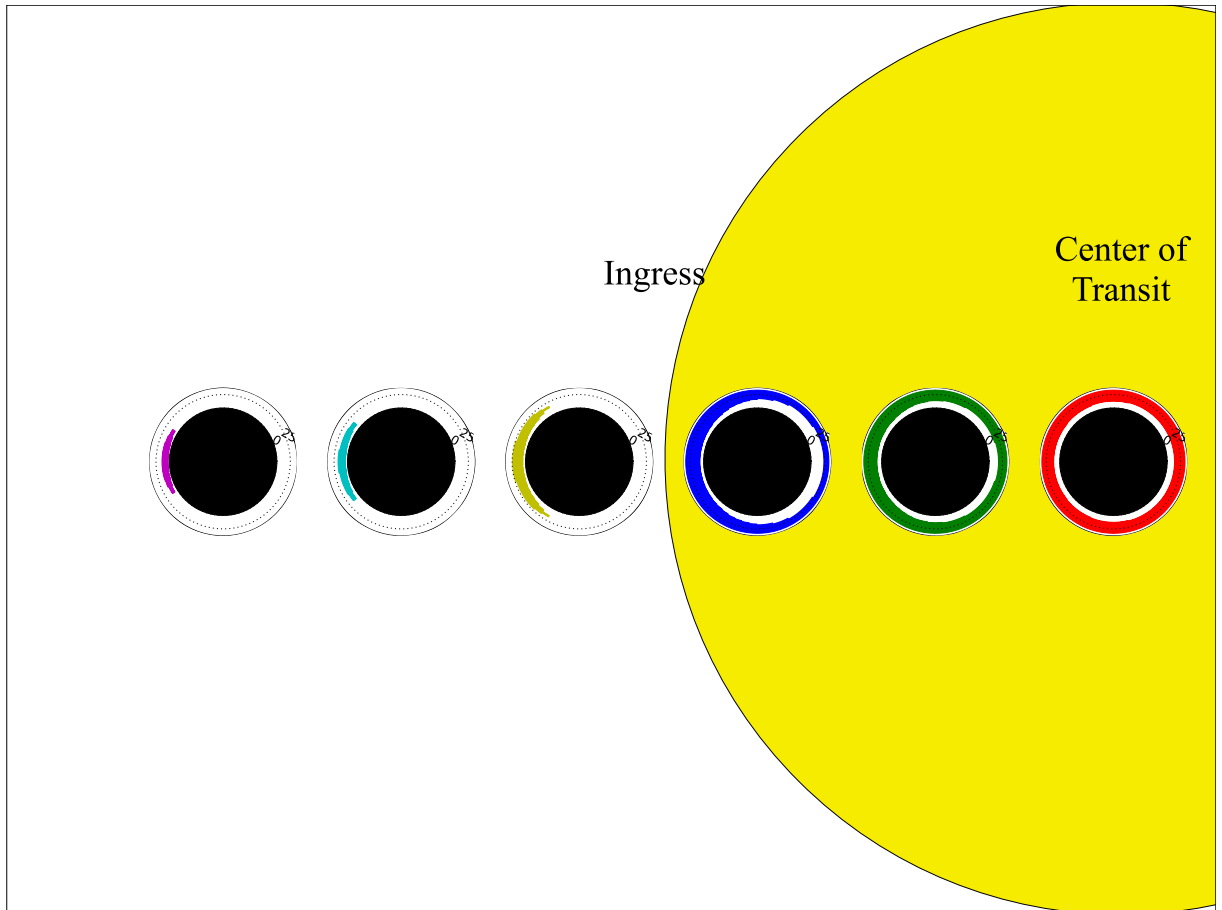


Figure 4.2 Adapted from [Misra et al. \(2014\)](#). This diagram shows where star light for this Earth-Sun analog is transmitted through the planet's atmosphere to the observer. Outside of transit, light is refracted through the atmosphere to the observer through the colored portion. During transit, light is refracted away from the observer, which is shown as the white region, while light passing through the colored region reaches the observer. Thus outside of transit, refraction increases the overall light from the system and probes only the lower layers of the atmosphere, and, during transit, refraction limits how deeply into the atmosphere transmission spectroscopy can probe.

(2012), on the other hand, include a variable opaque layer when modeling the observations of the transit of Venus. Assuming no clouds, their model for Venus predicts an effect of roughly 1.6 ppm at maximum brightness, compared to the Sidis & Sari (2010) prediction of 1.9 ppm. The Tanga et al. (2012) model, however, makes frequent use of the distance between Earth and Venus, which becomes infinity when considered for an exoplanet transit, so it is not entirely applicable to my purpose.

## 4.2 Averaging the Data

The Sidis & Sari (2010) refraction model predicts a brightening of, at most, roughly 100 ppm. The maximum brightness is achieved just before 1st contact and just after last contact, and the maximum lasts for a very short time. The short duration requires that I use short cadence data (58.85 s cycle) from *Kepler*, and the small signal makes it difficult to detect by averaging transits from individual planet candidates. Considering only individual candidates also introduces the possibility of being misled by false positives. Thus I add together transits from multiple planet candidates with similar physical characteristics to improve the signal to noise as well as statistically characterize the group of candidates.

Since I expect the brightest signal to be at shoulder just outside of first and last contact, I want to add together the shoulder for each planet in such a way that the shoulders stack on top of each other. I do this by first changing the time of the observation to orbital phase for the data point for the candidate, and then I transform from phase to the projected distance  $X$  on the sky between the planet

center and the star center, in units of the host star radius. First and last contact occur at  $X = -1 - (R_p/R_*)$  and  $X = 1 + (R_p/R_*)$ . I then pick as a reference the candidate with the largest value of  $R_p/R_*$ , and I linearly transform X for each observation to that reference, stretching the light curve in X so that first and last contact occur at the same value of the transformed X for each candidate. Figure 4.3 shows an example of this process, where the black points are plotted for the original X of the candidate, and the red points are plotted for X transformed to the reference candidate. The solid, vertical lines are the position of  $X = 1 + (R_p/R_*)$  for the original X (black) and the transformed X (red).

To further prepare the transits for stacking, I normalize the individual transits of each candidate in a chosen group first by dividing by the average, out-of-transit flux of the star in each data file, and then I fit a line across a small region around the transit, excluding the transit, and divide by the line. Thus the transits all have a continuum of 1. I eliminate candidates that have  $1 - b - (R_p/R_*) < 0$ , where  $b$  is the impact parameter of the transit, because [Batalha et al. \(2013\)](#) note that such cases are more likely to be false positives. I also automatically eliminate transits which suffer from systematic effects from the *Kepler* instrument, as well as poor linear fits due to short-time-scale variations of the host star. I also check each candidate by eye to ensure there are no anomalies that make it past the automatic screening.

I combine all the individual transits of all the candidates in the group by binning in transformed X with bin sizes of 0.1, weighting the data by their uncertainties. Figure 4.4 shows the result of combining 318 transits from 10 planet candidates with equilibrium temperatures (assuming an albedo of 0.3, as in the *Kepler* candidate ta-

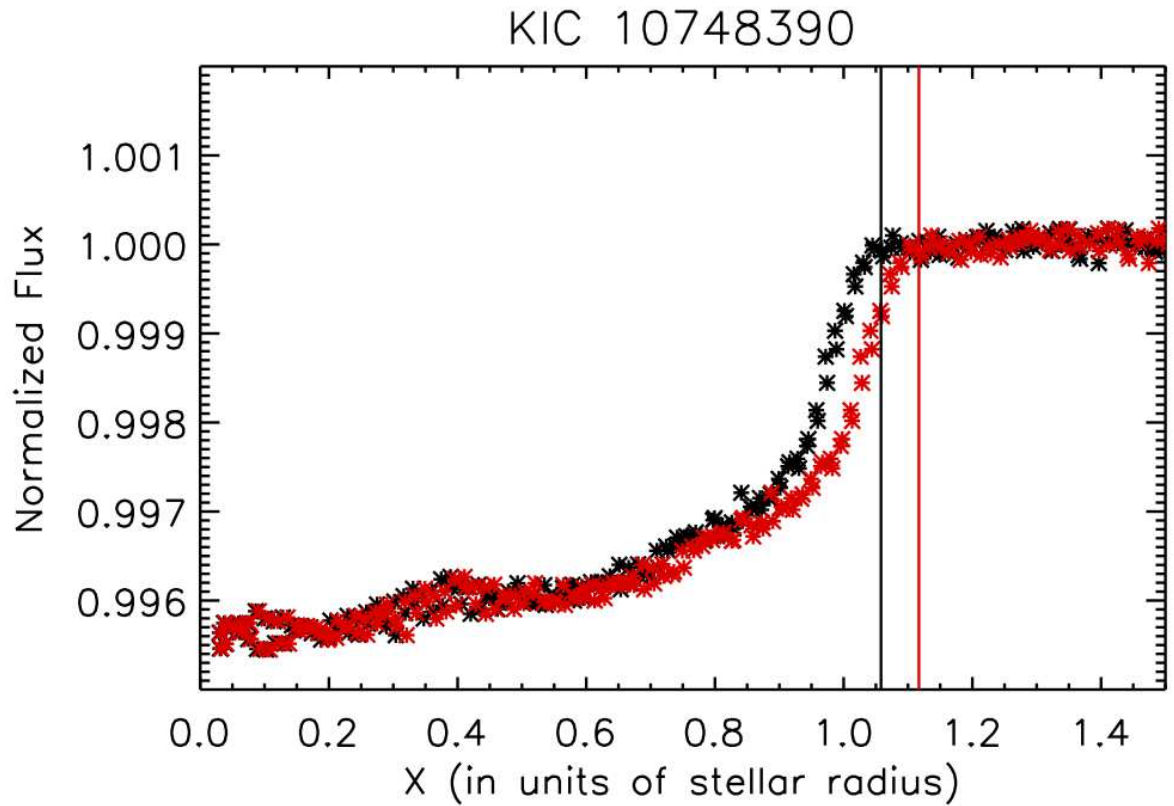


Figure 4.3 This figure shows the transform from  $X$  of an individual candidate (black points) to the reference value of  $1 + (R_p/R_*)$  (red points), so that the shoulders of the transits stack up at the same value of  $X$ . The vertical, solid lines mark the value of  $X = 1 + (R_p/R_*)$  for the actual candidate (black), in this case Jupiter-sized KIC 10748390, and for the reference candidate (red).

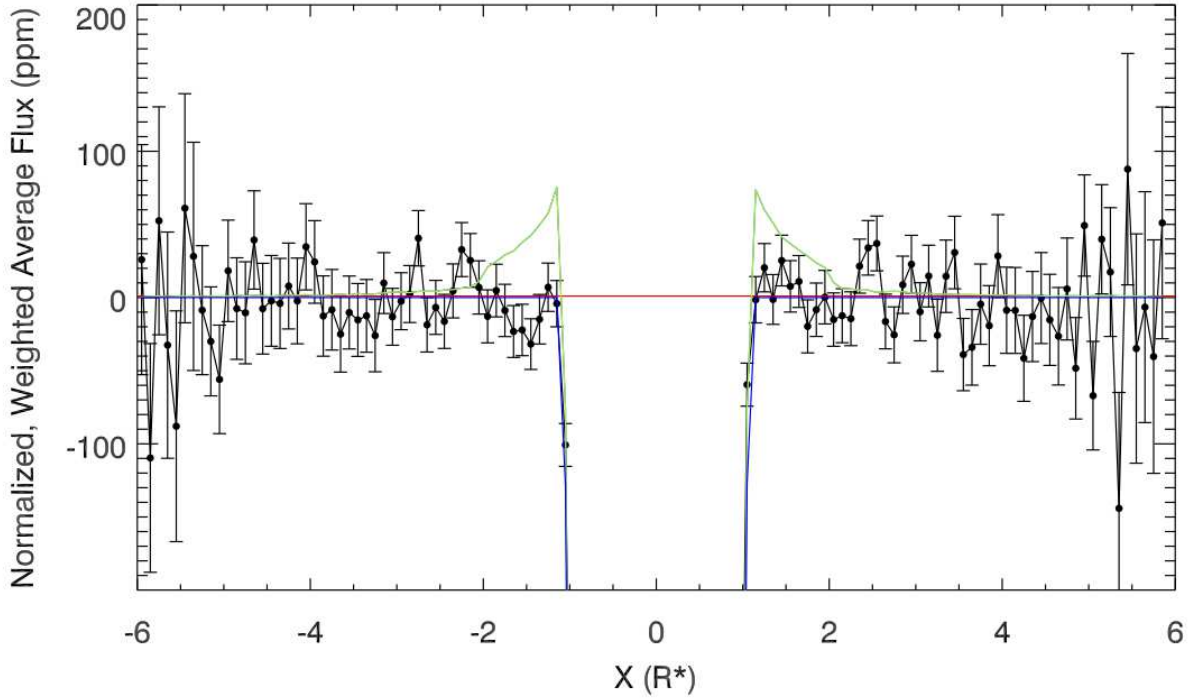


Figure 4.4 This figure shows the weighted average light curve of 318 transits for 10 planet candidates with radii between  $0.8$  and  $3 R_{\oplus}$  and equilibrium temperatures between  $300$  and  $400$  K. The expected refraction signal, in green, has a peak value of  $76$  ppm, while the error bars on the points are  $25$  ppm near the transit. The error bars on the points are the propagated photometric uncertainties. The blue line is the transit model with no refraction (and no stellar limb darkening), while the red line indicates the continuum flux level.

ble) between  $300$  and  $400$  K. These 10 candidates have radii between  $0.8$  and  $3 R_{\oplus}$ . The error bars on the points are the propagated errors from the uncertainties on the photometry. The error bars nearest the transit are  $\pm 12.5$  ppm, while the expected signal, calculated from the [Sidis & Sari \(2010\)](#) model including Rayleigh scattering, shown in green, peaks at  $76$  ppm.

### 4.3 Modeling Refraction

The result thus far suggests that these 10 planets do not have the expected refraction effect from [Sidis & Sari \(2010\)](#), which could be due to clouds or a high mean molecular weight atmosphere. The planets studied at secondary eclipse in Chapter 2 and Chapter 3 were close-in and very hot, with minimum equilibrium temperatures generally above 700K, and likely to be much hotter than the minimum, given the low average albedos. The planets I consider here are cooler, between 300K and 400K (see Figure 4.4). At high temperatures, fewer materials can condense to form clouds. [Wakeford & Sing \(2015\)](#) tabulated the condensation temperatures of expected condensates for hot Jupiters as well as solar system planets and considered the effects of those condensates on transmission spectra. Above 700 K, condensates are typically high molecular weight compounds containing heavy elements like magnesium, silicon, and iron. At lower temperatures, clouds can form from water and other hydrogen compounds like methane ( $\text{CH}_4$ ) and ammonia ( $\text{NH}_3$ ). Given the larger pool of potential cloud particles at cooler temperatures, it is plausible that, while hot sub-Saturns appear on average to be clear, their cooler counterparts may show the opposite behavior and commonly support cloud formation.

The lack of the expected refraction, however, could also mean that the [Sidis & Sari \(2010\)](#) model is just too simplistic. Thus I began developing a light curve model with the aim of accounting for refraction in the case of realistic opacities, for varying atmospheric compositions, and possible opaque cloud layers.

My model thus far starts from the stellar occultation model of [Baum & Code](#)

(1953), shown in Figure 4.5. I assume that the rays detected by the observer are those that emerge from the atmosphere of the planet parallel to the line of sight. I start with a grid of rays, spaced by 0.1 km, and I count how many rays would intercept the star ( $n_N$ ), if there were no refraction through the atmosphere. I then determine the refraction angle of a ray emerging from the atmosphere of the planet at each location of the grid, and the refracted rays are traced back to the plane of the star. The refraction angle is given by Equation 6 of Baum & Code (1953):

$$\theta \simeq (2\pi r_0 a)^{1/2} (n_0 - 1) e^{-a(r_1 - r_0)}, \quad (4.2)$$

where  $a = 1/H$ ,  $n_0$  is the refractive index at radius  $r_0$ , and  $r_1$  is the radius of closest approach to the planet center for the ray. Rays that hit the star are counted ( $n_R$ ), and the brightening due to refraction is then  $n_R/n_N - 1$ . The model currently treats the planet and star as one-dimensional lines, rather than as spheres. Figure 4.6 shows the side view of the planet-star system. The size of the planet has been exaggerated for this plot, in order to better show the planet's position. The purple dashed lines represent the span of rays that pass above the planet and trace back to the surface of the star, after being refracted in the planet's atmosphere. These rays add light to the light curve, because they would not intersect the star in the case of no refraction.

To test this model, I compared the result for Venus's parameters (ignoring the clouds) to the expected values of Sidis & Sari (2010) and Tanga et al. (2012). I have assumed, for the refraction angle of Baum & Code (1953) for the Venus case, that the mean molecular weight is that of CO<sub>2</sub>, 44.01 amu, and an index of refraction

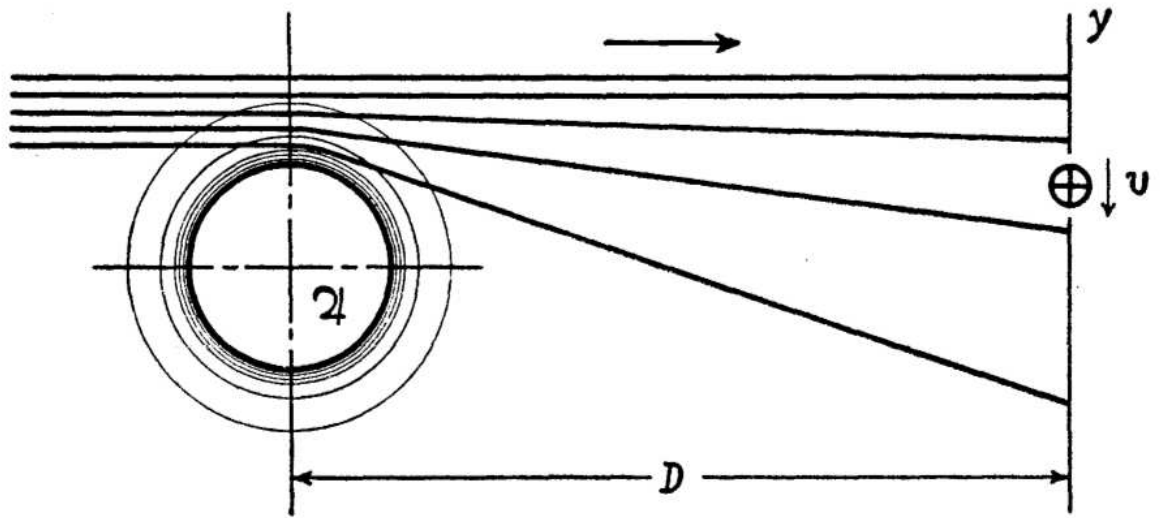


Figure 4.5 Shown is Figure 3 from [Baum & Code \(1953\)](#). For a stellar occultation by Jupiter, the rays from the star come from infinity (left), so they are parallel until being refracted through Jupiter's atmosphere. The rays then diverge before reaching the observer at Earth (right). For the exoplanet case, I assume that the rays leave the star (right), and some rays are refracted through the atmosphere of the planet. The rays detected by the observer (left) are those that leave the planet's atmosphere parallel to the line of sight.

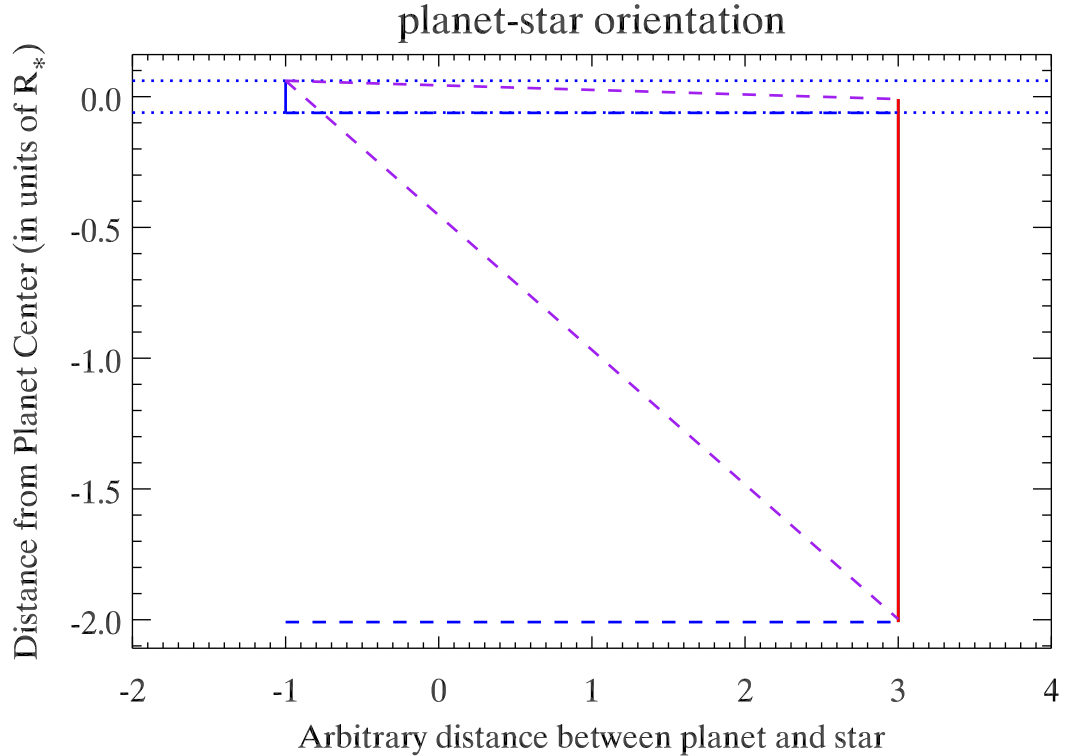


Figure 4.6 Shown is the side-view of the star-planet system in my one-dimensional refraction model. The planet is represented by the blue vertical line, while the star is the red vertical line. The distance between the star and planet in this plot is not to scale. The planet is 7 times the radius of Venus, making the planet easily visible in the plot, and the mass is 16 times that of Venus, giving the planet a bulk density of about  $1 \text{ g cm}^{-3}$ . This radius is much larger than the expected cutoff for rocky planets, and the bulk density too low, but I choose it here for illustration purposes. The center of the planet is at  $y = 0$ , while the center of the star is at  $y = -1.061$ , where the y-axis is in units of the stellar radius. This puts the lower solid limb of the planet at  $y = -0.0609$  and the upper limb of the star at  $y = -0.0610$ , with a ray spacing of less than  $2 \times 10^{-7}$ . The blue dotted lines represent the span of rays that would be blocked by the solid planet. In this particular arrangement, these rays would not intersect the star if the planet were not there, so there is no loss of light due to the solid planet. The blue dashed lines represent the uppermost and lowest, in the y direction, rays that intersect the star. The purple dashed lines represent the span of rays that pass through the planet's atmosphere, above the solid planet, and are refracted downward to intersect the star. These rays add light to the light curve, since they would not otherwise intersect with the star.

of 1.00044, for CO<sub>2</sub> at 0° C and 1 atm (e.g. [Misra & Meadows, 2014](#)). [Sidis & Sari \(2010\)](#) and [Tanga et al. \(2012\)](#) predict a peak effect of approximately 2 ppm, whereas my model predicts 20 ppm. The resulting light curve is shown in [Figure 4.7](#). My model predicts a higher value because of its one-dimensional nature. Since the 20 ppm effect is calculated by dividing the number of rays that intersect the star with refraction ( $n_R$ ) by the number of rays that hit the star without refraction ( $n_N$ ), if one increases  $n_N$  without significantly increasing  $n_R$ , the effect will be diminished. For spherical planets, the refraction effect produces the most light along the equator, where the one-dimensional model is essentially counting rays, and toward the poles the effect is weaker to non-existent. This can be seen in [Figure 4.2](#), where the colored portion of the planet's atmosphere when outside of transit is the region refracting light to the observer. Therefore, if I were including the spherical star and the spherical planet, there would be many more rays counted for  $n_N$ , but a much smaller increase in  $n_R$ .

#### 4.4 Future Work

The next steps in the search for refracted light in exoplanet atmospheres are to continue improving the model and to improve the averaged data by adding candidates and by applying the more sophisticated screening procedures developed in [Chapter 2](#) and [Chapter 3](#) to the sample. I need to define how strong the signal should be for different atmosphere compositions, such as those suggested by [Howe & Burrows \(2012\)](#), as well as how different types of clouds can influence

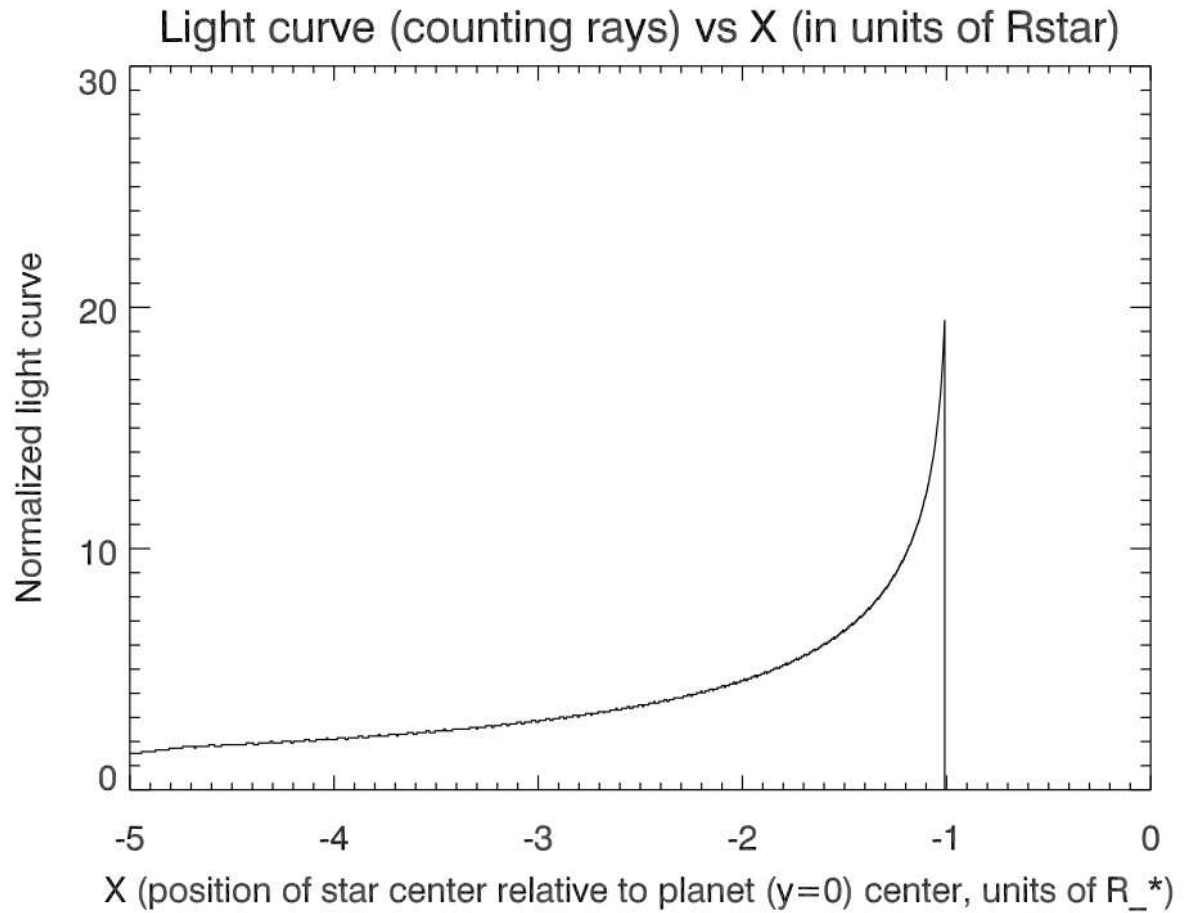


Figure 4.7 Shown is the light curve from my one-dimensional refraction model for a cloud-free Venus. The x-axis is the position of the center of the star relative to the center of the planet, in units of the stellar radius.

the signal. Collaborators Amit Misra and Victoria Meadows have developed a more sophisticated treatment of refraction, detailed in [Misra & Meadows \(2014\)](#) and [Misra et al. \(2014\)](#). Their code not only treats the planet and star as spheres, but also follows the path of a light ray through the atmosphere for a range of tangent altitudes. Rather than the estimated angle of refraction from [Baum & Code \(1953\)](#), the total refraction angle is calculated by integrating a set of differential equations at each point along the ray's path, from entry into the atmosphere to exit. The [Misra & Meadows \(2014\)](#) code allows the setting of an arbitrary cutoff altitude (as a maximum atmospheric pressure that can be probed) to simulate clouds or hazes, with the value of that altitude (i.e. pressure) to be set depending on the type of cloud or haze being simulated. The atmosphere can be modeled layer by layer, instead of the isothermal, constant-scale-height assumption I used in my initial attempts. Furthermore, my collaborators have a line-by-line radiative transfer code which models transmission spectra through atmospheres of various compositions and planet types which has been updated to include refraction ([Misra et al., 2014](#)). I can use this code to create a spectrum with realistic opacities due to spectral features, and integrate over the *Kepler* bandpass to check the [Misra & Meadows \(2014\)](#) models, which do not incorporate spectral line information. I would like to validate the use of refracted light using *Kepler* to show whether, on average, cooler super-Earths and mini-Neptunes are clear-sky, hydrogen-dominated atmospheres amenable to transmission spectroscopy, or are cloudy, hazy, or dominated by high-mean-molecular-weight species.

In addition to improving the model for the predicted refraction signal, I can

also improve our averaged light curves. Since the first attempts, the *Kepler* catalog has not only added more planet candidates, but also improved the parameters for those candidates and their host stars. I can also improve the averaged light curves by incorporating more of the noise tests and normalization techniques developed in Chapters 2 and 3.

With a solid model and a larger, cleaner sample, my postdoctoral research will either detect refracted light in *Kepler* data for the first time, or my work will confirm the preliminary result that cooler planets typically are more cloudy than their hotter counterparts.

## Chapter 5: Summary of the Thesis

In this thesis, I use the wealth of sub-Saturn (less than  $6 R_{\oplus}$ ) planet candidates in the *Kepler* Mission catalog and data archive to determine the average secondary eclipse depth for groups of small, close-in candidates, by averaging many candidates with similar size and orbital characteristics. The average albedo is determined from the average secondary eclipse, giving insight into the atmospheres of the planets. My results are the best constraint to date on the reflectivity of these small, hot planets. My averaging technique provides the necessary signal-to-noise to detect the small signal of the secondary eclipse. The method also prevents biasing of the result by false positives and outliers by not allowing them to dominate the result.

I detected a secondary eclipse depth of  $3.83_{-1.11}^{+1.10}$  ppm for a group of 31 sub-Saturn ( $< 6 R_{\oplus}$ ) planet candidates in short cadence with the greatest potential for a reflected light signature ( $(R_p/a)^2 > 10$  ppm). Including Kepler-10b in this group increased the depth to  $5.08_{-0.72}^{+0.71}$  ppm. Kepler-10b is a special case, due to its host star being several magnitudes brighter than the hosts of the other candidates in the sample. I also find, for a control group with  $(R_p/a)^2 < 1$  ppm, a depth of  $0.36 \pm 0.37$  ppm, consistent with no detection. The control group demonstrates that my method is not introducing spurious eclipse signals. I also analyze the light curve of Kepler-

10b and find an eclipse depth of  $7.08 \pm 1.06$  ppm. If the eclipses are due solely to reflected light, this corresponds to a geometric albedo of  $0.22 \pm 0.06$  for the group of close-in sub-Saturns,  $0.37 \pm 0.05$  if including Kepler-10b in the group, and  $0.60 \pm 0.09$  for Kepler-10b alone. Including a thermal emission model does not change the geometric albedo appreciably, adopting  $A_B = (3/2)*A_g$ . The result for Kepler-10b is consistent with previous works by other authors (e.g. [Batalha et al., 2011](#); [Demory, 2014](#); [Fogtmann-Schulz et al., 2014](#); [Rouan et al., 2011](#)). The result for close-in sub-Saturns shows that Kepler-10b is unusually reflective, but the analysis is consistent with, if a little lower than, the results of [Demory \(2014\)](#) for super-Earths. The results also indicate that hot Neptunes may typically be more reflective than hot Jupiters.

Applying the averaging method to long cadence data, I detect an average secondary eclipse depth of  $2.44 \pm 0.99$  ppm for a group of 55 close-in, 1 to 2  $R_\oplus$  candidates, and a depth of  $2.63^{+1.13}_{-1.14}$  ppm for a subset of 39 of these candidates. These depths both correspond to a geometric albedo  $A_g = 0.11 \pm 0.06$  in the case of complete redistribution of heat. I set an upper,  $3\sigma$  limit of  $A_g < 0.17$  in the case of instantaneous re-radiation, since the measured depths correspond to an unphysical, negative value for albedo. The original group of 55 candidates contains objects that are now known to be, or suspected to be, false positives, while the subset of 39 is the outcome of removing these suspect candidates. I include the results from the original group as well as the “cleaned” subset to demonstrate that the determined albedo is robust to the unintentional inclusion of a few false positives. For a group of 38 close-in, 2 to 4  $R_\oplus$  candidates, I detect an average secondary eclipse depth of

$2.42 \pm 0.76$  ppm, which corresponds to  $A_g = 0.07 \pm 0.03$  for full heat redistribution. Again, only an upper limit can be set for the case of instantaneous re-radiation, but it is much lower than the super-Earths:  $A_g < 0.04$ . A subset of 28 candidates, with suspected false positives removed, gives an average secondary eclipse depth of  $1.69 \pm 0.85$  ppm, which corresponds to  $A_g = 0.05 \pm 0.04$  for full heat redistribution, again demonstrating that the results are robust against inclusion of a few potential false positives. For a group of 16 close-in, 4 to 6  $R_\oplus$  candidates, I find an average secondary eclipse depth of  $2.16_{-1.38}^{+1.37}$  ppm, meaning a geometric albedo  $A_g = 0.12 \pm 0.08$  for full heat redistribution and  $A_g = 0.09 \pm 0.08$  for instantaneous re-radiation. Removing suspected false positives gives a group of 13 candidates with an average secondary eclipse depth of  $1.99_{-1.38}^{+1.37}$  ppm, which corresponds to  $A_g = 0.11 \pm 0.08$  for full redistribution of heat and  $A_g = 0.09 \pm 0.09$  for instantaneous re-radiation. The albedos I find in long cadence are slightly lower but consistent with the albedo I find in the short cadence data. I find an average albedo for super-Earths that are lower than the study of [Demory \(2014\)](#), which may be due to differences in sample selection. There are bright outliers such as Kepler-10b in the super-Earth category, but also for larger, close-in planets in the literature. The low average albedo across the radius bins, which is also consistent with the albedo of the population of dark, hot Jupiters, suggests that on average, hot, close-in planets are cloud-free, and that a common mechanism, such as silicate clouds, is at work to provide the subset of these planets found to have higher albedo. For the smallest planets, less than  $2 R_\oplus$ , the two populations of dark and bright planets could also be indicative of conditions on the surface, possibly a lava ocean with embedded particulates that could boost

the reflectivity of the lava (see references in Sections 2.6 and 3.3.7).

Lastly, I apply the averaging method to the transits of a group of 10 *Kepler* candidates between 0.8 and 3  $R_{\oplus}$ , and equilibrium temperatures between 300 and 400 K, to look for the refraction signal just before and just after transit. The simple model of Sidis & Sari (2010) suggests a refraction signal with peak strength of 76 ppm, which is not seen in the *Kepler* data. I discuss the initial development of a more detailed model for the refraction effect, allowing for different atmosphere compositions and the presence of clouds and hazes. I lay out plans for further developing the model with collaborators (Misra & Meadows, 2014) as part of my postdoctoral research, as well as testing it against the SMART line-by-line radiative transfer code for transmission spectra, including refraction, developed by Misra et al. (2014). I also plan to increase the number of candidates included in the groups in the *Kepler* data analysis, due to improvements in the catalog since the original group average was created. I further plan to improve the average of the data by adapting and applying the refined noise tests from the secondary eclipse studies.

## Bibliography

- Angerhausen, D., DeLarme, E., & Morse, J. A. 2015, *PASP*, 127, 1113
- Batalha, N. M., Borucki, W. J., Bryson, S. T., et al. 2011, *ApJ*, 729, 27
- Batalha, N. M., Rowe, J. F., Bryson, S. T., et al. 2013, *ApJS*, 204, 24
- Baum, W. A., & Code, A. D. 1953, *AJ*, 58, 108
- Bétrémieux, Y., & Kaltenegger, L. 2014, *ApJ*, 791, 7
- Borucki, W., Koch, D., Batalha, N., et al. 2009, *Transiting Planets*, 253, 289
- Borucki, W. J., Koch, D. G., Basri, G., et al. 2011, *ApJ*, 736, 19
- Borucki, W. J., Agol, E., Fressin, F., et al. 2013, *Science*, 340, 587
- Brown, T. M., Charbonneau, D., Gilliland, R. L., Noyes, R. W., & Burrows, A. 2001, *ApJ*, 552, 699
- Brown, T. M., Latham, D. W., Everett, M. E., & Esquerdo, G. A. 2011, *AJ*, 142, 112
- Buchhave, L. A., Latham, D. W., Johansen, A., et al. 2012, *Nature*, 486, 375
- Burke, C. J., Christiansen, J. L., Mullally, F., et al. 2015, *ApJ*, 809, 8
- Castan, T., & Menou, K. 2011, *ApJ*, 743, L36

Catanzarite, J., & Shao, M. 2011, ApJ, 738, 151

Charbonneau, D., Noyes, R. W., Korzennik, S. G., et al. 1999, ApJ, 522, L145

Charbonneau, D., Brown, T. M., Latham, D. W., & Mayor, M. 2000, ApJ, 529, L45

Charbonneau, D., Allen, L. E., Megeath, S. T., et al. 2005, ApJ, 626, 523

Charbonneau, D., Knutson, H. A., Barman, T., et al. 2008, ApJ, 686, 1341-1348

Christiansen, J. L., Ballard, S., Charbonneau, D., et al. 2010, ApJ, 710, 97

Christiansen, J. L., Jenkins, J. M., Caldwell, D. A., et al. 2013, Kepler Data Characteristics Handbook (KSCI-19040-004).

Christiansen, J. L., Clarke, B. D., Burke, C. J., et al. 2015, ApJ, 810, 95

Collier Cameron, A., Horne, K., Penny, A., & James, D. 1999, Nature, 402, 751

Coughlin, J. L., & López-Morales, M. 2012, AJ, 143, 39

Coughlin, J. L., Thompson, S. E., Bryson, S. T., et al. 2014, AJ, 147, 119

Coughlin, J. L., Mullally, F., Thompson, S. E., et al. 2016, ApJS, 224, 12

Deleuil, M., Almenara, J.-M., Santerne, A., et al. 2014, A&A, 564, A56

Deming, D., Seager, S., Richardson, L. J., & Harrington, J. 2005, Nature, 434, 740

Deming, D., Harrington, J., Laughlin, G., et al. 2007, ApJ, 667, L199

Demory, B.-O. 2014, ApJ, 789, L20

Demory, B.-O., Seager, S., Madhusudhan, N., et al. 2011, ApJ, 735, L12

Demory, B.-O., Gillon, M., Seager, S., et al. 2012, ApJ, 751, L28

- Demory, B.-O., Gillon, M., de Wit, J., et al. 2016, *Nature*, 532, 207
- Désert, J.-M., Charbonneau, D., Fortney, J. J., et al. 2011, *ApJS*, 197, 11
- Désert, J.-M., Charbonneau, D., Torres, G., et al. 2015, *ApJ*, 804, 59
- Dressing, C. D., & Charbonneau, D. 2013, *ApJ*, 767, 95
- Dumusque, X., Bonomo, A. S., Haywood, R. D., et al. 2014, *ApJ*, 789, 154
- Elliot, J. L., & Olkin, C. B. 1996, *Annual Review of Earth and Planetary Sciences*, 24, 89
- Esteves, L. J., De Mooij, E. J. W., & Jayawardhana, R. 2013, *ApJ*, 772, 51
- Esteves, L. J., De Mooij, E. J. W., & Jayawardhana, R. 2015, *ApJ*, 804, 150
- Fogtman-Schulz, A., Hinrup, B., Van Eylen, V., et al. 2014, *ApJ*, 781, 67
- Fortney, J. J., Lodders, K., Marley, M. S., & Freedman, R. S. 2008, *ApJ*, 678, 1419
- Fortney, J. J., Demory, B.-O., Désert, J.-M., et al. 2011, *ApJS*, 197, 9
- Fressin, F., Knutson, H. A., Charbonneau, D., et al. 2010, *ApJ*, 711, 374
- Fressin, F., Torres, G., Charbonneau, D., et al. 2013, *ApJ*, 766, 81
- Gandolfi, D., Parviainen, H., Deeg, H. J., et al. 2015, *A&A*, 576, A11
- García Muñoz, A., & Mills, F. P. 2012, *A&A*, 547, A22
- García Muñoz, A., Zapatero Osorio, M. R., Barrena, R., et al. 2012, *ApJ*, 755, 103
- Grillmair, C. J., Charbonneau, D., Burrows, A., et al. 2007, *ApJ*, 658, L115
- Hadden, S., & Lithwick, Y. 2014, *ApJ*, 787, 80

Hansen, B. M. S. 2008, *ApJS*, 179, 484-508

Helling, C., Lee, G., Dobbs-Dixon, I., et al. 2016, *MNRAS*, 460, 855

Heng, K., & Kopparla, P. 2012, *ApJ*, 754, 60

Heng, K., & Demory, B.-O. 2013, *ApJ*, 777, 100

Howe, A. R., & Burrows, A. S. 2012, *ApJ*, 756, 176

Hu, R., Demory, B.-O., Seager, S., Lewis, N., & Showman, A. P. 2015, *ApJ*, 802, 51

Hui, L., & Seager, S. 2002, *ApJ*, 572, 540

Jenkins, J. M., Twicken, J. D., Batalha, N. M., et al. 2015, *AJ*, 150, 56

Ioannidis, P., Schmitt, J. H. M. M., Avdellidou, C., von Essen, C., & Agol, E. 2014, *A&A*, 564, A33

Ito, Y., Ikoma, M., Kawahara, H., et al. 2015, *ApJ*, 801, 144

Kane, S. R., Ciardi, D. R., Gelino, D. M., & von Braun, K. 2012, *MNRAS*, 425, 757

Kipping, D. M., & Spiegel, D. S. 2011, *MNRAS*, 417, L88

Kite, E. S., Fegley, B., Jr., Schaefer, L., & Gaidos, E. 2016, arXiv:1606.06740

Koch, D. G., Borucki, W. J., Basri, G., et al. 2010, *ApJ*, 713, L79-L86

Knutson, H. A., Charbonneau, D., Allen, L. E., et al. 2007, *Nature*, 447, 183

Kreidberg, L., Bean, J. L., Désert, J.-M., et al. 2014, *Nature*, 505, 69

Kurucz, R. L. 1979, *ApJS*, 40, 1

Léger, A., Grasset, O., Fegley, B., et al. 2011, *Icarus*, 213, 1

Liddle, A. R. 2007, MNRAS, 377, L74

Lopez, E. D., & Fortney, J. J. 2014, ApJ, 792, 1

López-Morales, M., & Seager, S. 2007, ApJ, 667, L191

Lovis, C., & Fischer, D. 2010, Exoplanets, 27

Machalek, P., McCullough, P. R., Burke, C. J., et al. 2008, ApJ, 684, 1427-1432

Mandel, K., & Agol, E. 2002, ApJ, 580, L171

Marcus, R. A., Sasselov, D., Hernquist, L., & Stewart, S. T. 2010, ApJ, 712, L73

Marley, M. S., Gelino, C., Stephens, D., Lunine, J. I., & Freedman, R. 1999, ApJ, 513, 879

Marcy, G. W., Isaacson, H., Howard, A. W., et al. 2014, ApJS, 210, 20

Mayor, M., & Queloz, D. 1995, Nature, 378, 355

Miguel, Y., Kaltenegger, L., Fegley, B., & Schaefer, L. 2011, ApJ, 742, L19

Misra, A. K., & Meadows, V. S. 2014, ApJ, 795, L14

Misra, A., Meadows, V., & Crisp, D. 2014, ApJ, 792, 61

Morley, C. V., Marley, M. S., Fortney, J. J., et al. 2014, ApJ, 787, 78

Morris, B. M., Mandell, A. M., & Deming, D. 2013, ApJ, 764, L22

Morton, T. D., Bryson, S. T., Coughlin, J. L., et al. 2016, ApJ, 822, 86

Mullally, F., Coughlin, J. L., Thompson, S. E., et al. 2015, ApJS, 217, 31

Pasachoff, J. M., Schneider, G., & Widemann, T. 2011, AJ, 141, 112

- Petigura, E. A., Howard, A. W., & Marcy, G. W. 2013, Proceedings of the National Academy of Science, 110, 19273
- Pinsonneault, M. H., An, D., Molenda-Żakowicz, J., et al. 2012, ApJS, 199, 30
- Rauer, H., Catala, C., Aerts, C., et al. 2014, Experimental Astronomy, 38, 249
- Ricker, G. R., Winn, J. N., Vanderspek, R., et al. 2015, Journal of Astronomical Telescopes, Instruments, and Systems, 1, 014003
- Rogers, L. A. 2015, ApJ, 801, 41
- Rouan, D., Deeg, H. J., Demangeon, O., et al. 2011, ApJ, 741, L30
- Rowe, J. F., Matthews, J. M., Seager, S., et al. 2006, ApJ, 646, 1241
- Rowe, J. F., Matthews, J. M., Seager, S., et al. 2008, ApJ, 689, 1345
- Sanchis-Ojeda, R., Rappaport, S., Winn, J. N., et al. 2013, ApJ, 774, 54
- Sanchis-Ojeda, R., Rappaport, S., Winn, J. N., et al. 2014, ApJ, 787, 47
- Santerne, A., Bonomo, A. S., Hébrard, G., et al. 2011, A&A, 536, A70
- Santerne, A., Fressin, F., Díaz, R. F., et al. 2013, A&A, 557, A139
- Schaefer, L., & Fegley, B. 2009, ApJ, 703, L113
- Sheets, H. A., & Deming, D. 2014, ApJ, 794, 133
- Shporer, A., O'Rourke, J. G., Knutson, H. A., et al. 2014, ApJ, 788, 92
- Sidis, O., & Sari, R. 2010, ApJ, 720, 904
- Sing, D. K., Fortney, J. J., Nikolov, N., et al. 2016, Nature, 529, 59
- Smith, J. C., Stumpe, M. C., Van Cleve, J. E., et al. 2012, PASP, 124, 1000

- Spiegel, D. S., Burrows, A., Ibgui, L., Hubeny, I., & Milsom, J. A. 2010, *ApJ*, 709, 149
- Stumpe, M. C., Smith, J. C., Van Cleve, J. E., et al. 2012, *PASP*, 124, 985
- Sudarsky, D., Burrows, A., & Pinto, P. 2000, *ApJ*, 538, 885
- Tanga, P., Widemann, T., Sicardy, B., et al. 2012, *Icarus*, 218, 207
- Thompson, S. E., Christiansen, J. L., Jenkins, J. M., et al. 2013, Kepler Data Release 21 Notes (KSCI-19061-001)
- Todorov, K., Deming, D., Harrington, J., et al. 2010, *ApJ*, 708, 498
- Torres, G., Kipping, D. M., Fressin, F., et al. 2015, *ApJ*, 800, 99
- Traub, W. A., & Oppenheimer, B. R. 2010, *Exoplanets*, 111
- Valenti, J. A., & Piskunov, N. 1996, *A&AS*, 118, 595
- Verbiscer, A., French, R., Showalter, M., & Helfenstein, P. 2007, *Science*, 315, 815
- Wakeford, H. R., & Sing, D. K. 2015, *A&A*, 573, A122
- Winn, J. N. 2010, *Exoplanets*, 55
- Wolszczan, A., & Frail, D. A. 1992, *Nature*, 355, 145
- Wolszczan, A. 1994, *Science*, 264, 538
- Zahnle, K., Marley, M. S., Freedman, R. S., Lodders, K., & Fortney, J. J. 2009, *ApJ*, 701, L20
- Zellem, R. T., Lewis, N. K., Knutson, H. A., et al. 2014, *ApJ*, 790, 53